# Numerical Modeling of the Runway Deicing Products Performance on Aircraft Runways

by

Aida MAROUFKHANI

THESIS PRESENTED TO ÉCOLE DE TECHNOLOGIE SUPÉRIEURE
IN PARTIAL FULFILLEMENT FOR THE DEGREE OF
DOCTOR OF PHILOSOPHY
Ph.D.

MONTREAL, JANUARY 16, 2025

ÉCOLE DE TECHNOLOGIE SUPÉRIEURE
UNIVERSITÉ DU QUÉBEC

**BOARD OF EXAMINERS**

**THIS THESIS HAS BEEN EVALUATED**

**BY THE FOLLOWING BOARD OF EXAMINERS**

Mr. François Morency, Thesis Supervisor
Mechanical Engineering Department at École de technologie supérieure

Mrs. Gelareh Momen Thesis Co-supervisor
Applied Sciences Department at Université du Québec à Chicoutimi

Mr. Michel Baraër, Member of the Jury
Construction Engineering Department at École de technologie supérieure

Mr. François Garnier, Member of the Jury
Mechanical Engineering Department at École de technologie supérieure

Ms. Leyla Amiri, External Evaluator
Mechanical Engineering Department at Université du Sherbrooke

THIS THESIS WAS PRENSENTED AND DEFENDED

IN THE PRESENCE OF A BOARD OF EXAMINERS AND PUBLIC

JANUARY 9, 2025

AT ECOLE DE TECHNOLOGIE SUPERIEUR

## ACKNOWLEDGMENT

I would like to express my deepest gratitude to Prof. François Morency for being my research director. Over the past four years, your professionalism, punctuality, and insightful guidance have been a constant source of inspiration. It has been a privilege to work under your supervision, and I am truly grateful for all the knowledge and support you have shared.

A special thank you to my co-supervisor, Prof. Gelareh Momen, for her kindness, encouragement, and valuable support throughout this journey. I wish you the very best in your future endeavors.

To my loving husband, Amin, the most amazing and supportive partner—your love, encouragement, and belief in me have been the driving force behind my success. Thank you for always standing by my side and inspiring me to achieve my dreams. I couldn't have done this without you.

To my incredible sister, Azadeh, the kindest person I know—thank you for always being there for me, listening with patience, and offering your unwavering support. Your encouragement and understanding have meant the world to me.

To my wonderful parents, the greatest role models and sources of unconditional love—thank you for your sacrifices, your belief in me, and your endless encouragement. Your support has been the foundation of everything I have accomplished.

Finally, I am deeply grateful to my brother, my aunt, and my friends for believing in me and for your encouragement and companionship. Your presence and support have made this journey truly memorable.

# NUMERICAL MODELING OF THE RUNWAY DEICING PRODUCTS PERFORMANCE ON AIRCRAFT RUNWAYS

Aida MAROUFKHANI

## RÉSUMÉ

Les pistes couvertes de glace augmentent le risque d'accidents en rendant les surfaces glissantes. Dans l'aviation, le dégivrage des pistes est essentiel pour garantir des décollages et des atterrissages en toute sécurité. Cependant, l'utilisation excessive de produits de dégivrage soulève des préoccupations environnementales. Développer un modèle mathématique peut aider à réduire l'utilisation de ces produits. Les modèles 0D actuels s'appuient principalement sur des taux de fonte empiriques constant pour les chaussées, manquant de précision pour prédire les conditions des pistes. Cette recherche présente un modèle unidimensionnel pour estimer les taux de fonte de la glace sur les pistes ainsi que les températures de surface, en fonction de la quantité de dégivrant et des conditions environnementales. Le modèle de dégivrage de piste se base sur le problème de Stefan à deux phases, modifié pour tenir compte de la concentration non uniforme de dégivrant, régie par la loi de Fick pour la diffusion de masse. La méthode de l'enthalpie a été adoptée pour le changement de phase avec des températures de fusion variables, en utilisant une approche par volumes finis pour résoudre le modèle de manière explicite. La vérification a été effectuée en comparant avec la solution de similarité de Neumann, confirmant les capacités du modèle de dégivrage de piste à prédire la température et la position du front de fusion. Avec les dégivrants, le modèle a prédit des paramètres clés comme la température de surface, le front de fusion et les gradients de concentration, vérifiant ainsi sa capacité à simuler des comportements attendus tels que la relation température-concentration selon la courbe du liquidus. La validation du modèle est basée sur des expériences de fonte de glace contrôlées suivant les normes AS6170, où des solutions de dégivrage à -2 °C et -10 °C ont été appliquées à des échantillons de glace. À -2 °C, l'erreur de prévision de la température du modèle était de 0,9 % pour le KFO (formate de potassium) et de 0,88 % pour le KAC (acétate de potassium), avec des écarts de prévision de masse fondue de 15 % pour le KFO et de 11 % pour le KAC après 5 minutes, se stabilisant au

fil du temps. À -10 °C, l'erreur de température était de 1,2 % pour les deux dégivrants, avec des erreurs de masse fondue de 11,8 % pour le KFO et de 16 % pour le KAC. L'étude paramétrique a examiné les effets de variables telles que le coefficient de convection thermique, l'épaisseur initiale du dégivrant et la température de fusion. Dans des conditions spécifiques aux pistes, le KAC a obtenu un taux de fonte plus élevé que le KFO dans divers scénarios de température. De plus, la fréquence de réapplication a été testée est les résultats ont montré que des applications plus importantes mais moins fréquentes faisaient fondre légèrement plus de glace, améliorant l'efficacité du dégivrage sur les pistes.

**Mots-clés :** Modèle de Dégivrage de Piste ; Problème de Stefan à Deux Phases ; Loi de Fick ; Méthode de l’Enthalpie ; Taux de Fonte de la Glace ; Modélisation Numérique ; Réapplication de Dégivrant

# NUMERICAL MODELING OF THE RUNWAY DEICING PRODUCTS PERFORMANCE ON AIRCRAFT RUNWAYS

Aida MAROUFKHANI

## ABSTRACT

Ice-covered runways increase accident risk by making surfaces slippery. In aviation, deicing runways is essential to ensure safe takeoffs and landings. However, excessive deicing chemical use raises environmental concerns. Developing a mathematical model can help to reduce chemical usage. Current 0D models primarily rely on constant empirical melting rates for road pavements, lacking the precision needed for runway conditions. This research presents a one-dimensional model to estimate runway ice melting rates and surface temperatures based on deicer quantity and environmental conditions. The Runway Deicing model employs the two-phase Stefan problem, modified to account for non-uniform deicer concentration, governed by Fick's law for mass diffusion. The enthalpy method was adopted for phase change with variable melting temperatures, using a finite volume approach to solve the model explicitly. Verification was performed through comparison with the Neumann similarity solution, confirming the Runway Deicing Model's accuracy in predicting temperature and melting front location. With deicers, the model predicted key parameters like surface temperature, melting front, and concentration gradients, verifying its performance by capturing expected behaviors like the temperature-concentration relationship according to the liquidus curve. Model validation was based on controlled ice melting experiments following AS6170 standards. Deicing solutions at -2°C and -10°C were applied to ice samples. At -2°C, the model's temperature prediction error was 0.9% for KFO (Potassium formate) and 0.88% for KAC (Potassium acetate), with the mass prediction discrepancies of 15% for KFO and 11% for KAC at 5 minutes, stabilizing over time. At -10°C, temperature error was 1.2% for both deicers, with the mass errors of 11.8% for KFO and 16% for KAC. The parametric study examined the effects of variables such as the heat convection coefficient, initial deicer thickness, and melting temperature. Under runway-specific conditions, KAC achieved a higher melting rate than KFO across temperature scenarios. Additionally, reapplication frequency was tested and the results

showed that larger, less frequent applications melted slightly more ice, enhancing deicing efficiency on runways.

**Keywords:** Runway Deicing Model; Two-Phase Stefan Problem; Fick's Law; Enthalpy Method; Ice Melting Rates; Numerical Modeling; Deicer Reapplication

## TABLE OF CONTENTS

Page

## LIST OF TABLES

Page

## LIST OF FIGURES

Page

## LIST OF ABREVIATIONS

| | |
|---|---|
| RDP | Runway Deicing Product |
| RDM | Runway Deicing Model |
| 0D | Zero dimensional |
| 1D | One dimensional |
| 2D | Two dimensional |
| 3D | Three dimensional |
| KFO | Potassium Formate |
| KAC | Potassium Acetate |
| UCAR | Ethylene Glycol-based fluid containing Ethylene Glycol, Urea, and water |
| CMA | Calcium Magnesium Acetate |
| NaAc | Sodium Acetate |
| NaF | Sodium Formate |
| NaCl | Sodium Chloride |
| $MgCl_2$ | Magnesium Chloride |
| $CaCl_2$ | Calcium Chloride |
| RMSE | Root Mean Square Error |
| DSC | Differential Scanning Calorimetry |
| AMS | Aerospace Material Specifications |
| BC | Boundary Condition |
| AS6170 | Aerospace Standard |
| AMIL | Anti-Icing Materials Laboratory |
| NRC | National Research Council of Canada |
| ADM | Aéroports de Montréal |
| CRIAQ | Consortium for Research and Innovation in Aerospace of Québec |

## LIST OF SYMBOLS & UNITS OF MEASURMENTS

*Symbols*

| | |
|---|---|
| $A$ | Area ($m^2$) |
| $C$ | Mass concentration (%) |
| $C_{volume}$ | Volume concentration (%) |
| $C_e$ | Eutectic concentration of deicing solution (%) |
| $C_l$ | Concentration of solute in the liquid (deicing solution) (%) |
| $C_s$ | Concentration of solute in the solid region (ice) (%) |
| $c_{p-s}$ | Specific heat of solid (ice) ($J\ kg^{-1}$°C) |
| $c_{p-l}$ | Specific heat of liquid (deicing solution) ($J\ kg^{-1}$°C) |
| $D_l$ | Diffusion coefficient of liquid (deicing solution) ($m^2 s^{-1}$) |
| $D_s$ | Diffusion coefficient of solid (ice) ($m^2 s^{-1}$) |
| $E$ | Energy ($J\ m^{-2}$) |
| $E_{liquid}$ | Local enthalpy in the liquid phase ($J\ m^{-3}$) |
| $E_{solid}$ | Local enthalpy in the solid phase ($J\ m^{-3}$) |
| $F_0$ | Dimensionless time variable |
| $h$ | Heat transfer coefficient for combination of convection-radiation ($W\ m^{-2}K^{-1}$) |
| $h_c$ | Heat convection coefficient ($W\ m^{-2}K^{-1}$) |
| $H_{initial}$ | Initial deicing solution thickness ($m$) |
| $j$ | Node |
| $J$ | Diffusion flux ($m\ s^{-1}$) |

| | |
|---|---|
| $k_l$ | Thermal conductivity of liquid (deicing solution) ($W\ m^{-1}\ K^{-1}$) |
| $k_s$ | Thermal conductivity of solid (ice) ($W\ m^{-1}\ K^{-1}$) |
| $L$ | Length ($m$) |
| $L_f$ | Latent heat ($J\ kg^{-1}$) |
| $M$ | Number of nodes |
| $M_w$ | Molar mass ($kg\ mol^{-1}$) |
| $m$ | Total mass of the deicing solution ($kg$) |
| $m_1$ | Mass of the solute ($kg$) |
| $m_2$ | Mass of the solvent ($kg$) |
| $m_e$ | Final masses of the petri dish and remaining ice ($g$) |
| $m_{im}$ | Mass of ice melted in experimental test ($g$) |
| $m_s$ | Initial masses of the Petri dish and ice sheet ($g$) |
| $m_{Deicing\ solution-experimental}$ | Mass of deicing solution in experimental test ($kg$) |
| $m_{Deicing\ solution-runway\ model}$ | Mass of deicing solution in runway deicing model ($kg$) |
| $m_{solution-initial}$ | Initial mass of deicing solution in experimental test ($g$) |
| $n$ | Time number |
| $q$ | Heat flux ($W\ m^{-2}$) |
| $q_{convection-radiation}$ | Convection-radiation heat flux ($W\ m^{-2}$) |
| $R$ | Resistance ($W\ m^{-1}K^{-1}$) |
| $T_e$ | Eutectic temperature of deicing solution (℃) |
| $T_{experimental}$ | Experimental temperature (K) |

| | |
|---|---|
| $T_l$ | Deicing solution temperature (℃) |
| $T_m$ | Melting temperature (℃) |
| $T_{mpure}$ | Melting temperature of pure ice (℃) |
| $T_\infty$ | Air temperature (℃) |
| $T_p$ | Pavement temperature (℃) |
| $T_s$ | Ice temperature (℃) |
| $T_{runway\ model}$ | Runway deicing model surface temperature ($K$) |
| $t$ | Time ($min$) |
| $u$ | Dimensionless temperature |
| $V$ | Total volume of the deicing solution ($m^3$) |
| $V_1$ | Volume of solute ($m^3$) |
| $V_2$ | Volume of solvent ($m^3$) |
| $V_C$ | Molar volume of the solute in the solvent at its normal boiling point ($m^3$) |
| $v$ | Wind velocity ($m\ s^{-1}$) |
| $x$ | Spatial coordinate along the normal direction ($m$) |
| $\hat{x}$ | Convenient length scale ($m$) |
| $X$ | Melting front location ($m$) |
| $X_{initial}$ | Initial melting front location ($m$) |
| $\dot{X}$ | Velocity of the melting front ($m\ s^{-1}$) |

*Greek letters*

| | |
|---|---|
| $\alpha_l$ | Thermal diffusivity in liquid ($m\ s^{-1}$) |
| $\alpha_s$ | Thermal diffusivity in solid ($m\ s^{-1}$) |
| $\beta$ | Dimensionless number in root equation |
| $\Delta t$ | Time step ($min$) |
| $\Delta$x | Spatial step ($m$) |
| $\Delta t_T$ | Thermal stability condition ($min$) |
| $\Delta t_c$ | Concentration stability condition ($min$) |
| $\Delta t_{exp}$ | Explicit time step ($min$) |
| $\varepsilon_s$ | Surface emissivity |
| $\lambda$ | Liquid fraction |
| $\lambda_{Neumann}$ | Transcendental root |
| $\xi$ | Dimensionless length |
| $\sigma$ | Stephan–Boltzmann constant ($W\ m^{-2}K^{-4}$) |
| $\Sigma(F_0)$ | Dimensionless melting front |
| $\rho$ | Density of the deicing solution ($kg\ m^{-2}$) |
| $\rho_1$ | Density of the solute ($kg\ m^{-2}$) |
| $\rho_2$ | Density of the solvent ($kg\ m^{-2}$) |
| $St_L$ | Stefan condition in liquid phase |
| $St_s$ | Stefan condition in solid phase |
| $\Psi_w$ | Solvent-specific empirical parameter |
| $\eta^{sol}$ | Viscosity of the solution ($Pa\ s^{-1}$) |

# INTRODUCTION

## Runway Deicing

In the realm of aviation, where safety is paramount, meticulous considerations must be made to ensure the well-being of passengers and the seamless operation of flights. Particularly during winter, the aviation industry faces unique challenges that demand comprehensive strategies for airport safety. Addressing the potential hazards of slippery runways becomes a critical focus, given the adverse weather conditions characterized by precipitation such as rainfall, snowfall, and freezing rain (Klein-Paste, 2007, 2018).

The necessity for proactive measures is underscored by the fact that winter temperatures often plummet below 0°C, leading to the accumulation of snow on airport pavements. This accumulation, when left unattended, forms a perilous bond with runways, posing a significant threat to the safe take-off and landing of aircraft. Between 1958 and 1993, over 100 aircraft incidents occurred due to the presence of water, ice, or snow on runways. The majority of these incidents resulted in fatalities (Comfort, 2001). A poignant example highlighting the repercussions of inadequate winter maintenance is the Delta Air Lines MD-88 incident in 2015, where a flight from Atlanta to New York-LaGuardia skidded off Runway 13 during landing (National-Transportation-Safety-Board, 2016). Three additional instances of airplanes sliding off runways include two occurrences at Chicago O'Hare Airport, involving United Airlines Flight 1977 (Associated-Press, 2015) and United Airlines Flight 734 (CBS-news, 2016). Another recent incident took place on February 8, 2019, at Bagotville Airport (YBG) when an aircraft skidded off the runway after landing (Radio-Canada, 2019). In each of these cases, the incidents were attributed to slippery runway conditions caused by snow and ice.

These events serve as the stark reminder of the potential dangers associated with runway slipperiness during winter conditions. It is incidents like these that underscore the urgency of implementing robust winter maintenance activities at airports, particularly in countries like Canada with severe winter climates (Hassan et al., 2002).

In addressing the imperative of maintaining runway safety during winter, the aviation industry employs various strategies, with a significant focus on the removal of ice to mitigate hazards. Deicing approach plays a pivotal role in controlling snow and ice accumulation on runways. In this thesis, deicing is the process of removing existing ice or snow from the runway. This multifaceted strategy incorporates both chemical and mechanical methods to ensure thorough ice removal. Initially, chemical agents are applied to the runways to break the bond between the ice and the pavement. Once this bond is weakened, mechanical tools such as plows, brushes, blowers, and shovels are employed to physically remove the dislodged ice. This two-step process addresses both the chemical and physical aspects of deicing, aiming to thoroughly clear the runway surface and reduce slipperiness (Barash et al., 2000).

**Deicing Chemicals**

In the realm of chemical deicing products, several agents are employed to achieve the desired effect. These substances operate by depressing the freezing point, melting ice on the runway (US-Environmental-Protection-Agency, 2012). Commonly used deicing and anti-icing agents for pavements include ethylene glycol, propylene glycol, urea, UCAR (an ethylene glycol-based fluid containing approximately 50% ethylene glycol, 25% urea, and 25% water by weight), potassium acetate, sodium acetate, sodium formate, and calcium magnesium acetate (CMA). The application of sand, although enhancing the friction on icy surfaces, may adversely affect the mechanical components of aircraft. Salt, such as sodium chloride or potassium chloride, is utilized for deicing/anti-icing in areas not frequented by aircraft, like roadways and parking lots (Barash et al., 2000).

In North America, extensive quantities of de-icing products are applied on airport runways to ensure secure take-off and landing amidst challenging weather conditions. Following their application, a portion of these chemicals has the potential for recovery, while, in certain instances, they disperse into the surrounding environment (Shi et al., 2017). Despite the critical implications of environmental contamination, there has been limited attention directed towards assessing and reducing the quantities of deicing products for runway application. The

environmental ramifications of deicer chemicals have been elucidated in an article by Widyatmoko and Dehdezi (2015), emphasizing their adverse effects on soils, flora, fauna, and airfield pavements.

The selection of chemical agents is bound by two considerations. Firstly, it involves choosing the most effective deicing and anti-icing products that exert minimal negative impact on the environment. A product is considered more effective if it can melt a larger volume of ice and has strong ice penetration capabilities (Charpentier et al., 2023). Traditional airfield runway deicing products (RDPs) containing urea or glycols, for instance, have diminished in popularity due to their negative environmental impacts. Newer RDPs have emerged as substitutes, often incorporating sodium acetate (NaAc), potassium acetate (KAc), potassium formate (KF), or sodium formate (NaF) as freezing point depressants. While these chemicals are pricier, they are also more effective than urea at lower temperatures (Shi, 2008). In Canada, the prevailing consensus is that the heightened effectiveness and simultaneous reduction in environmental concerns justify the increased cost associated with the use of these newer RDPs (Shi, 2008). Secondly, compatibility with various materials is crucial, encompassing the pavement, aircraft, and runway infrastructure. It is noteworthy that certain modern chemical agents, such as Alkali-metal-salt, may contribute to a reduced lifespan for aircraft brakes and corrosion of aircraft alloys (Shi, 2008).

To mitigate these impacts, the aviation industry is steadfast in its objective to minimize the use of chemical components during deicing operations. This reduction aims to curtail the negative influence on the environment, thereby reducing the risk of contamination in areas proximate to transportation infrastructure. In pursuit of this ecological goal, a model aimed at reducing deicer usage needs to be developed. Such a model would help estimate the amount of deicer required to melt a specific amount of ice, thereby reducing environmental pollution associated with excess deicer application, while still maintaining necessary safety measures for aviation operations.

The utilization of a mathematical model has the potential to enhance the efficiency of deicer chemical applications by estimating the needed amount of deicer chemical. While certain road deicing models can predict pavement temperature during deicing operations under snow or ice cover, there is still a need for a more complete model to predict heat transfer, water, and deicer mass transfer in at least one dimension. Additionally, the characteristics of airport, such as environmental conditions and the size of the runway, call for a specialized model tailored to runway deicing. Ultimately, the model should forecast the quantity of RDP required for complete snow and ice melting on the runway. To our knowledge, there is currently no existing model of this nature, and no attempts have been made to develop one in the open literature in the past.

In the context of runway deicing, the scenario involves the application of a liquid deicing solution onto pure ice surfaces. Importantly, the melting point of the deicing solution varies according to its concentration. Initially, the concentration of deicer is higher in the deicing solution compared to the ice, but as the ice melts, the concentration decreases. Moreover, the melting point itself varies spatially and temporally, resulting in a dynamic melting temperature throughout the deicing process.

The existing models that incorporate variable melting points using enthalpy method, particularly focus on the solidification of chemical solutions or the melting of frozen solutions. For example, Voller (2008) introduced a fixed-grid enthalpy model designed to simulate dendritic growth in under-cooled binary alloys. Similarly, Jamil et al. (2006) developed an enthalpy-based model to analyze heat transfer during the melting of saline binary solutions, applying it to calorimetry to determine eutectic melting kinetics, with validation via differential scanning calorimetry (DSC) for accurate temperature measurements.

This thesis aligns with the objectives outlined in goal #4 of the project O2HPA. Entitled “Optimization of Winter Operations of Airport Runways”, this collaborative project is supported by National Research Council of Canada (NRC) and Consortium for Research and Innovation in Aerospace of Québec (CRIAQ). The project involves a partnership with three

Canadian industries—Aéroports de Montréal (ADM), Nachurs Alpine Solutions, and Wpred—alongside collaboration with two universities and a government laboratory: the Université du Québec à Chicoutimi (UQAC) with its Anti-Icing Materials Laboratory (AMIL), and the École de Technologie Supérieure (ÉTS) of Montréal.

**Objectives**

The process of chemical deicing on runways necessitates a comprehensive model that considers both spatial and temporal dimensions when the melting rate is unknown. We need to develop a one-dimensional runway deicing model.

The main objective of this research is to elaborate a numerical method for runway deicing process to predict ice melting rate and surface temperature for a given deicer and runway conditions. This overarching goal will be accomplished through the pursuit of three specific sub-objectives:

1. Determine an effective mathematical model and the numerical method for addressing the phase change problem.

2. Develop a melting model that takes into account the influence of chemical deicers and apply it to the runway deicing products (RDPs) and validate their performance against experimental data.

3. Apply the runway conditions—such as radiation heat, wind velocity, runway pavement temperature, and typical ice thickness on the runway—to the developed model.

In terms of the mathematical framework, we have employed the classical Stefan problem, which involves two phases (Myers et al., 2020). To solve this problem, we utilize the enthalpy method, a front-capturing scheme, which allows for the prediction of temperatures within both solid and liquid regions (Swaminathan & Voller, 1993). Previous applications of the enthalpy method have primarily focused on Stefan problems with constant melting points, across both space and time.

**Thesis Outline**

Chapter 1 of the thesis establishes the groundwork by examining relevant research on deicing models and phase change phenomena. It begins with an overview of chemical deicing approaches and follows with a review of literature on the two-phase Stefan problem, focusing on both pure and impure materials. Additionally, it explores the use of the enthalpy method for the simulation of melting processes, including its application in mixture solidification models. The chapter also reviews experimental studies related to deicing phenomena and the relationship between deicer concentration and melting point depression. This literature review serves to position this research within the broader field, identifying gaps and setting the context for the thesis's unique contributions.

Chapter 2, the methodology chapter, outlines the theoretical and computational framework used to develop the runway deicing model. It begins with an overview of the problem, emphasizing the need for a reliable model that simulates ice melting under chemical treatment. The two-phase Stefan problem forms the basis of the mathematical model, modified to account for impure materials and melting point depression due to varying concentrations of deicer. This model is combined with Fick's law to capture mass diffusion effects, allowing for an integrated treatment of both heat and mass transfer at the ice-deicer interface. To solve this setup, a finite volume discretization is used to transform the continuous equations into a discrete system manageable for computation, while the enthalpy method accommodates the latent heat of fusion, enabling seamless modeling of the phase change process. The chapter also discusses boundary and initial conditions, parameter calibration, and the computational implementation in MATLAB, with a mesh density study ensuring numerical accuracy and stability. This approach balances physical detail and computational efficiency, offering a tailored model for simulating the effects of deicing agents under runway conditions.

Chapter 3, the results chapter, presents findings from the runway deicing model, structured into four key sections. First, the verification section confirms the model's foundational accuracy using benchmark comparisons, including the Neumann similarity solution for pure

material melting without deicer, followed by a review of outputs such as temperature, melting front location, and enthalpy under deicing conditions. In the validation section, simulated results—temperature, mass of melted ice, and solution concentration—are compared to experimental data for Potassium formate and Potassium acetate at specified temperatures, ensuring alignment with the mass of ice melted and the temperature of the deicing solution. These comparisons are made using specific amounts of deicer and ice tested under controlled environment room conditions, and the error between the simulated and experimental results is calculated. The critical parameter analysis examines how core factors, such as the heat convection coefficient, initial deicing solution thickness, and melting temperature, impact model results, highlighting influential variables. Finally, runway condition analysis applies the model to real-world runway conditions, assessing deicing performance across variables like surface temperature, melting rate, and the effects of deicer reapplication under different temperature and environmental condition.

# CHAPITRE 1

# LITERATURE REVIEW

The introduction section provided a concise overview of the runway deicing procedure, describing the deicing chemicals used and their adverse effects on both the environment and aircraft. It also highlighted the research problem, emphasizing the necessity for the development of a mathematical model aimed at improving the use of deicing chemicals to minimize environmental pollution. The aim of this thesis was also articulated as the creation of a mathematical model and a numerical method to evaluate the efficacy of chemicals utilized in the de-icing procedures on runways.

This chapter reviews contemporary research to establish the contribution of this thesis in relation to previous works. Specifically, it substantiates the selection of the two-phase Stefan problem as a mathematical model, the utilization of the enthalpy method for the simulation of the melting process, and its integration with deicer mass diffusion. The first section (1.1) delves into chemical deicing models, providing an overview of existing approaches. The literature on the phase change problem is then reviewed in Section 1.2, which is divided into three subsections: 1.2.1 discusses the Stefan problem for pure and impure materials, 1.2.2 covers the application of the enthalpy method in phase change numerical models, and 1.2.3 examines mixture solidification models using the enthalpy method. Section 1.3 reviews existing experimental tests related to deicing phenomena, highlighting the methodologies and findings that inform current practices. Finally, Section 1.4 presents literature on calculating melting point depression based on concentration, shedding light on the chemical aspects of the deicing process.

## 1.1 Chemical Deicing Models

Over the last 20 years, researchers have explored the impact of chemical agents on the melting process through various approaches. This includes the development of a straightforward thermodynamic model for melting ice with salt, which provides a fundamental understanding of the phase change dynamics when salt is introduced (Potapova, 2012). This model offers

insights into the depression of the freezing point, which is a critical factor in the effectiveness of salt as a deicing agent.

Further comparative studies have been conducted to differentiate the processes of melting ice using pure water versus a salt solution (Klein-Paste & Potapova, 2014). They measured the mass of ice melted over time and the rate of temperature change within the ice layer. The acceleration of the melting process was quantified by monitoring the time taken to achieve complete melting under controlled conditions.

Moreover, comprehensive investigations have delved into the solution behaviors of four specific chemicals: sodium chloride (NaCl), magnesium chloride ($MgCl_2$), calcium chloride ($CaCl_2$), and potassium formate (KFO). These chemicals are commonly used in ground deicing due to their varying melting properties and low environmental impacts. Utilizing thermodynamic theory, along with an activity model for aqueous solutions, researchers calculated key properties relevant to winter maintenance, such as freezing point depression and melting capacity. Freezing point depression refers to the lowering of the freezing point of water when a chemical is added, which is crucial for preventing ice formation. Melting capacity, on the other hand, measures the ability of a chemical to melt ice at various temperatures. This theoretical approach aids in predicting the performance of these chemicals under different conditions. In one detailed study, the focus was on three common chloride salts – NaCl, $MgCl_2$, and $CaCl_2$ – assessing their effectiveness by measuring the speed and extent of ice melting under controlled conditions and evaluating their potential environmental ramifications. (Wåhlin et al., 2017).

Mathematical models have played a crucial role in optimizing the utilization of deicing chemicals in the ground transportation industry. These models, which predict road surface freezing, are essential tools for informing and improving salt application procedures, thereby enhancing road safety during winter. The methodologies applied in these models vary, relying on different physical methods, with the majority employing heat balance methods. These methods analyze the heat and water balance on road surfaces, taking into account variables

such as melting, freezing, evaporation, rainfall, frost, and snowfall under different surface conditions (dry, wet, or ice-covered). (Dan et al., 2020; Denby et al., 2013; Fujimoto et al., 2014).

Fujimoto et al. (2014) study introduced a road surface freezing model incorporating heat, water, and salt balances to simulate ice melting on roads. Validated through field experiments, this model accurately forecasts road surface conditions during freezing temperatures by considering factors like heat transfer, water infiltration, and the impact of salt application. The measured road surface conditions included surface temperature, ice thickness, moisture levels, and salt concentration.

Dan et al. (2020) developed a Water-Ice-Salt model to explore the dynamics of road surface conditions. This model provides a detailed understanding of the interplay between water, ice formation, and salt application rates, with an emphasis on how these factors influence pavement conditions and the broader environment. The environmental measurements included factors such as air temperature, wind speed, salt dispersion patterns, and the impact on surrounding soil and water quality. By incorporating wind effects, the study sheds light on the complex interactions between salt application strategies and the ecological implications of winter road maintenance.

Nuijten (2016) made a significant contribution to winter runway maintenance practices through a case study focused on predicting runway temperatures at Oslo Airport in Norway. By integrating meteorological data, runway surface characteristics, and a mathematical model, the study forecasts surface temperatures under winter conditions several hours in advance. Validated with observed surface and subsurface temperatures and SNOWTAM data, the model demonstrates a root mean square error (RMSE) of 1.65 °C, with enhanced accuracy (1.40 °C RMSE) early in the winter season.

These mathematical models are zero-dimensional in space and forecast average values over time within the system under consideration. Additionally, all these models presume a known melting rate rely on experimental data for its determination.

## 1.2 Phase Change Models

The runway chemical deicing process involves both spatial and temporal dimensions, with the melting rate varying based on the concentration of deicing chemicals. To model this, a one-dimensional approach is minimally necessary. Phase change models can estimate the melting rate variation in time and space.

The classical Stefan problem (Zeneli et al., 2021) provides a foundational framework for determining the melting rate, where the melting temperature is constant, and the concentration is uniform in both the liquid and ice phases without considering mass diffusion. Initially, we will review the literature on the classical Stefan problem, examining its assumptions and applications. This review will cover the fundamental principles and the development of solutions under these simplified conditions.

Because in our scenario the concentration is not uniform in space, the concentration in the liquid phase decreases as the ice melts. This non-uniformity in concentration affects the melting process, and as a result, the deicing process involves complexities not addressed by the classical Stefan problem. Specifically, it requires the incorporation of mass diffusion due to the high concentration in the deicing solution and near-zero concentration in the ice. Therefore, we will delve into literature that extends the Stefan problem to account for non-constant melting temperatures and mass diffusion. This review will focus on how these factors influence the phase change process and the methodologies developed to handle these complexities.

In the second subsection, we will examine the numerical method chosen to address the phase change problem: the enthalpy method. Previous studies on the enthalpy method have primarily

focused on pure materials with constant melting temperatures. In contrast, our model must handle the phase change problems involving impure deicing solutions, which exhibit variable melting temperatures dependent on concentration. We will discuss the relevant literature on the enthalpy method, particularly its application to the solidification process of such solutions. This review will include an analysis of the strengths and limitations of the enthalpy method in handling phase change scenarios with the complexities of non-constant melting temperature in space and time, and how it can be adapted to our specific needs.

### 1.2.1 Stefan problem

Many crucial heat conduction problems in science, nature, and engineering involve phase changes caused by melting or freezing. These are mathematically known as moving phase boundary problems, where the position of the interface is unknown and must be determined as part of the solution. The Stefan problem, which addresses ice melting, is the most common example. This problem is an interface problem for the heat equation, a parabolic partial differential equation, and is called a free boundary problem. It was first introduced by Lamé and Clapeyron (1831) and described by Stefan (1891) who studied the melting of polar ice in 1889. Additional historical details on Stefan's modeling of ice melting are available in (Problem & Vuik, 1994).

There is a literature on the Stefan problem, including three notable books that provide in-depth explanations. Alexiades and Solomon (1993) seminal work on the mathematical modeling of melting and freezing processes presents a comprehensive treatment of the Stefan problem. Their book covers both theoretical and practical aspects, including the derivation of governing equations and the application of numerical methods for solving these equations. The authors also discuss various boundary conditions and their impact on the solution. They discuss numerical and analytical methods used to solve the Stefan problem, emphasizing its importance in accurately predicting phase change phenomena. The Stefan problem book written by Rubinšteĭn (2000), offers a comprehensive exploration of the Stefan problem, covering both classical and contemporary approaches. The text covers a wide range of topics,

from the fundamental principles to advanced mathematical techniques for solving the problem. Gupta (2017) book offers a thorough exploration of the basic concepts and mathematical foundations of the classical Stefan problem. Gupta's work is particularly valuable for its detailed analysis of boundary conditions and the formulation of the problem in 1D,2D, and 3D.

Recent articles have further advanced the understanding of the Stefan problem using different boundary conditions and techniques. Turkyilmazoglu (2018) revisits traditional Stefan problems by examining how solidification and melting occur in a moving bar (medium) that is undergoing phase changes. The research reveals multiple solutions for the phase change interface movement and offers explicit solutions under various initial boundary conditions.

The article written by Groot (2018) reviews the Stefan problem of solidification from a mixture and its primary numerical methods. It highlights the challenges of simulating this problem in 2D or 3D on a regular grid, where a sharp solid–liquid interface moves relative to the grid. Groot introduces a new simulation method that conserves mass and tracks the interface motion with second-order accuracy in grid size. The method shows promising results in 1D simulations and is adaptable to 2D and 3D, enabling large-scale simulations with modest computational resources.

Koga and Krstic (2020) work focuses on a mathematical approach to control how heat moves through materials for the two-phase Stefan problem. They developed a method called energy shaping, which adjusts the energy in the system to ensure that the boundary between the solid and liquid phases stays stable. Their approach is designed to remain effective even when there are uncertainties in the system's parameters, and they back up their claims with simulations.

To provide a comprehensive review of the literature on the Stefan problem considering mass diffusion, we can mention the article by Zhao et al. (2020). This study addresses the challenge of accurately simulating the movement of the interface between different phases in heat-transfer-controlled or diffusion-controlled phase transformations. The authors propose a control volume method that significantly improves mass conservation during calculations.

Their method achieves a maximum relative mass conservation error of less than $10^{-13}$, compared to the conventional Stefan condition discrete equation's error of around $10^{-2}$.

Three articles by Myers address variable melting temperature. The article by Myers and Font (2015) addresses the Stefan problem where the phase change temperature is not constant. The authors identify errors in previous analyses, such as those by Evans and King (2000), which used an incorrect Stefan condition formulation. They present energy-conserving reductions for cartesian, cylindrical, and spherical symmetry problems and compare these solutions to those of the two-phase problem. Their work aims to correct and improve the understanding and solutions of such phase change problems.

The article by Myers (2016) presents a revised Stefan condition that accounts for latent heat release and temperature depression at reduced scales. The author demonstrates that previous formulations of the Stefan problem for nanoscale melting were incorrectly specified. Earlier models, such as model by Font and Myers (2013), predicted very rapid melt times for nanoscale particles, on the order of picoseconds, but this revised formulation suggests that the melt rates may be even faster. This could imply that the standard heat equations used in those models might not be accurate at such small scales.

The article by Myers et al. (2020) explores the Stefan problem with varying thermophysical properties for each phase and changes in the phase-change temperature depending on the size of the nanoparticle or the velocity of the phase change process. Specifically, "size" refers to the dimensions of the nanoparticle, which can affect its melting temperature and other properties due to the high surface-to-volume ratio. "Velocity" pertains to how fast the phase change occurs, which can be influenced by the conditions of supercooling or heating. The study formulates governing equations for both one-dimensional and spherically symmetric nanoparticle melting. It also examines the limitations of using Fourier’s law at small scales and proposes an improved model that incorporates finite heat carrier travel time.

### 1.2.2 Enthalpy Method

One of the viable approaches to simulate a Stefan problem involving solidification-melting is the fixed-domain method. This method is characterized by its simplicity, as it involves solving a single energy equation for both phases while implicitly tracking the melting front position (Bhattacharya et al., 2002). Within the front capturing method, two prominent techniques include the heat capacity and the enthalpy method. Among these, the enthalpy method, pioneered by Voller and Prakash (1987), stands out as the most widely used in phase-change simulations. It is particularly prevalent in commercial software packages and will be the primary focus of analysis in this section. We can refer to the article by Eyres et al. (1946) as the pioneering use of the enthalpy method, employed to address nonlinearity in a heat conduction scenario. The publication by Alexiades and Solomon (1993) offers a comprehensive examination of the mathematical principles and real-world applications associated with melting and freezing phenomena. It explores a range of mathematical models utilized to depict processes of melting and freezing, including the Stefan problem, as well as advanced numerical techniques like the enthalpy method employed in solving phase change.

Furthermore, Dusinberre (1945) employed the enthalpy method to address a phase change issue. One significant feature of the enthalpy method is its capacity to include the solid-liquid interface seamlessly within the solution, obviating the necessity for explicit tracking. Ayasoufi (2004) extensively elaborated on this aspect in her doctoral thesis.

The article of Sultana et al. (2018) conducts a thorough examination of mathematical formulations and boundary conditions essential for numerical predictions of solidification and melting phenomena, with a specific focus on techniques pertinent to modeling solid-liquid interfaces. Their review centers on the fixed grid enthalpy method, which provides solutions for phase change problems involving both conduction and convection processes. Moreover, Henry and Stavros (1996) provided an overview of the primary mathematical modeling techniques for solidification and melting issues, including the enthalpy method, in their paper. In the publication authored by Tarwidi (2019), it was determined that the approximation of

interface position using the enthalpy method with finite element discretization is more accurate compared to the approximation achieved using the Godunov method.

Some investigations have incorporated the enthalpy method alongside other numerical techniques to improve the model's accuracy. In the paper authored by Beckett et al. (2001), an adaptive moving mesh method is devised for numerically solving an enthalpy formulation of two-dimensional heat conduction problems involving phase change. The enthalpy equation is discretized employing a semi-implicit Galerkin finite element method based on linear basis functions.

The paper authored by Esen and Kutluay (2004) employed an enthalpy formulation using finite difference approximations to address the one-dimensional Stefan problem with a Neumann condition at the fixed boundary. Gudibande and Iyer (2013) introduce the cell splitting technique within the enthalpy method framework. This method effectively eliminates waviness and eliminates the need for mushy zone constants when simulating melting with natural convection. The method's efficacy is demonstrated through a simple one-dimensional melting problem, with results compared against analytical solutions. Additionally, Gudibande and Iyer (2017) expanded their method to simulate contact melting. In this paper, they employed a moving grid methodology to prevent the diffusion of the solid-liquid interface caused by the downward motion of the solid.

In recent three years, researchers have extensively investigated the enthalpy method for phase change problems. One notable contribution is the article by Roscani and Voller (2024), which develops an enthalpy-based approach to address the Stefan problem using time fractional formulations. This study introduces memory-enthalpy formulation. They verified their model by ensuring thermodynamic consistency, providing a continuous heat flux across the melting interface, and offering mathematical equivalence to existing memory-flux formulations.
Another valuable contribution is the article by König-Haagen and Diarce (2023). This study evaluates different enthalpy methods for solving solid/liquid phase change problems. They differentiate between "corrected" and "uncorrected" enthalpy methods. The corrected methods

involve adjustments to improve numerical stability and accuracy, such as iterative corrections of the temperature/enthalpy relation. The study highlights that these corrected methods, including the "optimum approach," generally provide better accuracy and efficiency compared to traditional, uncorrected methods. In contrast, uncorrected methods, like some classical apparent heat capacity approaches, often suffer from stability issues, particularly with larger time steps. The paper demonstrates that the corrected methods offer significant improvements in handling the phase change front and provide more reliable results across different scenarios. They categorize different enthalpy methods based on their characteristics which is shown in table 1.1.

Table 1.1 Different enthalpy methods based on their characteristics

| Enthalpy method | |
|---|---|
| Explicit | Implicit |
| Uncorrected | |
| Explicit apparent heat capacity method | Implicit apparent heat capacity method |
| Corrected | |
| • Basic explicit method<br>• Explicit version of Pham's method | • One correction: Pham's method<br>• Iterative correction: Optimum approach, Source-based method |

Another investigation on the enthalpy method is presented in the article by Vasil'ev et al. (2021). This study focuses on numerically solving the two-phase Stefan problem using an enthalpy-based approach. To enhance stability and accuracy, the authors emphasize smoothing the coefficients that represent thermal properties, such as heat capacity and thermal conductivity, near the phase change interface. This smoothing process is critical because sharp discontinuities at the phase change boundary can cause numerical instabilities and inaccuracies in the simulation. By gradually adjusting these coefficients across the interface, the method reduces abrupt changes, which improves both the stability of the computational process and the precision of the results.

All these studies pertain to the enthalpy method applied to pure materials. Therefore, after examining the utilization of enthalpy for the solidification and melting of materials without impurities, we now need to explore literature concerning mixtures rather than pure substances. This is necessary as we aim to develop a model for the melting process involving deicer chemicals. Since there is a lack of literature on using the enthalpy method for melting solid ice with deicing solutions, we present literature focusing on the solidification of chemical solutions instead.

### 1.2.3 Mixture Solidification Model with Enthalpy Method

The presence of solute in the liquid results in a decrease in the solution's melting temperature. One of the first articles to utilize the enthalpy method for the solidification process of binary alloys is the article by Prakash and Voller (1989). They address numerical aspects related to solving the continuum mixture model equations to analyze phase change problems involving binary materials transitioning between solid and liquid states. In the publication by Swaminathan and Voller (1992), the authors introduce a universal implicit source-driven enthalpy method for analyzing solidification systems. The key distinction in their proposed approach, compared to previous source-based methods, is the consistent linearization of the discretized source term. This ensures optimal convergence, meaning that the numerical solution achieves stability with minimal iterations, regardless of varying conditions such as different grid sizes, time steps, or material properties.

Following that, Voller (2008) introduced the developed model, which is an enthalpy fixed grid method designed for simulating dendritic growth in an under-cooled binary alloy. The paper authored by Jamil et al. (2006) introduces a model for heat transfer during the melting of saline binary solutions. The model they utilized is founded on an enthalpic formulation and applied to calorimetry to ascertain the kinetics of eutectic melting. Model validation was conducted to ascertain the temperature within the sample of the differential scanning calorimetry (DSC).

We can highlight the study by Bhattacharya et al. (2002), which integrated the enthalpy method with other numerical techniques to improve accuracy in modeling the melting and solidification of binary solutions. This study applied the enthalpy method to investigate the melting of frozen brine and ice slabs, focusing on capturing the temperature profiles and phase change fronts accurately. In this context, accuracy refers to the method's ability to closely match analytical solutions for temperature and front positions, especially in capturing sharp interfaces within 1D simulations. The enthalpy method modeled multiple phase change fronts in finite ice and brine slabs, demonstrating reliability in representing the detailed melting process without requiring phase interface tracking.

The studies reviewed highlight the versatility and adaptability of the enthalpy method in capturing complex phase changes under various conditions. Given this, the enthalpy approach combined with a finite volume discretization offers an appropriate balance between computational feasibility and the physical accuracy required for runway deicing applications. By focusing on a 1D setup, this study prioritizes the critical vertical axis of heat and mass transfer, which governs the ice thickness and deicer distribution, reducing computational demands compared to 2D or 3D models. This choice allows us to simulate large-scale systems, like runway surfaces, where ice and deicer layer interactions play a central role.

Unlike experimental setups that face challenges in environmental control and scalability, this numerical approach enables a direct assessment of how temperature, concentration gradients, and melting rate evolve over time, particularly in the presence of deicer. Calculating melting front progression, along with the associated mass of melted ice, provides insights that are difficult to measure experimentally, particularly in large-scale scenarios. The outcome of this numerical study, therefore, is a detailed assessment of how much ice will melt under specific conditions, offering a scalable solution applicable to runway deicing with customizable inputs for different deicers and climate conditions.

In the subsequent section of this chapter, our aim is to provide an overview of experimental investigations pertaining to the ground deicing process.

## 1.3 Experimental Models

Understanding product performance is crucial for determining the appropriate quantity of deicing product needed based on ground conditions. Consequently, laboratory tests of deicing products must be conducted under controlled and known conditions.

The handbook authored by Chappelow et al. (1992) serves as a comprehensive resource for evaluating chemical deicers. This handbook defines 62 specific test methods for the complete characterization of deicing chemicals, organized into eight principal performance areas: physicochemical characteristics, deicing performance, compatibility with metals and concrete, engineering parameters, ecological effects, and health and safety aspects. Among these, 12 primary test methods are emphasized for critical evaluations, including ice melting tests, ice penetration tests, and corrosion tests for metals and concrete.

Blackburn et al. (2004) offers guidelines for choosing snow and ice control strategies and tactics suitable for various winter maintenance conditions. These guidelines are applicable to highways, roads, streets, and other paved surfaces.

Melinder (2007) explores the thermophysical properties of various aqueous solutions employed as secondary working fluids in thermal systems The study provides detailed analysis and data on properties such as density, viscosity, thermal conductivity, and specific heat capacity, which are essential for optimizing the performance and efficiency of thermal systems. Akin and Shi (2012) present the creation of standardized laboratory tests to assess the effectiveness of deicing chemicals. The study outlines the methodologies for evaluating key performance metrics such as ice melting capacity, ice penetration, and undercutting capabilities.

Gerbino-Bevins et al. (2012) examine the ice-melting capacity of various deicing chemicals through laboratory tests conducted under controlled conditions. The study compares the amount of ice melted by different deicers at various concentrations and temperatures (0°F,

10°F, and 20°F). The findings reveal that higher concentrations of liquid deicers result in greater ice melting, and the results from their shaker test correlate well with limited field data from Nebraska. This study contributes to understanding the practical implications of using different deicing agents in winter road maintenance.

Brassard et al. (2019) provide a review of various runway deicing products, focusing on their ability to prevent and remove ice from airport runways. The study evaluates the performance of these products using specific metrics, including repeatability of results across three established methods outlined in the AMS documents for assessing deicing. The aerospace standard AS6211 is used to evaluate the performance of a Runway Deicing Product (RDP)(Committee, 2021).

Kulyakthin and Klein-Paste (2021) investigate the use of calorimetry as a method for measuring the melting rate of deicing agents. Their study evaluates whether this thermal analysis technique can accurately assess how quickly deicers melt ice under controlled conditions. The findings reveal that calorimetry allows for the continuous measurement of melting rates of various deicers, such as $CaCl_2$ and $MgCl_2$, throughout the melting process without interfering with it. However, the study also notes that determining the exact melting rate can be complicated due to uncertainties in the concentration of deicers in meltwater, which can affect the heat balance calculations. While calorimetry shows promise as a measurement tool, the limitations in distinguishing between different deicers highlight the need for improvements in the assumptions and measurement techniques used in the process.

Charpentier et al. (2022) present an improved method for assessing the performance of de-icing products on airport runways. Their study refines existing aerospace standards for evaluating runway de-icing product (RDP) performance, aiming to provide more detailed insights into the melting and penetration characteristics of these agents under controlled conditions.

In a subsequent study, Charpentier et al. (2023) introduce a dynamic ice penetration model for RDPs, grounded in experimental data and based on the AS6211 protocol. This model allows for more reliable predictions of ice melt rates over time, capturing nuances such as the effect of concentration on melting curves and challenges like air bubble formation during testing. Compared to earlier models, this approach accounts for temporal variations in de-icing performance, which traditional static models overlook, thereby providing a more comprehensive tool for understanding and comparing RDP efficacy.

## 1.4 Melting temperature

In the following, we present research on determining the melting temperature for chemical deicing solutions. This step is crucial because the melting temperature varies with the concentration of the solution, influencing the phase change dynamics that the model aims to capture. By incorporating concentration-dependent melting temperatures, the model can better represent the behavior of deicing solutions in real conditions, especially when evaluating how different concentrations impact the melting rate and the extent of ice removal on surfaces.

One of the primary studies in this area was conducted by Prakash and Voller (1989). Their article addresses the numerical modeling of binary solid-liquid phase changes. They developed a continuum mixture model to describe the phase change process, incorporating the effects of varying concentration on the melting temperature. The study focuses on modeling the coupled heat and mass transfer phenomena to predict the phase change behavior of binary mixtures.

Another relevant article is by Bennon and Incropera (1987), where a continuum model describes momentum, heat, and species transport in binary solid-liquid phase change systems. This study is particularly useful in deriving the relationship between melting temperature and concentration, which aids in simulating the impact of varying deicer concentrations on phase change dynamics.

Recently, Lamas et al. (2022) examined freezing point depression in salt solutions, using the Madrid-2019 model to account for different salt concentrations. This study provides a refined approach for estimating freezing points, clarifying the effects of concentration on temperature depression—a critical factor to incorporate in the study for modeling of deicing solutions under various concentrations.

## 1.5 Conclusion

Despite advancements in modeling deicing processes, key limitations remain in existing studies that hinder their applicability to real-world scenarios. Chemical deicing models assume uniform temperature distributions across the ice and deicer layers, simplifying the geometry but overlooking the spatial variations critical to predicting melting behavior, particularly when deicing chemicals diffuse into the ice and initiate melting. Additionally, melting rates in previous models are derived from experimental data rather than predictive formulations that dynamically link melting rates to temperature and concentration changes. Consequently, such models require experimental tests for each deicing chemical to determine its melting rate.

Another significant gap lies in the absence of diffusion modeling. Deicer diffusion into the ice, which directly impacts the melting process, is not incorporated into existing frameworks. Coupling heat and mass transfer is essential to better capture the interplay between thermal and concentration gradients during melting. This requires incorporating mass diffusion, driven by the high concentration in the deicer solution and the near-zero concentration in the ice. Moreover, classical phase-change models, the Stefan problem and the Enthalpy method, assume a constant melting temperature—an assumption applicable only to pure materials like water. For deicer-ice systems, the melting temperature varies with concentration. While advanced Stefan problem formulations and Enthalpy methods for mixtures account for some complexities, they focus on solidification processes. They do not consider the melting process or the diffusion of deicing chemicals into the ice, which is a crucial factor in the deicing process.

Finally, while deicing studies for roads, sidewalks, and railways provide valuable insights, they do not address the unique challenges of runway deicing. Runway-specific conditions, such as variations in surface temperature, environmental influences, the use of specific runway deicing products (RDPs), and the deicer reapplication, are not sufficiently considered. This limits the applicability of existing models to aviation contexts.

This thesis addresses the limitations of previous models, which assume a melting rate based on empirical results, by developing an enhanced model that correlates melting rate variations with temperature fluctuations driven by deicer concentration. By extending the classical Stefan problem to accommodate variable melting temperatures and non-uniform concentrations, this work advances the theoretical framework for understanding deicing processes. Additionally, the proposed model integrates experimental data to reflect the complexities of runway deicing, offering an approach that bridges theoretical and practical aspects in this area.

# CHAPITRE 2

# MODEL AND METHODOLOGY

In this chapter, we introduce the mathematical models utilized in the development of the runway deicing model. In the first section, we provide an overview of the problem, detailing its scope and significance. In the second section, we present the mathematical model chosen to address the phase change phenomena, with a focus on the two-phase Stefan problem, followed by a discussion of the modifications made to tailor the model to our specific requirements. The third section is dedicated to the numerical method employed to solve the mathematical formulation. This section will also cover the discretization method used to translate the continuous problem into a discrete form suitable for computational analysis. The chapter aims to offer a comprehensive understanding of the theoretical framework and computational approach adopted in the development of the deicing model.

The primary model employed in this study draws its foundations from the model exposed in the book authored by Alexiades and Solomon (1993). Their model is rooted in the classical formulation of the two-phase Stefan problem, primarily tailored for pure materials. This foundational framework serves as the basis for our investigation into the dynamics of phase change phenomena and provides a theoretical underpinning for our analysis and modeling endeavors.

## 2.1 Problem Definition

Figure 2.1 depicts the schematic representation of the problem under consideration. The illustration showcases a runway surface, which is coated with a layer of ice or snow. Additionally, there exists a deicer application layer atop the ice/snow layer, strategically applied to induce the melting of the icy surface. Moreover, the weather conditions pertinent to the airport runway are visually depicted in the figure, providing insights into the environmental factors influencing the deicing process.

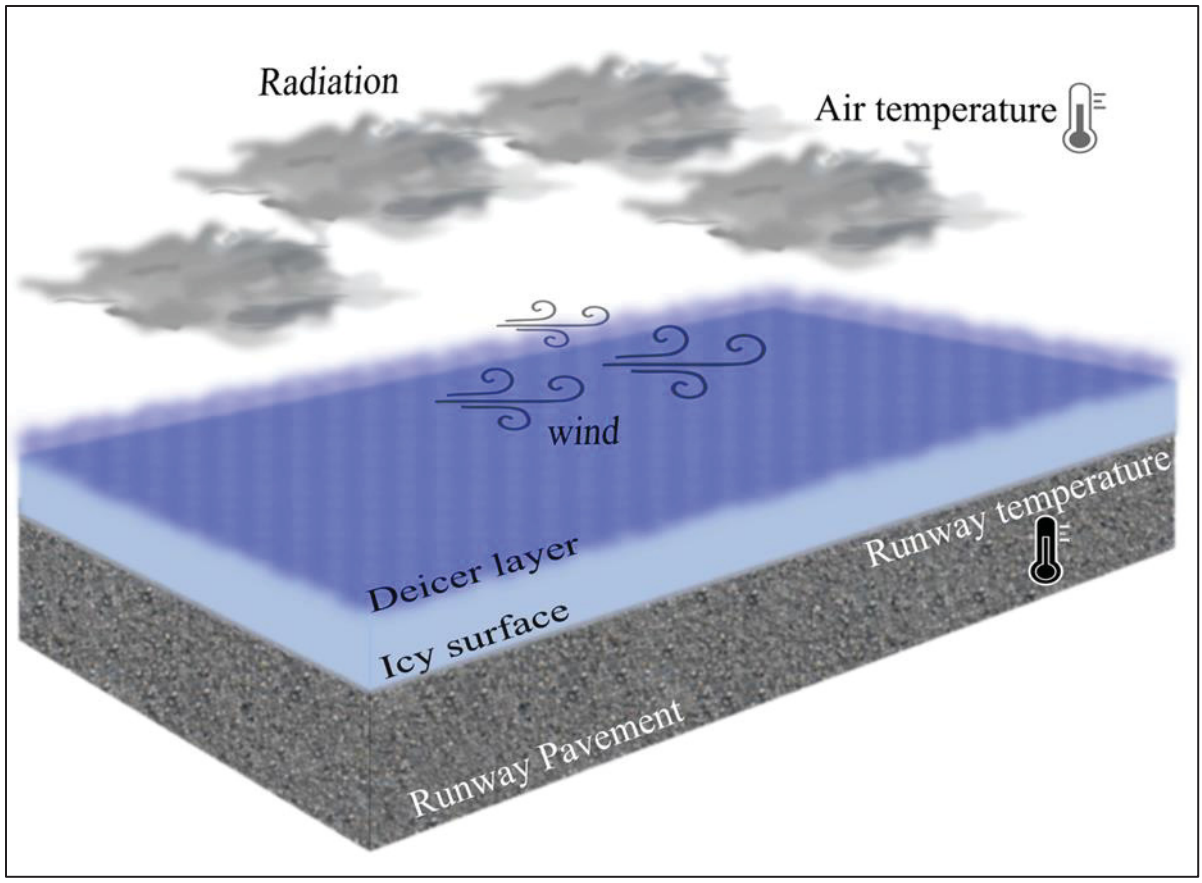


Figure 2.1 Scheme of the physical problem under study

As observed, our analysis incorporates multiple factors contributing to the overall heat and mass flux dynamics within the system. Specifically, we account for the imposed temperature from the runway pavement. Furthermore, the heat transfer coefficient includes the combined effects of both convective heat flux, influenced by wind velocity, and radiation heat flux, both of which significantly impact the overall heat transfer process.

Phase change and melting phenomena occur within the interface between the two upper layers: the deicer layer and the ice layer. As such, our initial focus will be directed towards these layers to understand the underlying dynamics. Subsequently, in the next sections, we will proceed to elucidate the conditions and fluxes within these two upper layers, which collectively form the system under investigation in this study.

By analyzing the conditions and fluxes within the deicer layer and the ice layer, we aim to unravel the mechanisms governing the phase change process and melting dynamics at the interface. This approach allows for a detailed examination of the thermal transfer and the mass transfer phenomena.

In this thesis, assumptions are made within the model to reduce the complexity of the problem. Figure 2-2 provides an outline of the 1D problem within the runway deicing model. As depicted, the system comprises five distinct layers arranged from bottom to top: the runway pavement, the ice layer, the mushy region layer, the solution layer, and the atmosphere layer. Notably, from a physical perspective, the mushy region represents a thin zone where the solution penetrates and mixes with the ice. Consequently, this region contains both deicing solution and partially melted ice, neither fully solid nor entirely liquid. The mushy region is a vital stage in deicing because it helps break down the ice. The model replaces the mushy region with a sharp interface between solid and liquid (melting front). As the ice melts, the melting front location, denoted by the red line (X(t)), moves toward the runway pavement.

Within this system, two layers are identified as active, meaning their properties vary over time, namely the ice layer and the solution layer. In contrast, the properties of the remaining two layers, the runway pavement, and the air, are considered constant over time. Consequently, the domain of the problem encompasses these two active layers and the interface between solid and liquid (mushy region), while the steady-state layers serve as boundary conditions. The starting point of the problem (x=0) represents the area above the runway pavement, while the endpoint (x=L) marks the interface between the solution layer and the air. Within this setup, five distinct temperatures are discernible: the steady-state pavement temperature ($T_p$) and the air temperature ($T_\infty$), and the unsteady-state temperatures corresponding to the solid ($T_s$), the liquid ($T_l$), and the melting front ($T_m$). Notably, the melting front temperature, representing a mixture of ice and deicing solution, equals the melting temperature ($T_m$).

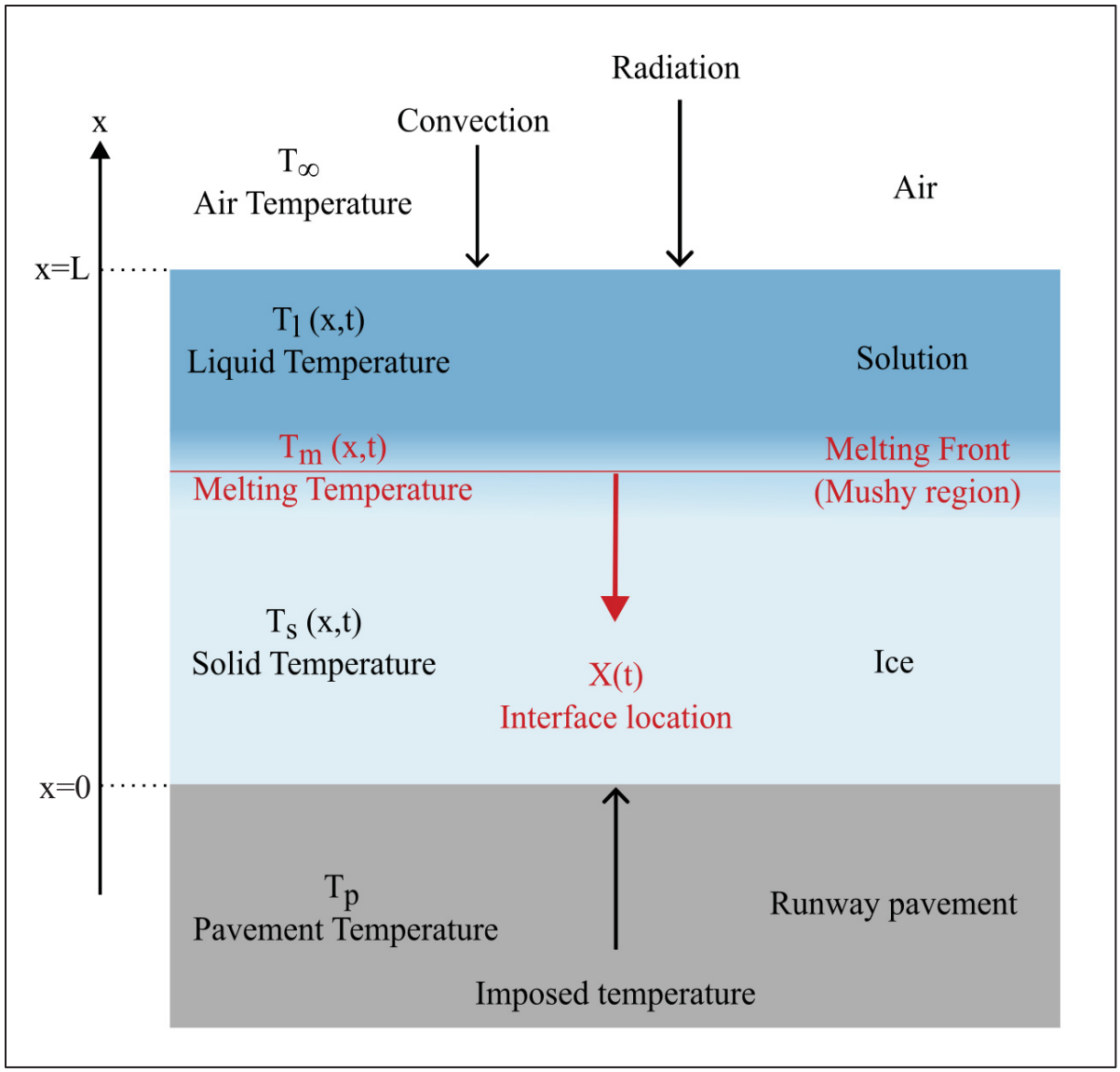


Figure 2.2 Schematic of the problem in 1D

As you can see in Figure 2.2, we consider the imposed temperature at the boundary between the ice and the runway pavement, as well as the convective and radiative heat flux between the atmosphere and the surface of the deicing solution. Solar radiation and momentum effects are neglected in the model. The properties of the deicing chemicals are obtained from experimental data.

## 2.2 Mathematical Model

The mathematical model employed here utilizes the Stefan problem to address phase change phenomena. We introduce a modification to the two-phase Stefan problem. This modification accommodates scenarios where the melting rate varies due to the presence of impurities (deicer) within the liquid region.

### 2.2.1 Stefan Problem

The phase-change problem presents a distinctive challenge as it involves the determination of both temperature distribution and the location of the interface between solid and liquid regions. Within each phase, a heat equation is formulated based on the specific properties of that phase, ensuring the conservation of energy. Like any other differential problem, solving the phase-change problem requires consideration of boundary and initial conditions. However, unique to this problem is the presence of interface conditions in addition to boundary and initial conditions. The interface serves as part of the boundary for both the liquid and solid regions, necessitating boundary conditions from each side to fully define the initial boundary value problem within each phase.

To address the phase change issue, we initiate our approach by employing the principles of energy conservation. The energy conservation equation, assuming the absence of any heat sink or source, is formulated as follows:

$$\frac{\partial E}{\partial t} + \nabla . q = 0 \tag{2.1}$$

where $E$ represents energy, $t$ signifies time, and $\mathrm{q}$ denotes heat flux.

The two-phase Stefan problem is a mathematical model used to describe phase change phenomena, such as solidification or melting, occurring at a moving interface between two phases. Consider our problem as a one-dimensional domain (figure 2.2), represented by the

interval $0 \leq x \leq L$, where x represents the spatial coordinate along the normal direction. Let *T(x,t)* denote the temperature distribution within the domain at time *t*, and let *X(t)* represent the position of the moving interface separating the solid and liquid phases. The mathematical model for the two-phase Stefan problem consists of several equations representing heat conduction, phase change, and interface motion. With subscript *s* denoting the solid and subscript *l* the liquid, the specific heat, $c_{p-s}, c_{p-l}$ , and the thermal conductivity, $k_s, k_l$, are constant in solid and liquid regions.

The enthalpy-temperature relationship which is shown is figure 2.3 is given by:

$$E = \rho c_p T + \rho L_f \lambda \tag{2.2}$$

which $c_p$ is the specific heat capacity at constant pressure, $L_f$ is the latent heat of fusion, and $\lambda$ is the liquid fraction, ranging from 0 (solid) to 1 (liquid). The density is the same in the solid and liquid region, $\rho = \rho_2 + \lambda\rho_1$.

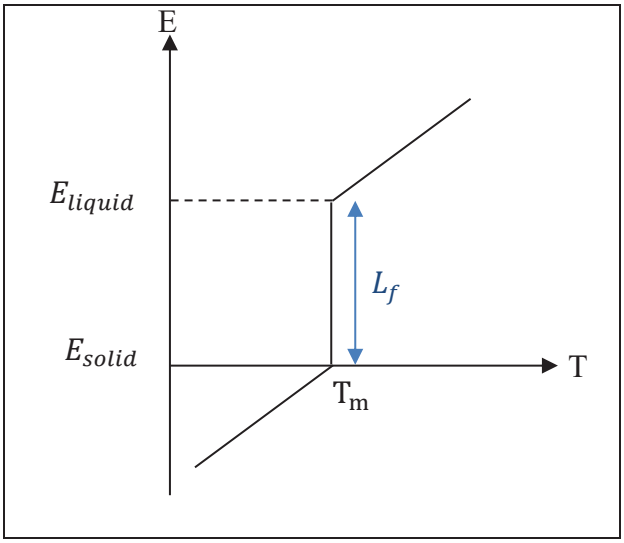


Figure 2.3 Enthalpy-temperature relationship

The total enthalpy can be given by

$$E = \begin{cases} \rho c_{p-s}[T - T_m] & for\ T < T_m \\ \rho c_{p-l}[T - T_m] + \rho L_f & for\ T > T_m \end{cases} \tag{2.3}$$

When $T = T_m$, it is a mushy region, and the enthalpy is $0 < E < \rho L_f$.

To relate heat transfer to temperature gradients, we apply Fourier's law of heat conduction for each phase:

$$q = -k_s \frac{dT}{dx} \quad \text{for} \quad 0 < x < X(t) \quad \text{(solid phase)} \tag{2.4}$$

$$q = -k_l \frac{dT}{dx} \quad \text{for} \quad X(t) < x < L \quad \text{(liquid phase)} \tag{2.5}$$

To solve the temperature equations, boundary conditions are needed. The initial conditions for temperature:

$$T(x, 0) = T_s\,, \ (solid\ region) \tag{2.6}$$

$$T(x, 0) = T_l\,, \ (liquid\ region) \tag{2.7}$$

For the space boundary conditions, at the bottom of the ice, x=0 (BC1), considering imposed temperature from the pavement:

$$T(0, t) = T_p \tag{2.8}$$

At the surface of the solution, x=L (BC2), a convection-radiation fluxes exist:

$$q = -k_l \frac{dT}{dx}(L, t) = q_{convection-radiation}, \quad t > 0 \tag{2.9}$$

the heat flux is calculated with an imposed heat transfer coefficient (h):

$$q_{convection-radiation} = h[T_\infty(\,t) - T(L, t)] \tag{2.10}$$

where $h$ is the heat transfer coefficient for combination of convection-radiation (Monteiro et al., 2011)

$$h = h_c + \varepsilon_s \sigma((T_\infty(\,t) + 273.15)^3 - (T(L, t) + 273.15)^3) \tag{2.11}$$

Where $\sigma$ is the Stephan–Boltzmann constant ($5.68 \times 10^{-8}$ W m$^{-2}$K$^{-4}$) and $\varepsilon_s$ is the surface emissivity. The values for the emissivity is based on (Nuijten, 2016).

The heat convection coefficient $h_c$ is calculated based on the wind velocity ($v$) (Seifeddine et al., 2022):

$$h_c = 5.6 + 4v \qquad for\ v \leq 5\ m/s \tag{2.12}$$
$$h_c = 7.2\ v^{0.78} \qquad for\ v > 5\ m/s$$

Additionally, at the interface between solid and liquid phases, we incorporate the Stefan condition for heat balance across the melting front ($t > 0$) (Myers & Font, 2015):

$$\rho\left[\left(c_{p-l} - c_{p-s}\right)\left(T_m(t) - T_{mpure}\right) + L_f\right]\dot{X}(t) \tag{2.13}$$
$$= -k_l \frac{dT}{dx}(X(t)^-, t) + k_s \frac{dT}{dx}(X(t)^+, t)$$

where $L_f$ is the latent heat of fusion, $\dot{X}(t)$ is the velocity of the melting front ($\frac{dX(t)}{dt}$), the value of $\frac{dT}{dx}(X,t)$ is $\frac{dT}{dx}\left(X(t)^{\mp}, t\right)$ when $x \to X(t)^{\mp}$ (two sides of melting front). $T_{mpure}$ is the melting temperature for pure material. The temperature at the melting front location:

$$T(X(t), t) = T_m(t)\,, \quad t > 0 \tag{2.14}$$

The melting temperature depends on the concentration of the solute. The melting temperature of the model is presented in detail in section 2.2.3.

This system of equations is the classical Stefan problem. Now we will present the mass transfer equations to compute the melting rate. In our model, the melting rate is unknown and varies with concentration. The classical Stefan problem assumes a uniform concentration in liquid and ice, without mass diffusion. Runway deicing necessitates a mass diffusion equation because of high concentration in the binary mixture and close to zero concentration into the ice.

### 2.2.2 Mass Diffusion

In addition to addressing the Stefan problem, our model incorporates solute mass conservation using Fick's law equations for mass concentration ($C$) to enable the ice melting. Without mass diffusion, the solute does not penetrate the solid and the melting point in the ice remains unchanged. The diffusion coefficients for the Fick's model take different values in the solid

and the liquid, $D_s \neq D_l$. The concentration gradient is formulated by Fick's second law as follows:

$$\frac{\partial C}{\partial t} = -\nabla . J \tag{2.15}$$

where $C$ represents mass concentration, $t$ signifies time, and J denotes diffusion flux. The diffusion flux (J) is calculated by Fick's first law for each region:

For the solid region

$$J = -D_s \frac{dC}{dx}, \qquad 0 < x < X(t)\,, t > 0 \tag{2.16}$$

and for the liquid region

$$J = -D_l \frac{dC}{dx}, \qquad X(t) < x < L\,, t > 0 \tag{2.17}$$

Initially, the deicer doesn't exist in the solid region (ice)

$$C(x, 0) = C_s = 0 \tag{2.18}$$

The initial concentration of solute in the liquid is:

$$C(x, 0) = C_l \tag{2.19}$$

The initial height of the solution $H_{initial}$, is based on the initial concentration of the solution.

$$H_{initial} = \frac{(1 - C_l)m_1}{C_l\, \rho A} \tag{2.20}$$

where $m_1$ is the mass of the deicer, and A is the area.

The initial melting front location is the equal to initial thickness of ice:

$$X(0) = X^0 = X_{ice\_initial} = X_{initial} \tag{2.21}$$

We consider that, there is no mass flux at the boundaries, so at x=0 and x=L,

$$-D_l \frac{dC}{dx}(0,t) = 0, \quad -D_l \frac{dC}{dx}(L,t) = 0 \tag{2.22}$$

At the interface between the solid and liquid regions, a concentration gradient occurs. The deicer penetrates the solid region by mass diffusion. Thus, at $t > 0$, the interface condition for mass diffusion can be expressed as:

$$[C_l(X(t)^-, t) - C_s(X(t)^+, t)]\dot{X}(t) \tag{2.23}$$
$$= -D_l \frac{dC}{dx}(X(t)^-, t) + D_s \frac{dC}{dx}(X(t)^+, t)$$

Here $C_s(X(t)^+, t)$ is the concentration of the deicer at the solid side of the interface, and $C_l(X(t)^-, t)$ is the concentration of the deicer at the liquid side of the interface. Additionally, we considered mass diffusion equation in liquid region $-D_l \frac{dC}{dx}(X(t)^-, t)$ and in the solid region $D_s \frac{dC}{dx}(X(t)^+, t)$.

The diffusion coefficient in the liquid $D_l$ is based on article written by Wåhlin and Klein-Paste (2017). For the solution penetration within the solid region, the diffusion coefficient $D_s$ is determined using the equation from Wilke and Chang (1955) mentioned in article by Wåhlin and Klein-Paste (2017)

$$D_s = 7.4e-8 \frac{\sqrt{\Psi_w M_w} T}{\eta^{sol} V_C^{0.6}} \tag{2.24}$$

where $\eta^{sol}$ is the viscosity of the solution, $M_w$ is the molar mass of the solvent, $\Psi_w$ is a solvent-specific empirical parameter, $V_C$ is a molar volume of the solute in the solvent at its normal boiling point, and T is the temperature (in Kelvin). This coefficient is crucial for initiating melting, as the deicer concentration is initially zero within the solid region.

### 2.2.3 Melting temperature

When studying phase changes in materials, particularly the melting behavior of impure substances, it is crucial to understand how impurities affect the melting point. In a binary solid-

liquid phase change, the presence of impurities can significantly alter the melting temperature from that of the pure substance. This can be mathematically described using the liquidus temperature equation, as detailed by Prakash and Voller in their work on continuum mixture model equations (Prakash & Voller, 1989).

The melting temperature of an impure material, $T_m$, can be approximated by the liquidus temperature equation:

$$T_m = T_{mpure} + \left(T_e - T_{mpure}\right)\left(\frac{C}{C_e}\right)^x \tag{2.25}$$

In this equation, $T_{mpure}$ is the melting temperature of the pure substance, $T_e$ is the eutectic temperature of the binary solution and $C_e$ is the eutectic concentration of the binary solution. In a eutectic system, the eutectic point represents the lowest temperature at which the mixture can melt or freeze, defined by the eutectic temperature ($T_e$) and the eutectic concentration ($C_e$). The liquidus temperature equation demonstrates how the melting temperature ($T_m$ ) varies with the concentration of the impurity ($C$). For simplicity, the power of the concentration slope (x) is based on the power fitting of the experimental phase diagram of deicer and water.

To better understand this equation, the qualitative behavior of the melting temperature as a function of impurity concentration can be visualized in the plot of the eutectic binary system phase diagram figure 2.4. In this plot, the vertical axis represents the melting temperature ($T_m$ ), and the horizontal axis represents the concentration of the impurity ($C$).

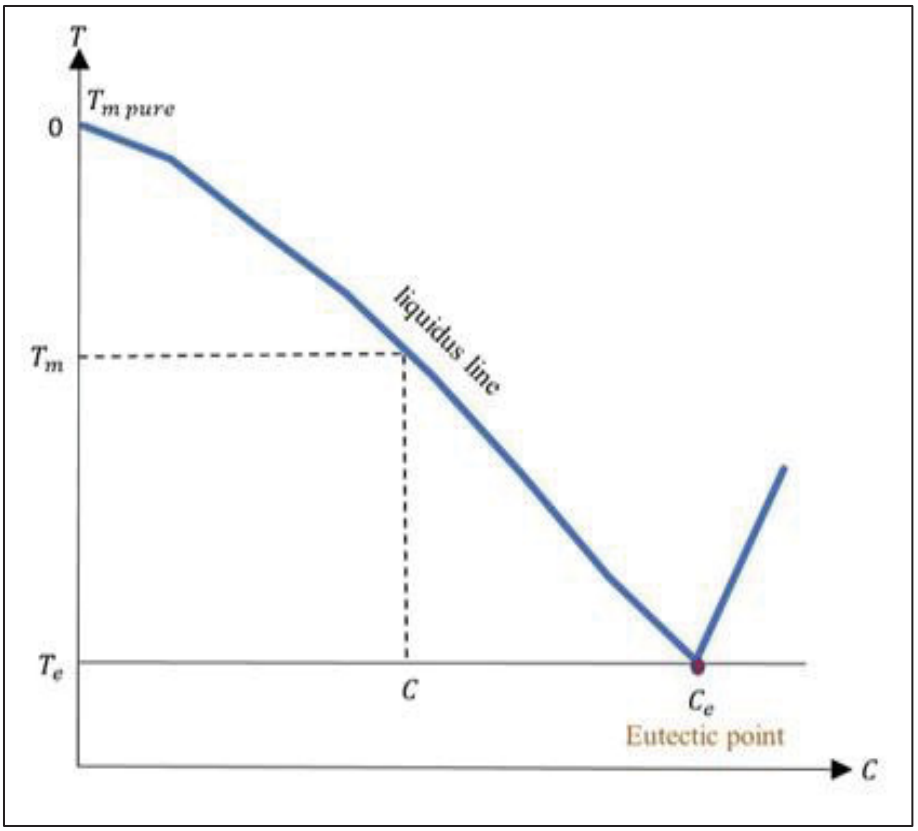


Figure 2.4 Phase diagram of eutectic water- chemical deicer

For pure ice, where $C = 0$, the melting temperature is at $T_{mpure} = 0$. As concentration of impurities $C$ increases, the melting temperature $T_m$ decreases towards the eutectic temperature $T_e$, reflecting the influence of the impurities. At $C = C_e$, the melting temperature reaches the eutectic temperature $T_e$.

## 2.3 Numerical Method

The enthalpy method is a numerical approach used to solve the Stefan problem, which involves phase changes like melting and solidification. This method considers both the temperature ($T$) and enthalpy ($E$) of the material, providing a unified framework for analyzing phase transitions. In this context, enthalpy represents the heat content per unit mass and is closely linked to the temperature through the liquid fraction ($\lambda$), indicating the proportion of the

material in the liquid phase (Esen & Kutluay, 2004). This relationship allows the method to smoothly transition between solid and liquid states as the temperature changes (equation 2.2).

A significant advantage of the enthalpy method is its natural incorporation of the Stefan condition, which describes the balance of heat at the boundary between solid and liquid phases. The enthalpy method ensures the Stefan condition (jump condition) is automatically satisfied by the way enthalpy changes with temperature and phase fraction, inherently maintaining the energy balance at the interface. By eliminating the need to track the moving boundary between phases, this method simplifies the computational process (Alexiades & Solomon, 1993). It integrates the behavior of both solid and liquid phases into a single framework, making it easier to implement and solve numerically.

In this thesis, the discrete problem is solved explicitly by applying a finite volume approach in 1D, using finite difference approximations for spatial and temporal derivatives. This approach involves discretizing both space and time to create a computational grid, as shown in Figure 2.5. Spatial nodes $x_1, \dots, x_j, \dots, x_M$ are distributed along the vertical axis, and temporal nodes $t_o, \dots, t_n, t_{n+1}$ are organized along the horizontal axis. The region is divided into a finite number of control volumes $V_j$, each of constant height $\Delta x$. Within each control volume, there is a midpoint node $x_j$ and endpoints $x_{j-\frac{1}{2}}$ and $x_{j+\frac{1}{2}}$, where $\Delta x$ represents the distance between these endpoints.

In each control volume, the governing equations are integrated over the volume $V_j$ and over a finite time interval $\Delta t$. This integration ensures that the conservation of energy is maintained within each control volume over each time step. Initially, the temperature, enthalpy, and mass concentration distributions are specified, along with appropriate boundary conditions. At each time step, the enthalpy and mass concentration at each node $x_j$ are updated based on the values from the previous time step, considering heat and mass transfer, and phase change dynamics (Alexiades & Solomon, 1993). By solving the equations explicitly, this method provides a straightforward and efficient numerical solution, accurately capturing the phase change behavior within the material.

In Figure 2.5, the lightest blue represents ice, while the darkest blue denotes the deicing solution. The mushy region is depicted using a medium blue shade. The location of the melting front—a sharp interface between the solid and liquid phases—is marked by a red line in the figure. This melting front indicates the boundary where the phase change occurs. We considered a sharp interface so the enthalpy scheme should yield a single mushy node at each time step. The mushy region corresponds to the computational cell that contains this melting front, indicating a mix of solid ice and liquid deicing solution.

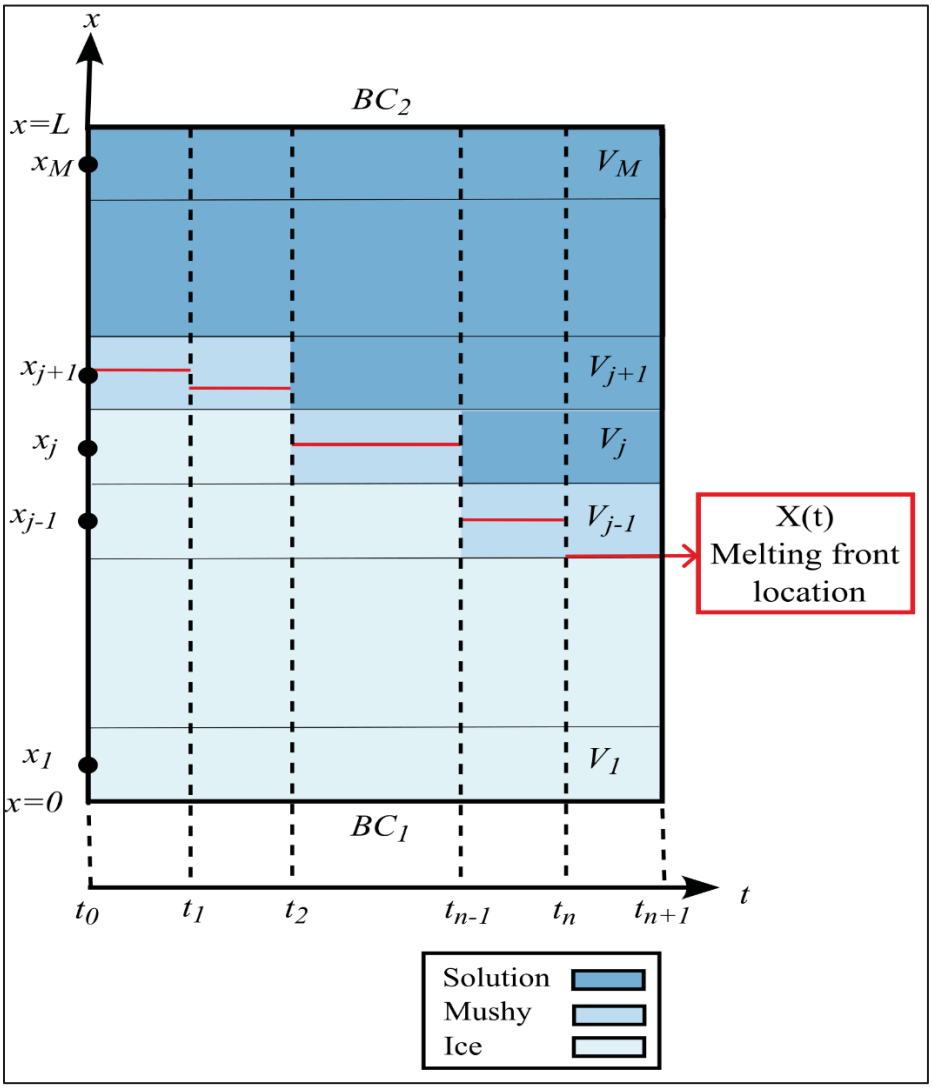


Figure 2.5 Space-time grid for melting

In the discretization scheme, the mushy region is treated as a special computational cell that contains both phases. This cell retains its designation as a mushy region until all the ice within it has completely melted. Once the ice in this cell is fully melted, the melting front advances to the adjacent cell, continuing the phase transition process. The red line representing the melting front thus serves as a dynamic boundary that moves through the computational grid, delineating the transition from solid ice to liquid deicing solution.

This melting front is computed based on the enthalpy of each cell, making it an output of the numerical method rather than an input. The exact location of the melting front is determined based on the enthalpy distribution, assuming a model where liquid is on top and solid is on the bottom, but the enthalpy method itself only needs to track whether a cell is in a solid, liquid, or mushy state.

The discrete equations used in the numerical method differ slightly at the initial time step, $n = 0$. At this initial time step, the temperatures $T_j^0$and the initial front location $X^0$ are imposed. These initial conditions set the stage for the simulation, providing the necessary starting points for the temperature distribution and the position of the melting front. The equations for the subsequent time steps are then applied to advance the simulation, updating the temperatures and the position of the melting front as the phase change progresses.
The density should be defined for each control volume based on the concentration of the solute. The liquid (solution) concentration that we considered is the mass concentration and is calculated by

$$C_l = C = \frac{m_1}{m} \tag{2.26}$$

where $m_1$ is the mass of solute, and $m$ is the total mass of the solution. Furthermore, for the volume concentration, we have

$$C_{volume} = \frac{V_1}{V}, \qquad \frac{V_2}{V} = 1 - C_{volume} \tag{2.27}$$

where $V_1$ is the volume of solute, $V_2$ is the volume of solvent, and $V$ is the total volume of the solution. Also, we know $m_1 = \rho_1 V_1$ and $m = \rho V$. So, the relationship between the mass concentration and volume concentration is

$$C = \frac{\rho_1}{\rho} c_{volume} \tag{2.28}$$

Moreover, based on the fact that in the solution, the total mass concentration of solute and solvent is equal to 1, we have:

$$\frac{m_1}{m} + \frac{m_2}{m} = 1 \tag{2.29}$$

where $m_2$ is the mass of the solvent. From equations (2.26) to (2.29), for the volume concentration of solute, we get:

$$C_{volume} = \frac{\rho - \rho_2}{\rho_1 - \rho_2} \tag{2.30}$$

where $\rho_1$ is the density of the solute (deicer), $\rho_2$ is the density of the solvent (water), and $\rho$ is the density of the solution.

Now, by considering equations (2.26), (2.28), and (2.29), we can calculate the density of the solution $\rho$ with:

$$\rho = \frac{\rho_1 \rho_2}{\rho_1 + C(\rho_2 - \rho_1)} \tag{2.31}$$

For each control volume, if the control volume is totally solid (ice) the density is $\rho_2$. If it is totally liquid (solution) the density is calculated based on equation (2.31). If the control volume is the mushy cell, the density will be calculated considering liquid fraction:

$$\rho_j^0 = \begin{cases} \dfrac{\rho_1 \rho_2}{\rho_1 + C_l(\rho_2 - \rho_1)}, & \lambda_j^0 = 1 \\ \lambda_j^0 \left( \dfrac{\rho_1 \rho_2}{\rho_1 + C_l(\rho_2 - \rho_1)} \right) + \left(1 - \lambda_j^0\right)(\rho_2), & 0 < \lambda_j^0 < 1 \\ \rho_2 & \lambda_j^0 = 0 \end{cases} \tag{2.32}$$

Furthermore, $\lambda_j^0$ represents the initial liquid fraction. For the node $x_j$, the boundaries of the control volume are positioned at $(j-1)\Delta x$ and $j\Delta x$. The control volume is considered to be in the mushy zone if $j\Delta x < X^0 \leq (j-1)\Delta x$. Thus, the initial liquid fraction is given by:

$$\lambda_j^0 = \begin{cases} 1, & j\Delta x \leq X^0 \quad (liquid) \\ \dfrac{(X^0 - (j-1)\Delta x)}{\Delta x}, & j\Delta x < X^0 \leq (j-1)\Delta x \ (mushy) \\ 0, & (j-1)\Delta x > X^0 \quad (solid) \end{cases} \tag{2.33}$$

The initial temperature is set for both the liquid and solid regions. For the mushy region, it is calculated based on the initial liquid fraction as follows:

$$T_j^0 = \begin{cases} T_l, & j\Delta x \leq X^0 \quad (liquid) \\ \lambda_j^0 T_l + \left(1-\lambda_j^0\right)T_s, & j\Delta x < X^0 \leq (j-1)\Delta x \ (mushy) \\ T_s, & (j-1)\Delta x > X^0 \quad (solid) \end{cases} \tag{2.34}$$

Similarly, the initial solute mass concentration is imposed for both the liquid and solid regions. In the mushy region, the solute mass concentration is determined based on the initial liquid fraction.

$$C_j^0 = \begin{cases} C_l, & j\Delta x \leq X^0 \quad (liquid) \\ \lambda_j^0 C_l + \left(1-\lambda_j^0\right)C_s, & j\Delta x < X^0 \leq (j-1) \ (mushy) \\ C_s = 0, & (j-1)\Delta x > X^0 \quad (solid) \end{cases} \tag{2.35}$$

The local enthalpy in the solid phase, $E_{solid}$, and in the liquid phase, $E_{liquid}$, should be defined with respect to a constant reference temperature, which in this case is the melting temperature of the pure material (water), $T_{mpure}$. So, to calculate the local enthalpy at initial time we have:

$$E_j^0 = \begin{cases} \rho_j^0 L + \rho_j^0 c_{p-l}\left[T_j^0 - T_{mpure}\right], & \lambda_j^0 = 1 \\ \lambda_j^0\left(\rho_j^0\left(c_{p-l}\left[T_j^0 - T_{mpure}\right] + L_f\right)\right) + \cdots \\ +\left(1-\lambda_j^0\right)\left(\rho_1 c_{p-s}\left[T_j^0 - T_{mpure}\right]\right), & 0 < \lambda_j^0 < 1 \\ \rho_1 c_{p-s}\left[T_j^0 - T_{mpure}\right], & \lambda_j^0 = 0 \end{cases} \tag{2.36}$$

with the local enthalpy in the solid phase $E_{solid} = \rho c_{p-s}\left[T_j^0 - T_{mpure}\right]$, and in the liquid phase $E_{liquid} = \rho(c_{p-l}\left[T_j^0 - T_{mpure}\right] + L)$. In Figure 2.6, we show the liquid fraction ($\lambda$) on the enthalpy-temperature relationship graph.

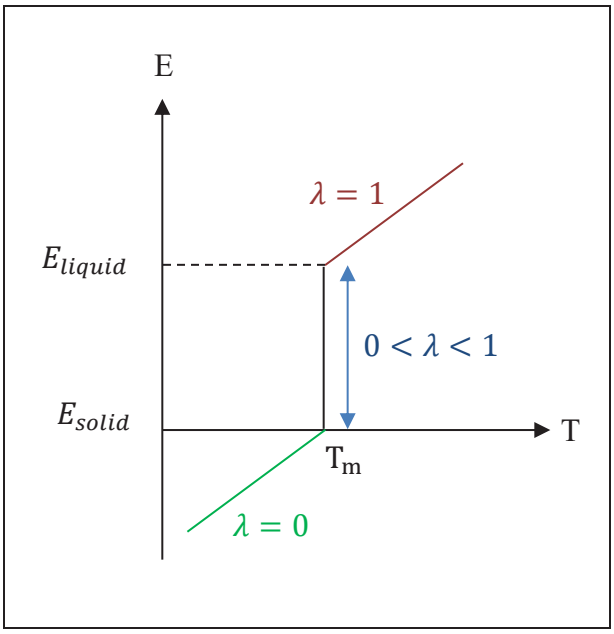


Figure 2.6 Liquid fraction on E_T relationship

The conductivity of a mushy control volume is influenced by the structure of the phase-change front. When considering a distinct interface between two regions, a control volume with a sharp front includes layers of solid and liquid arranged in series. The effective conductivity of this arrangement is the sum of the conductivities of these layers. The thickness of each layer is determined by the fractions of solid and liquid, leading to the following relationship:

$$\frac{1}{k_j^n} = \frac{\lambda_j^n}{k_L} + \frac{1 - \lambda_j^n}{k_s} \tag{2.37}$$

Based on this equation, if the control volume is entirely liquid ($\lambda_j^n = 1$), then the thermal conductivity is equal to the thermal conductivity of the liquid. Conversely, if the control volume is entirely solid ($\lambda_j^n = 0$), the thermal conductivity is equal to the thermal conductivity of the solid.

The diffusion coefficient is calculated in manner similar as the thermal conductivity coefficient, resulting in:

$$\frac{1}{D_j^n} = \frac{\lambda_j^n}{D_L} + \frac{1-\lambda_j^n}{D_s} \tag{2.38}$$

The heat resistance of the layers for $j = 2, \dots, M$ is given by:

$$R_{j-1/2} = \frac{\Delta x}{2}\left(\frac{1}{k_{j-1}} + \frac{1}{k_j}\right) \tag{2.39}$$

The heat fluxes across the common boundary of the control volumes, for $j = 2, \dots, M$, are determined by dividing the total temperature drop by the sum of the resistances of the layers:

$$q_{j-1/2}^n = -\frac{T_j^n - T_{j-1}^n}{R_{j-1/2}} \tag{2.40}$$

Similarly, the mass resistances and fluxes follow the same principle as heat resistances and fluxes. Therefore, for $j = 2, \dots, M$ we have:

$$J_{j-1/2}^n = -\frac{C_j^n - C_{j-1}^n}{R2_{j-1/2}} \quad with \quad R2_{j-1/2} = \frac{\Delta x}{2}\left(\frac{1}{D_{j-1}} + \frac{1}{D_j}\right) \tag{2.41}$$

The boundary conditions at x=0 (BC1), equation 2.8 become:

$$T_1^n = T_p \tag{2.42}$$

and the boundary conditions at x=L (BC2), equation 2.9 become:

$$q_{M+1/2}^n = -\frac{T_M^n - T_\infty^n}{\frac{1}{h_{cd}} + R_{M+1/2}} \tag{2.43}$$

$$with \text{ resistance } R_{M+1/2} = \frac{\Delta x}{2}\left(\frac{1}{k_l}\right)$$

We don't have any mass flux at boundaries, the boundary conditions for concentration at x=0 and x=L is

$$J^n_{1/2} = 0 \tag{2.44}$$

$$J^n_{M+1/2} = 0$$

The fluxes have been evaluated at the time $t_n$. At this time ($t_n$), the enthalpy $E_j^n$ determine the thermal state of the control volume $V_j$ completely. The enthalpy must then be explicitly calculated for the next time step $t_{n+1}$ based on the material's state at $t_n$. By discretizing the energy conservation law, for $j = 1, \dots, M$, we obtain:

$$E_j^{n+1} = E_j^n + \frac{\Delta t}{\Delta x}\left[q^n_{j-1/2} - q^n_{j+1/2}\right] \tag{2.45}$$

Additionally, the concentration in each control volume should be updated for the next time step $t_{n+1}$ explicitly, based on the mass transfer between the control volumes caused by concentration differences at $t_n$. Using the discretized Fick's law equations for mass concentration, for $j = 1, \dots, M$, we have:

$$C_j^{n+1} = C_j^n + \frac{\Delta t}{\Delta x}\left[J^n_{j-1/2} - J^n_{j+1/2}\right] \tag{2.46}$$

After calculating the enthalpy and concentration for the time step $t_{n+1}$, the computation proceeds to the next time step $t_{n+1}$.

For the new time step $t_n$, the calculated enthalpy ($E_j^{n+1}$) and concentration ($C_j^{n+1}$), become the enthalpy ($E_j^n$) and concentration ($C_j^n$) for each control volume. The state of the material is then determined based on these updated enthalpies and local enthalpies for each control volume.

For mixtures (solutions), local enthalpies are calculated at the melting temperature $T_{mj}$ by:

For solid:

$$E_{solid} = \rho_j c_s\left(T_{m\,j} - T_{mpure}\right) \tag{2.47}$$

For liquid:

$$E_{liquid} = \rho_j\left(c_l\left(T_{m\,j} - T_{mpure}\right) + L_f\right) \tag{2.48}$$

For each control volume, the melting point is updated at each time step based on local concentration, as described in Equation 2.25.

For pure water, melting temperature is equal to the melting temperature of pure material $T_{m\,j} = T_{mpure}$, the local enthalpies are:

$$E_{solid} = 0 \qquad (2.49)$$
$$E_{liquid} = \rho L_f$$

If the enthalpy is below the $E_{solid}$, the material is entirely in the solid phase with a liquid fraction of zero. If the enthalpy exceeds $E_{liquid}$, the material is fully liquid with a liquid fraction of one. When the enthalpy falls between $E_{solid}$ and $E_{liquid}$, the material is in a mushy node, and the liquid fraction must be calculated. The liquid fraction for these three regions is defined as follows:

$$\lambda_j^n = \begin{cases} 0 & E_j^n \le E_{solid} \quad (solid) \\ \dfrac{E_j^n - E_{solid}}{E_{liquid} - E_{solid}} & E_{solid} < E_j^n < E_{liquid} \quad (mushy) \\ 1, & E_j^n \ge E_{liquid} \quad (liquid) \end{cases} \qquad (2.50)$$

Next step the density in each control volume should be updated:

$$\rho_j = \begin{cases} \dfrac{\rho_1 \rho_2}{\rho_1 + C_j^n(\rho_2 - \rho_1)}, & \lambda_j^0 = 1 \\ \lambda_j^0 \left( \dfrac{\rho_1 \rho_2}{\rho_1 + C_j^n(\rho_2 - \rho_1)} \right) + \left(1 - \lambda_j^0\right)(\rho_1), & 0 < \lambda_j^0 < 1 \\ \rho_1 & \lambda_j^0 = 0 \end{cases} \qquad (2.51)$$

Then, the temperature in each control volume can be updated based on the liquid fraction as follows:

$$T_j^n = \begin{cases} T_{m\,j} + \dfrac{E_j^n}{\rho_j c_{p-s}}, & \lambda_j^n \le 0 \quad (solid) \\ T_{m\,j}, & 0 < \lambda_j^n < 1 \quad (mushy) \\ T_{m\,j} + \dfrac{E_j^n - \rho_j L_f}{\rho_j c_{p-l}}, & \lambda_j^n \ge 1 \quad (liquid) \end{cases} \tag{2.52}$$

At each time step ($t_n$), the location of the melting front should be updated based on liquid fraction. If the mushy node is the M-th node, we have:

$$X^n = x_{M-\frac{1}{2}} + \lambda_M^n \Delta x_M \tag{2.53}$$

Two stability criteria are established for the time increment $\Delta t$: one for the thermal equation and another for the concentration equation:

1. $\Delta t_T = \Delta x^2/4 \max(\alpha)$ (Thermal stability condition) (Alexiades & Solomon, 1993)
2. $\Delta t_c = \Delta x^2/4 \max(D)$ (Concentration stability condition)

The minimum of these two conditions is regarded as the stability condition (min ($\Delta t_T, \Delta t_c$)). The thermal diffusivity in solid and liquid are $\alpha_s = k_s/\rho c_{p-s}$, $\alpha_l = k_l/\rho c_{p-l}$, respectively.

The MATLAB code implements the explicit finite volume scheme using equations (2.45) and (2.46). It solves the system for temperature, concentration, melting temperature, and the location of the melting front. The calculation algorithm for the MATLAB code is in appendix1.

In order to better illustrate the advancements and improvements introduced by the runway deicing model (RDM), a comparison between RDM and previous pavement deicing models is presented. This comparison highlights key differences in the approach, methodology, and assumptions underlying each model, providing a clearer understanding of how RDM addresses the gaps and limitations identified in existing studies.

The key differences between RDM and the previous model for the pavement deicing are highlighted in table 2.1.

Table 2.1 Key differences between RDM model and previous pavement deicing models

| Aspect | RDM model | Previous models |
|---|---|---|
| Melting rate | Numerically calculated using heat and mass flux dynamics | Derived from experimental data (volume changes) |
| Melting front | Dynamically tracked using liquid fraction and enthalpy method | Not explicitly tracked |
| Diffusion effects | Explicitly modeled (mass flux from concentration gradients) | Ignored |
| Melting temperature | Dynamically updated based on local conditions (concentration, enthalpy), and freezing point diagram | Calculated from concentration (based on experimental data for mass) using freezing point diagram |
| Temperature | Numerically calculated using enthalpy-temperature relation | Assumes uniform temperature in the solid and liquid phases |
| Spatial solution | 1D spatially resolved (finite volumes) | Assumes uniformity (bulk measurements) |
| Phase identification | Determined from enthalpy and liquid fraction | Not explicitly addressed |
| Update mechanism | Fully coupled heat-mass transfer calculations at each time step | Based on experimental observations |

The comparison presented in Table 2.1 clearly illustrates the significant advancements offered by the RDM model over previous pavement deicing models. Notably, the RDM model incorporates dynamic melting rate calculations, tracks the melting front, and explicitly models the diffusion effects of deicer chemicals, all of which were either oversimplified or neglected in earlier models. Additionally, the RDM model accounts for and continuously updated melting temperatures and variations in melting temperature based on local conditions. The RDM model integrates heat-mass transfer at each time step, and uses a spatially resolved

approach, providing a more accurate representation of the deicing process. These enhancements address key limitations in the modeling of runway deicing and offer a more realistic framework for predicting deicing behavior in complex, real-world scenarios.

## 2.4 Analytical solution (Neumann similarity solution)

For the first verification, we used the Neumann similarity solution as the analytical solution. $\lambda_{Neumann}$ is the solution to the transcendental equation which is calculated based on the Stefan condition ($St$) and velocity ($v$):

$$\frac{St_L}{exp(\lambda^2)\, erf\ (\lambda)} - \frac{St_s}{\beta\, exp(\,\beta^2\lambda^2)\, erfc(\beta\,\lambda)} = \lambda_{Neumann}\sqrt{\pi} \tag{2.54}$$

where the Stefan condition in liquid phase ($St_L$) and solid phase ($St_s$), along with the Dimensionless number ($\beta$), are defined as follows:

$$St_L = \frac{c_L(T_L - T_m)}{L_f}\,, \quad St_s = \frac{c_s(T_m - T_s)}{L_f}\,, \quad \beta = \sqrt{\frac{\alpha_L}{\alpha_s}} \tag{2.55}$$

Here, $T_m$ is the melting temperature, $T_L$ is liquid temperature, and $T_s$ is the solid temperature.

The temperatures can then be calculated by:

$$T(x,t) = T_\infty - \Delta T_L \frac{erf\left(\frac{x}{2\sqrt{\alpha t}}\right)}{erf(\lambda_{Neumann}\,)} \tag{2.56}$$

We use dimensionless variables to simplify the analysis:

$$\xi = \frac{x}{\hat{x}} \quad , \qquad F_0 = \frac{\alpha_L t}{\hat{x}^2} \quad and\ \Sigma(F_0) = \frac{X(t)}{\hat{x}} \tag{2.57}$$

So, the dimensionless melting front location is defined by:

$$\Sigma(F_0) = 2\lambda\sqrt{F_0} \tag{2.58}$$

and the dimensionless temperature is given by:

$$u(\xi, F_0) = \frac{T(x,t) - T_m}{\Delta T_L} \tag{2.59}$$

## 2.5 Conclusion

This chapter defined the runway deicing problem and presented the governing equations of the models used in this thesis. The two-phase Stefan problem was described, taking into account mass diffusion and non-constant melting temperature due to impurities in one of the phases. The calculation of melting temperature based on solute concentration was explained. The numerical methods employed in this thesis were then detailed. The enthalpy method was implemented to address the problem. The finite volume method was used for discretization. The model solved the enthalpy and concentration explicitly. Finally, the Neumann similarity solution was presented for the classical two-phase Stefan problem, incorporating dimensionless variables to streamline the analysis and establish a reliable analytical benchmark for verifying the numerical results.

# CHAPITRE 3

## Results

In the previous chapter, we presented the methodology used to develop the Runway Deicing Model. This model applies mathematical equations for a two-phase Stefan problem combined with Fick's law for impure materials. The numerical approach includes the enthalpy method and a finite volume discretization. This chapter presents the numerical results of the Runway Deicing Model. The first objective is to verify key model outputs, including temperature, melting front location, concentration, mass of ice melted, enthalpy, and melting temperature. The second objective is to validate specific results—temperature, mass of ice melted, and concentration—against four experimental tests conducted at the AMIL laboratory. These tests were performed for two runway deicing products, Potassium Formate (KFO) and Potassium Acetate (KAC), under two conditions with temperatures of -2°C and -10°C. The third objective is to identify critical parameters, such as the heat convection coefficient, initial deicing solution thickness, and melting temperature, that influence the model's accuracy. Finally, we assess the Runway Deicing model's performance under runway conditions. We focus on model output parameters, such as surface temperature of the deicing solution, mass of ice melted, melting front position, concentration of the deicing solution, and melting rate. We study the effects of input parameters such as deicer reapplication frequency under runway conditions. The runway conditions are test size, radiation heat flux, and the temperature imposed by the runway pavement.

The verification section starts with a comparison of the model prediction with the Neumann similarity solution results of ice melting, without chemical solution, as presented in the book written by Alexiades and Solomon (1993). It serves as the foundational model for two-phase problems using the Stefan problem for pure materials. For the second step of the verification, we analyzed the key parameters for the deicing process such as the temperature, the melting front location, the concentration, the mass of ice melted, the enthalpy and the melting

temperature. Then we investigate how different mesh sizes affect the runway model's outcomes.

In the validation section, the results for temperature, mass of ice melted, and the solution concentration over a 30-minute period are validated against the experimental data for temperature and mass of ice melted.

In the parametric study section, we explore the effect of the critical parameters on the runway model. These parameters include the heat convection coefficient, which depends on the wind velocity, the initial thickness of the deicing solution in the system, and the melting temperature.

The runway condition section of this chapter focuses on the results of the Runway Deicing Model (RDM) such as the surface temperature of the deicing solution, mass of ice melted, melting front position, concentration of the deicing solution. It examines the effects of the condition of the runway including test size, radiation heat flux, and the temperature imposed by the runway pavement. We will compare the melting rate of two deicing chemicals for two temperature conditions. To close the section, we investigate the effect of the deicer reapplication frequency on the melting rates.
In all sections, the Runway Deicing Model (RDM) is referred to as the Runway Model.

**Experimental Test (Test Case for Verification and Validation)**

Ice melting experiments reduce the number of parameters and control environmental conditions (Charpentier et al., 2023). For simplicity in the experimental test, factors such as wind velocity, radiation, and temperature of the runway pavement are not considered. The parameters controlled during the process are the ambient temperature $T_{\infty}$, and the area ($A$). To develop the RDM, the runway deicing problem simplifies to the ice melting experiments done by Charpentier et al. (2022), illustrated in Figure 3.1.

The experimental test followed the AS6170 test method standard (Committee, 2021) for the ice melting test. The deicing solution, also called Runway Deicing Product (RDP), is poured on an ice surface in a Petri dish. The brine (melted ice and the deicing solution) is removed at a fixed time interval and the weight is measured. The test is conducted in a cold room at the International Laboratory of Anti-icing Materials (AMIL) (Charpentier et al., 2023). This cold room provides controlled air temperatures between 0 °C and −35 °C, with a precision of 0.5 °C. The tests were conducted at a controlled temperature of -2 °C and -10 °C. A Petri dish with a diameter of 150 mm was used. Each Petri dish contained ice with a thickness of 3.4 mm, corresponding to sixty milliliters of water.

In Figure 3.1 part (a), 5 grams of the deicing solution at -2˚C and -10 ˚C is evenly applied onto the ice surface. The concentration of the solution is 50% (w/w). In part (b), you can observe partial melting of the ice. In part (c), after 5 minutes, the dish was tilted, and the brine is removed using a compressed air gun for a duration of 10 seconds, with a margin of error of ±1 second, while the dish remained inside the cold chamber at the specified test temperature. Once the brine is cleared, the Petri dish is weighed with a precision of ±0.01 g at room temperature, and the value is read from the scale precisely 20 seconds later.

With the initial masses of the Petri dish and ice sheet, $m_s$, and the final masses of the petri dish and remaining ice, $m_e$, the amount of ice melted, $m_{im}$, is calculated by equation 3.1:

$$m_{im} = m_s - m_e \tag{3.1}$$

The identical procedure is replicated, utilizing a new ice sheet, at time intervals of 10 and 30 minutes, and the outcomes are documented. Also, to increase the accuracy, additional measurements were made every minute before 5 minutes.

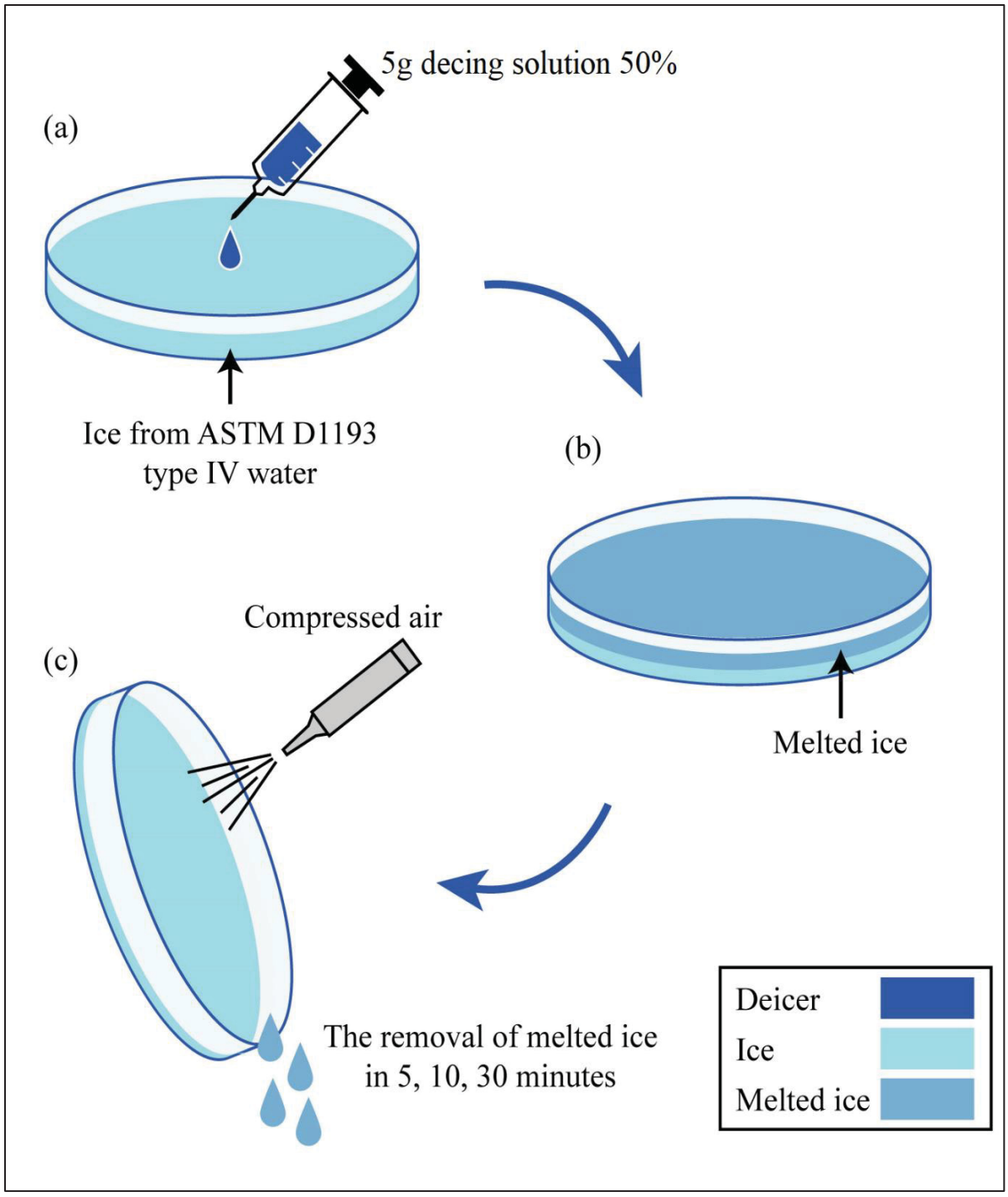


Figure 3.1 Ice melt methodology based on AS6170 (Committee, 2021)
(a) 5 g deicing solution 50% is poured on ice sample
(b) Ice is melted after deicer added (c) The melted ice is removed by compressed air

Thus, in the test case based on experiments, given that the ice thickness (0.0034 m) is relatively small compared to the diameter (0.3 m) of the petri dish (with a ratio of 0.01), the influence of the cylinder wall is disregarded. At the bottom boundary, the heat flux between the Petri dish and the ice is negligible. At the deicing solution surface, the convective heat flux is caused by natural convection and the heat loss by radiation is neglected.

For verification, Potassium Formate (KFO) is used as a deicer. In the validation section, in addition to KFO, the results for Potassium Acetate (KAC) will also be validated. Table 3.1, lists the properties used in this study, sourced from Melinder's work (Melinder, 2007). For KAC, the eutectic temperature and concentration are based on experimental results.

Table 3.1 Properties of KAC, KFO, ice

| Parameters / Material | $c_p$ $\frac{J}{kg℃}$ | $k$ $\frac{W}{mK}$ | $\rho$ $\frac{kg}{m^3}$ | $T_e$ ℃ | $C_e$ % | Molar mass $\frac{kg}{mol}$ |
|---|---|---|---|---|---|---|
| KAC | 2766 | 0.43 | 1290 | -60 | 50% | 0.098 |
| KFO | 2655 | 0.47 | 1355 | -52 | 49% | 0.084 |
| Ice | 2045 | 2.30 | 1000 | | | |

## 3.1 Model Verification

### 3.1.1 The Neumann Similarity Solution

The Neumann similarity solution is selected to verify the model interface location and temperature predictions without the presence of a deicer. Initially, dimensionless parameters and the Neumann similarity solution are used to solve the two-phase Stefan problem. This involves a slab with $0 < x < 1$, initially solid at $T_s = -1$ . The melting temperature remains constant because it is pure ice. To avoid boundary condition effects, because in the Neumann similarity solution the slab is semi-infinite, the simulation runs until the interface reaches the midpoint of the slab, the half melt time of 1.8 as per the test case definition (Alexiades & Solomon, 1993).

Inputs for the test case are dimensionless values:

- $T_m = 0$ , $T_l = 1$ , $T_s = -1$
- $\rho_l = \rho_s = c_l = c_s = k_l = k_s = 1$

The imposed temperature is $T_\infty = 1$. These values are chosen to align with the dimensionless formulation, where all thermophysical parameters equal one, resulting in $\alpha_s = \alpha_l = \frac{k_s}{\rho_s c_s} = \frac{k_l}{\rho_l c_l} = 1$. The simulation uses the Stefan number $St = 0.1$, so the latent heat $L_f = \frac{1}{St} = 10$, with $M = 200$ nodes. The stability condition, based on the Alexiades and Solomon (1993), requires $\Delta t \leq \frac{\Delta x^2}{3} \max(\alpha_s, \alpha_l)$. To prevent stability issues, we selected a factor $1/4$, slightly smaller than $1/3$, leading to a time step of $\Delta t = \frac{\Delta x^2}{4} \max(\alpha_s, \alpha_l)$. The melting front location and the temperature are calculated by equations 2.58 and 2.59, respectively.

The results for the interface location over a time span of 1.8 are shown in Figure 3.2. The vertical axis represents the position of the melting front, while the horizontal axis indicates time. As previously mentioned, the simulation continues until the interface reaches the midpoint of the slab. The results align well with the expected outcome until the melting process reaches halfway. At the end of the simulation, the analytical position is 0.5, while the RDM

predicts 0.57. This slight discrepancy arises because the analytical solution assumes a semi-infinite domain, whereas the numerical method uses a finite slab $0 < x < 1$.

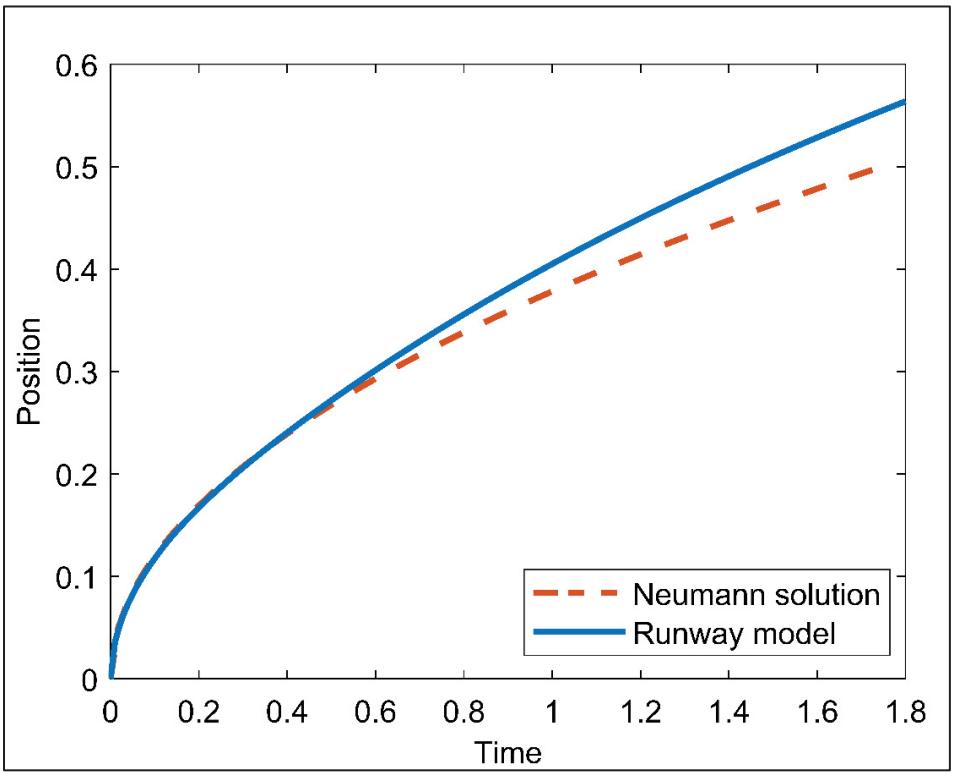


Figure 3.2 Melting front location as a function of time, for a time span 1.8

Figure 3.3 illustrates the temperature profile from $x = 0$ to the midpoint of the slab. The dashed line and the solid represent the exact solution (Neumann's solution) and numerical results at $x = 0, 0.1, 0.2, 0.3,$ and $0.4$. In this figure, the vertical axis indicates temperature ranging from -1 (solid state) to 1 (liquid state), while the horizontal axis represents time. The figure shows that at positions near the boundary (x= 0.1, 0.2), the temperature rapidly increases due to the imposed temperature ($T = 1$), reaching the melting temperature ($T_m = 0$). As a result, melting begins, the material transitions to a liquid state, and the temperature continues to rise. The temperature discrepancies increase with time and x position.

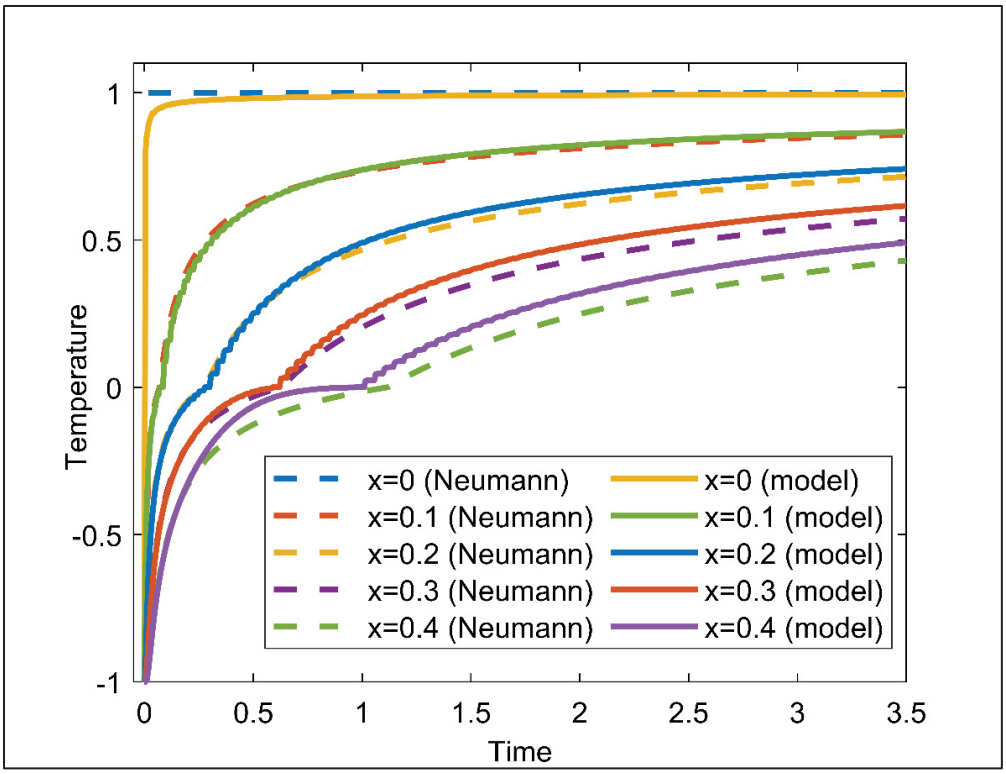


Figure 3.3 Temperature profile until half of the slab in time 3.5

This evidence supports the hypothesis that boundary conditions impact the solution, particularly the difference between a semi-infinite assumption and the finite domain used in the model. In the Neumann solution, the temperature at the melting front increases more slowly because the semi-infinite domain assumes a larger mass of ice, which allows for more latent heat absorption. This greater latent heat capacity leads to a smaller temperature increase as heat is conducted toward the larger mass of ice. Unlike a finite domain, where the available latent heat is limited, the semi-infinite assumption distributes energy over a larger mass, resulting in a lower temperature rise at the melting front.

To verify the semi-infinite assumption and further address discrepancies, two methods were tested. First, we extended the computational domain in the numerical model, and second, we imposed a small heat flux at the bottom leaving the computational domain at the bottom, with a temperature equal to -1, matching the ice temperature.

- **Extended Domain**:

  In the first approach, we increased the computational domain length to 5. Figures 3.4a and 3.4b show the results for the melting front location and temperature distribution up to x = 0.4 over a final time of 3.5. In this case, both the runway model and Neumann solution align well, demonstrating a close match for the melting front location and the temperature profile within the system.

- **Imposed Heat Flux**:

  In the second approach, a small heat flux was applied at the bottom to maintain a colder temperature there. Figures 3.5a and 3.5b illustrate the melting front location and temperature distribution for x = 0.4 over a final time of 3.5. Here, a slight discrepancy appears once the melting front passes the midpoint of the slab. At the final time, the Neumann solution predicts a melting front position of 0.7, while the runway model predicts 0.67. This discrepancy occurs because the imposed heat flux at the bottom maintains a temperature slightly lower than in the Neumann solution, as evidenced in Figure 3.5b, where the temperature remains lower after time 1.8.

a.

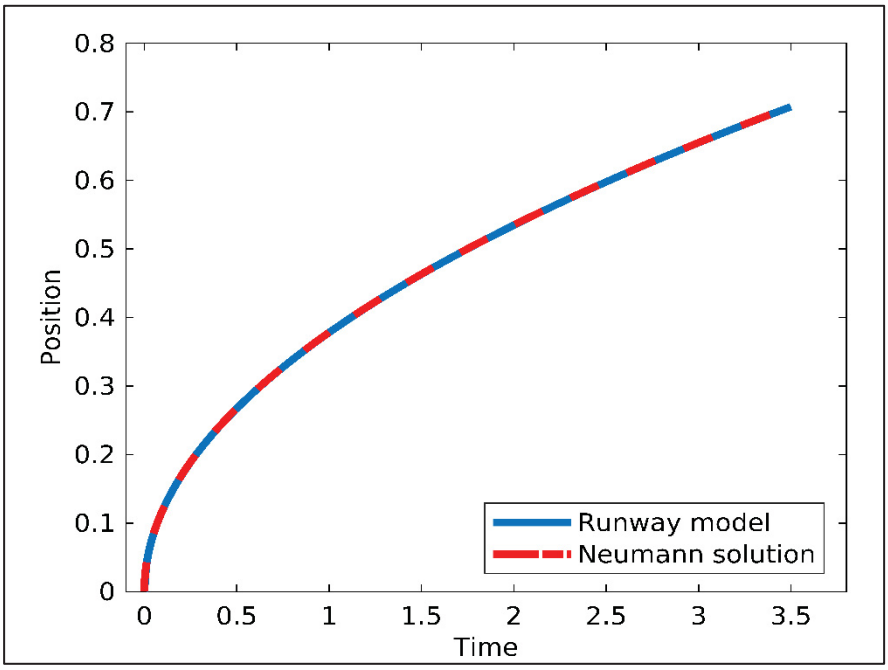


b.

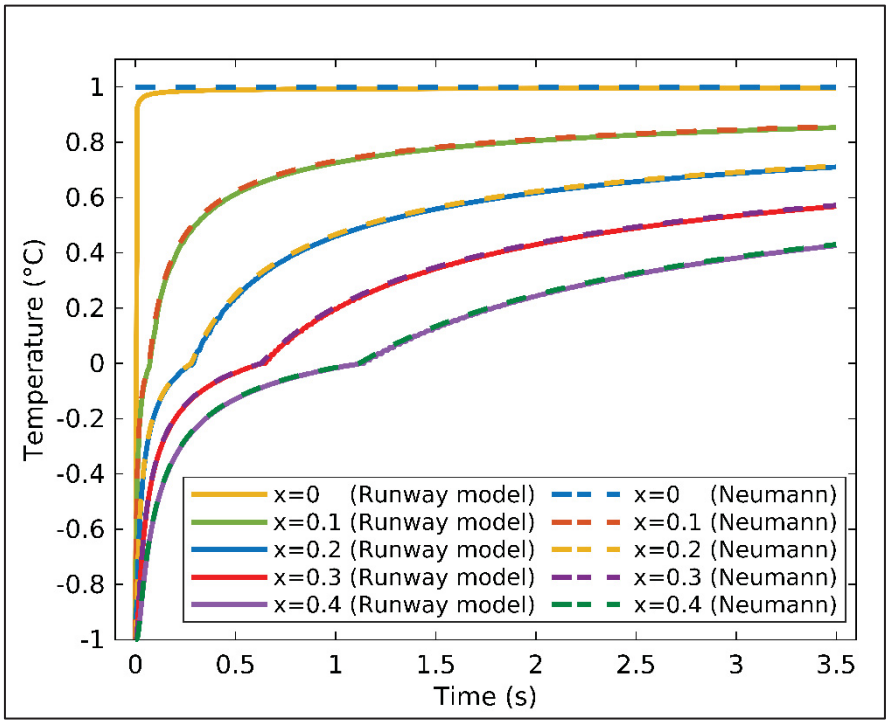


Figure 3.4 (a) Melting front location in time 3.5
(b) Temperature profile until half of the slab as a function of time 3.5

a.

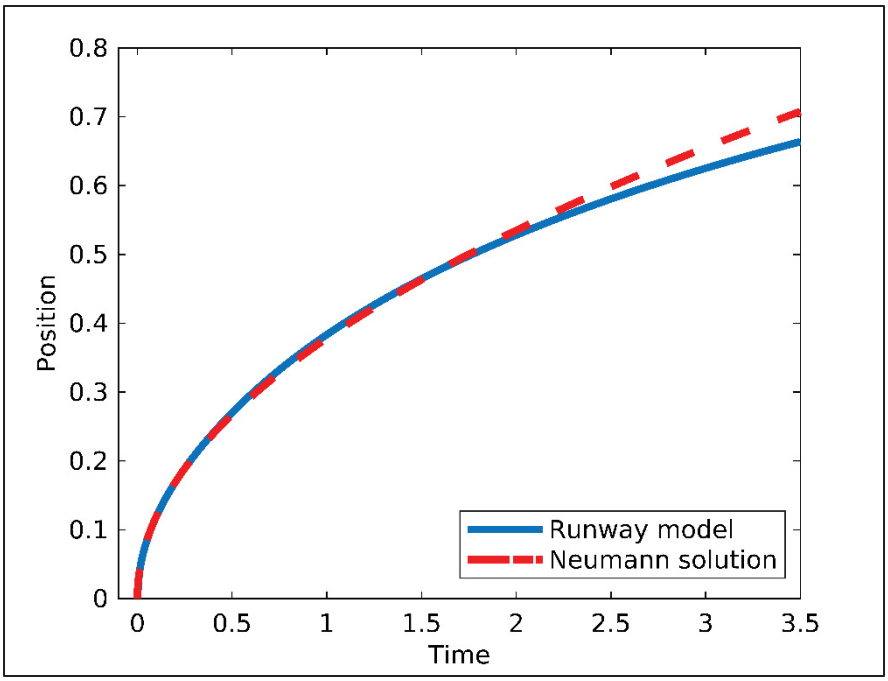


b.

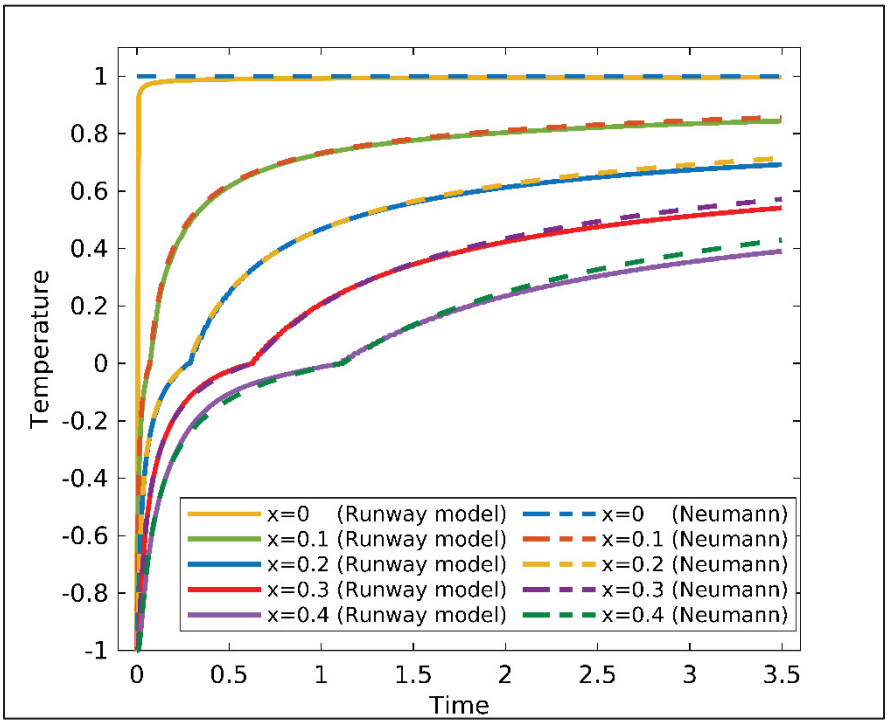


Figure 3.5 (a) Melting front location in time 3.5
(b) Temperature profile until half of the slab as a function of time 3.5

After verification of the model without presence of the deicer in system, now we need to verify the model with presence of the deicer by analyzing the key parameters of the model, such as the temperature, the interface location, the concentration, the mass of melted ice, the enthalpy and the melting temperature.

### 3.1.2 Analyze the Key Parameters

In the deicing process, the presence of chemicals lowers the freezing point of the solution, allowing melting to continue if this point is below the temperature of the system. This endothermic process requires heat from the environment. If heat does not flow quickly enough to the melting front, the temperature drops. The ice-solution interface must be colder than the surroundings to allow the heat flow. This effect is demonstrated by measuring the surface temperature of the melting ice with the deicer. As melting progresses, meltwater dilutes the deicing solution, raising the freezing point. Thus, the system's temperature decreases while the freezing point increases, slowing the melting reaction until it stops when the system reaches the deicing solution's freezing point. The system reaches an equilibrium temperature. Heat flow into the system slows down the rate of temperature drop and eventually warms the system, enabling melting even with a dilute concentration of deicer.

To verify the model, we analyzed key parameters. First, we examined the relationship between the surface temperature and the melting temperature to confirm the initial rapid temperature drop, followed by a rise in the melting temperature. Furthermore, we tracked the location of the melting front to observe the ongoing melting process until the system reached thermal equilibrium, indicating a faster rate of ice melting. Moreover, we monitored the concentration of the deicing solution, noting its gradual decrease over time due to dilution from melted ice. Additionally, we studied the mass of ice melted, showing that the highest melting rate occurred up to the equilibrium temperature, after which ice melted more slowly.

To further investigate the concentration changes within the system, we present concentration data for specific control volumes associated with discretized nodes. We examine the

relationship between concentration and melting temperature of a specific control volume, confirming that it follows the liquidus curve, as discussed in the methodology chapter.

Next, we analyzed the enthalpy (internal energy) in a control volume, confirming that during melting, the internal energy increased rapidly, corresponding to the latent heat ($L_f$) at that melting temperature. Finally, we compared the enthalpy results for two control volumes—one initially liquid and the other initially solid—to highlight the differences in enthalpy.

As explained in the methodology chapter, the liquid fraction is calculated based on enthalpy. Using the liquid fraction, we determined the location of the melting front, and consequently, the mass of ice melted. Additionally, Fick's law was applied to calculate the solute concentration in the solution and to model the penetration of solute into the ice, enabling the melting process. The melting temperature was then updated based on this concentration.

To verify that the mass transfer terms are correctly incorporated into the enthalpy method, we calculated the mass of water and solute in each control volume, using concentrations derived from Fick's law. We also calculate the solute concentration based on the interface location within each control volume. The results for both the mass of ice melted and the solute concentration are presented using both calculation approaches.

These findings align with those obtained using KFO for the experimental test case and confirm that our model correctly simulates the deicing process. The initial values based on the experimental test case are presented in table 3.2. Based on equation 2.24, the diffusion coefficients are $0.8 \times 10^{-9}\ m^2/s$ for KFO at -2°C. Based on equation 2.20, with 5 g of deicer in the solution at 50% concentration, $H_{initial}$ for KFO is $2.058 \times 10^{-4}$ m. The domain length is equal to the thickness of the ice plus the height of the solution, and it is equal to $3.6058 \times 10^{-3}\ m$ and $\Delta x = 3.6058 \times 10^{-6}\ m$. The heat convection coefficient based on equation 2.12 is equal to $9.6\ W\ m^{-2}K^{-1}$, considering a wind velocity of $1\ m\ s^{-1}$. The number of nodes (M) is 1000. The time step is $(\Delta t) = 2.89 \times 10^{-6}$ min with the final time 30 minutes.

Table 3.2 Initial values of the test case

| Parameters | Values |
|---|---|
| Latent heat ($J\ kg^{-1}$) | 334000 |
| Initial concentration (%) | 50 |
| Ice thickness (m) | 0.0034 |
| Initial mass of deicer (g) | 5 |
| Air temperature (℃) | -2 |
| Ice temperature (℃) | |
| Solution temperature (℃) | |

Figure 3.6 shows how the temperature changes versus melting temperature in the surface control volume (M=1000) as a function of time. The solid line is the surface temperature, and the dashed line represents the melting temperature at the surface.

From the starting point to around 2.5 minutes, there is a sharp decline in surface temperature, while the melting temperature increases rapidly due to the initial drop in solution concentration. The melting point temperature of the solution is influenced by its concentration, with higher concentrations resulting in lower melting point temperatures. Initially the concentration is high, so the melting point is low at around -52 ℃, and we have a high melting rate. As ice melts, it absorbs latent energy, causing the surface temperature to decrease. However, the ice melts due to the diffusion of deicer, which increases its concentration within the ice, lowering the melting point and causing the ice to melt as its temperature remains higher than the reduced melting point of the solution. As melting progresses, the solution becomes more diluted, leading to an increase in the melting point temperature over time. After 2.5minutes, the surface temperature reaches almost the melting temperature. The system reaches an equilibrium temperature. Subsequently, the temperature begins to rise as energy is absorbed from the ambient air, because the ambient temperature, constant at -2 °C, is higher than the temperature of the ice surface.

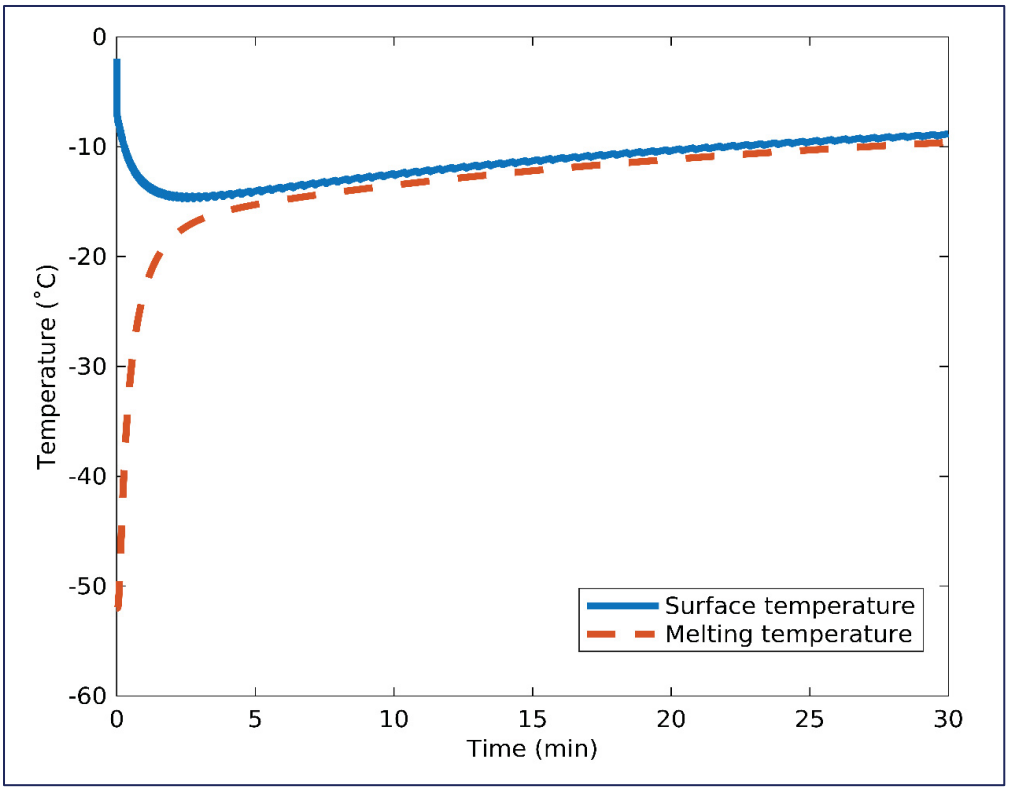


Figure 3.6 Surface temperature vs melting temperature
as a function of time over 30 minutes

The melting front location and the concentration of the solution as a function of time are shown in figure 3.7 and figure 3.8, respectively. Initially the ice thickness is $3.4 \times 10^{-3}\ m$, and the solution concentration is 50%. Until $t = 2.5$ minutes, the melting front location moves rapidly, reducing the ice thickness to $3.14 \times 10^{-4}\ m$ due to a high deicer concentration in the solution. During this period, $2.6 \times 10^{-4}\ m$ (thick) of ice is melted, diluting the solution and lowering its concentration to 21.96%. From $t = 2.5$ minutes to 30 minutes, the ice melts more slowly (at the rate of $0.82 \times 10^{-4}\ m\ min^{-1}$) as the solution becomes more diluted. By the end, $4.86 \times 10^{-4}\ m$ (thick) of ice is melted, and the concentration decreases to 14.86 %. As the ice continues to melt, the concentration decreases, and the melting front keeps moving toward the ice bottom. After an infinite amount of time, if all the ice melts, the concentration will be 0.038%, which is calculated based on the mass of the melted ice and its addition to the solution.

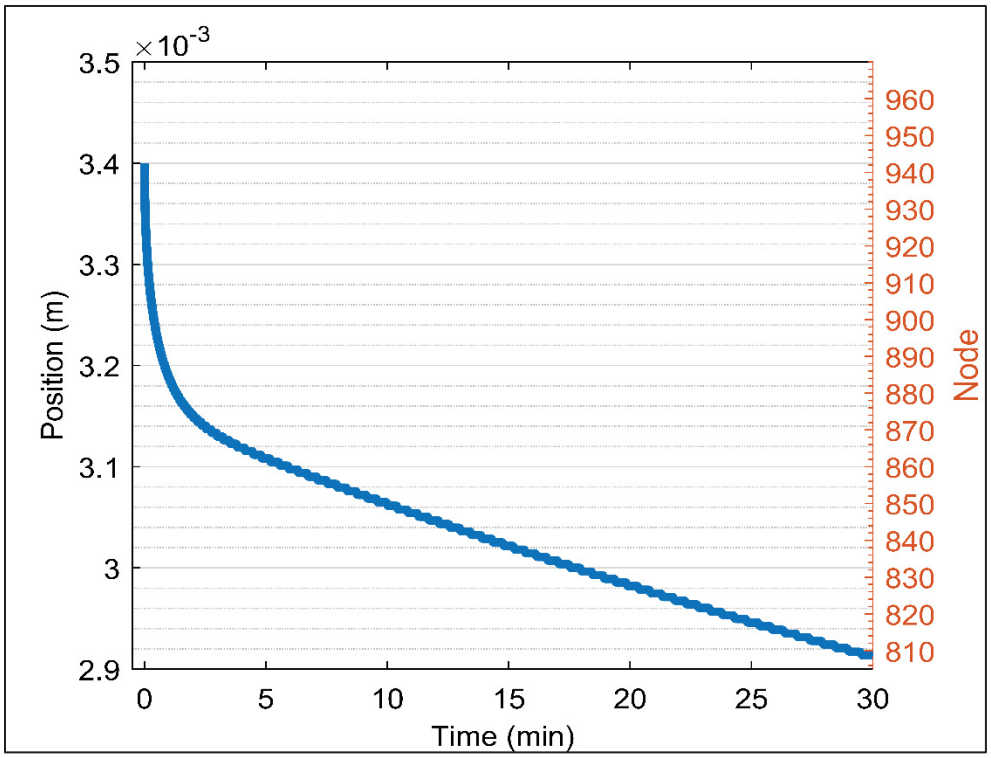


Figure 3.7 Interface location as a function of time over 30 minutes

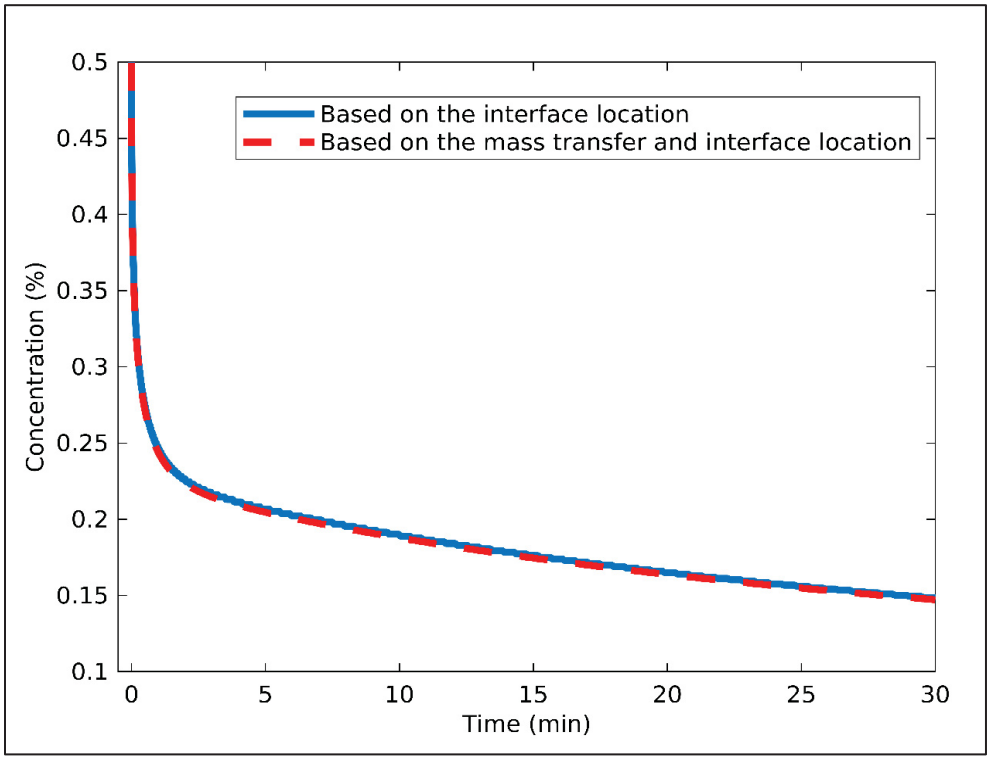


Figure 3.8 Concentration of the system as a function of time in 30 minutes

In figure 3.8 two different concentration results are presented. The solid blue line represents the concentration calculated based on the interface location and the initial mass of solute in the solution. The dashed orange line corresponds to the concentration determined using Fick's law, also considering the interface location.

Figure 3.9 illustrates the results for the mass of ice melted over 30 minutes. The dashed orange line corresponds to the mass of ice melted determined using Fick's law, also considering the interface location (based on liquid fraction). In each control volume, the mass of water is calculated from the solution concentration. At each time step, the water masses from all control volumes are summed to obtain the total mass of water in the system. The total mass of water, subtracted from the initial mass of water, gives the mass of ice melted. The solid blue line represents the mass of ice melted calculated based on the interface location.

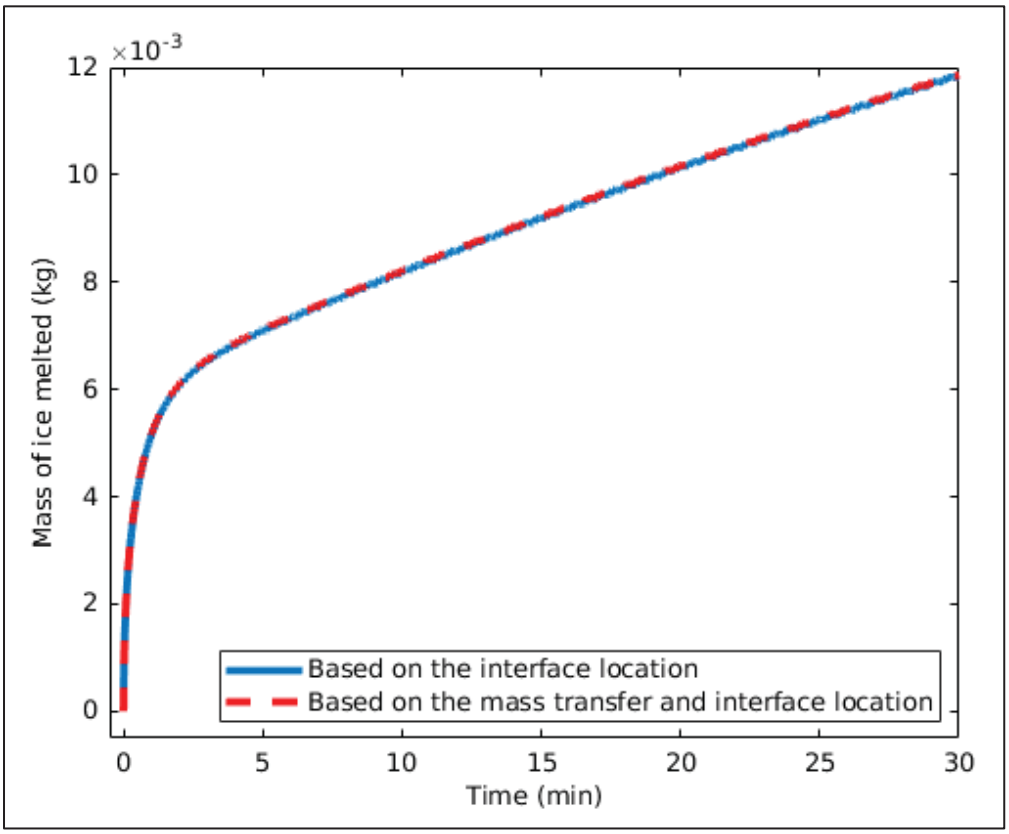


Figure 3.9 Mass of ice melted as a function of time in 30 minutes

As demonstrated in Figures 3.8 and 3.9, the results obtained from both methods—the one based on the interface location and the one using Fick's law—are in complete agreement. This consistency confirms that the mass transfer process has been correctly implemented within the enthalpy method. The accurate calculation of the mass of ice melted and the concentration of solute in both approaches indicates that the coupling between the heat transfer and mass transfer processes has been successfully modeled, ensuring the reliability of the simulation.

To further verify this approach, Figure 3.10 shows the concentration results obtained from both methods across five control volumes. The figure illustrates the deicer concentration at five positions along the x-axis as a function of time. The solid lines represent the concentration results in the control volumes based on Fick's law, while the dashed orange lines show the concentration calculated using Fick's law, considering the interface location (based on liquid fraction) and the mass of solute in each control volume, is calculated from the solution concentration and liquid fraction.

The graph presents concentrations from location x= $\frac{1}{1000}$ (node j=1) to x= $\frac{1000}{1000}$ (node j=1000), where $j = 1$ the bottom of the ice, and j=1000 the solution surface. Initially, the solution contains 50% deicer, while the ice is pure. The initial location of the liquid-solid interface is at node $\frac{943}{1000}$, where at the beginning the concentration is 3.4%. Nodes j=850 (x= $\frac{850}{1000}$) is located in pure ice at the beginning. Node j=808 (x= $\frac{808}{1000}$) marks the last control volume where the melting front is located at 30 minutes. As the deicer penetrates the ice, the concentration increases. However, once the ice begins to melt, the concentration in those cells decreases, as the melted ice dilutes the solution. This occurs because the increase in liquid volume reduces the overall deicer concentration, leading to some diffusion of the deicer back into the liquid phase.

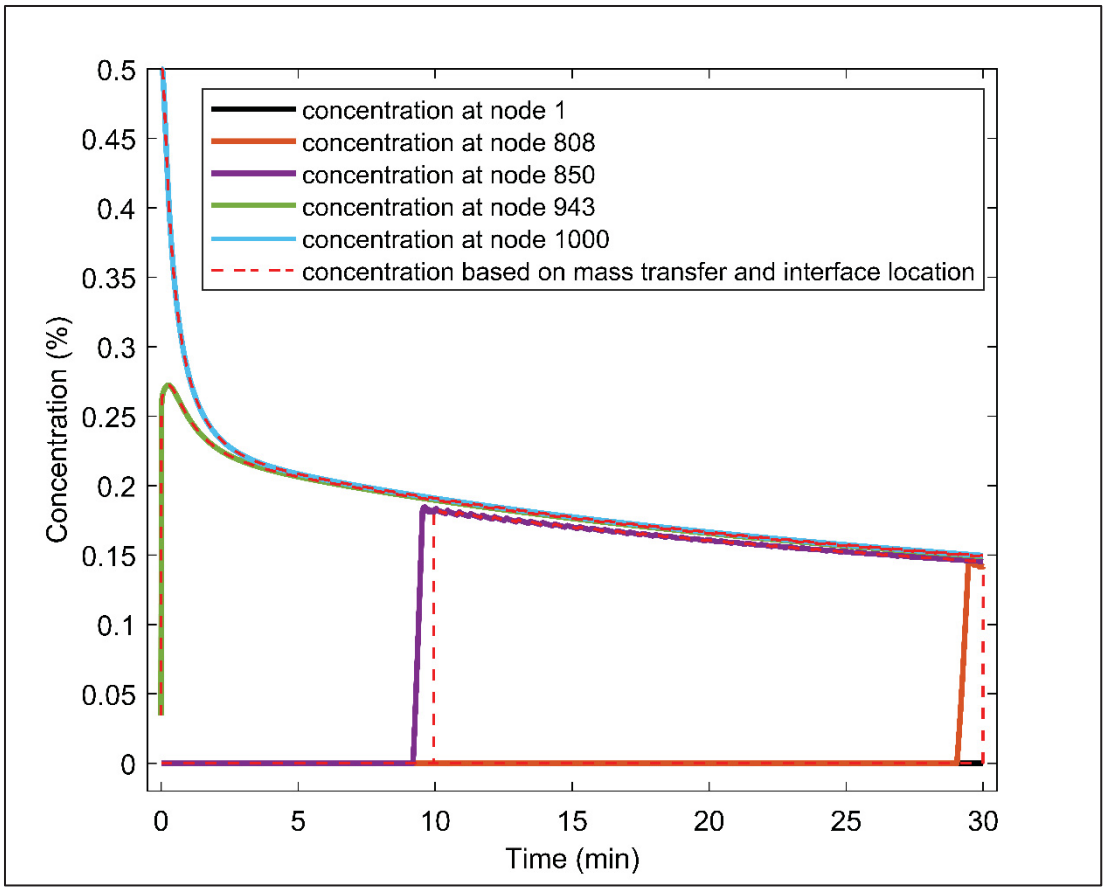


Figure 3.10 Concentration in five control volumes
as a function of time for 30 minutes

As it is shown in figure 3.10 the concentration results from the two calculation methods for nodes j=850 (x= $\frac{850}{1000}$) and j=808 (x= $\frac{808}{1000}$) are not the same. This discrepancy arises due to the penetration of the deicer. In the model, when the melting front is located exactly between two control volumes—one fully liquid and the other fully solid—the deicer penetrates the ice control volume. However, the liquid fraction in that volume does not change until the internal energy increases sufficiently, causing the liquid fraction to exceed zero, signaling a phase change from ice to liquid. As a result, the result based on Fick's law shows an earlier increase in concentration in these control volumes compared to the method that accounts for liquid fraction.

However, when considering the concentration of the entire system, as previously illustrated in Figure 3.8, both methods yield the same result. This is because the total mass of solute in the system remains constant.

In Figure 3.11, the melting temperature is shown as a function of concentration at node j=1000, which is the deicing solution at the initial time. Due to the thin thickness of the deicing solution, the temperature remains nearly uniform throughout the solution. Initially, the solute concentration in this control volume is 50% with eutectic melting temperature -52°C. As the concentration decreases, the melting temperature rises. By the end, with a solute concentration of 15%, the melting temperature increases to around -10°C. This confirms that the concentration-melting temperature relationship follows the liquidus curve for the solution mixture.

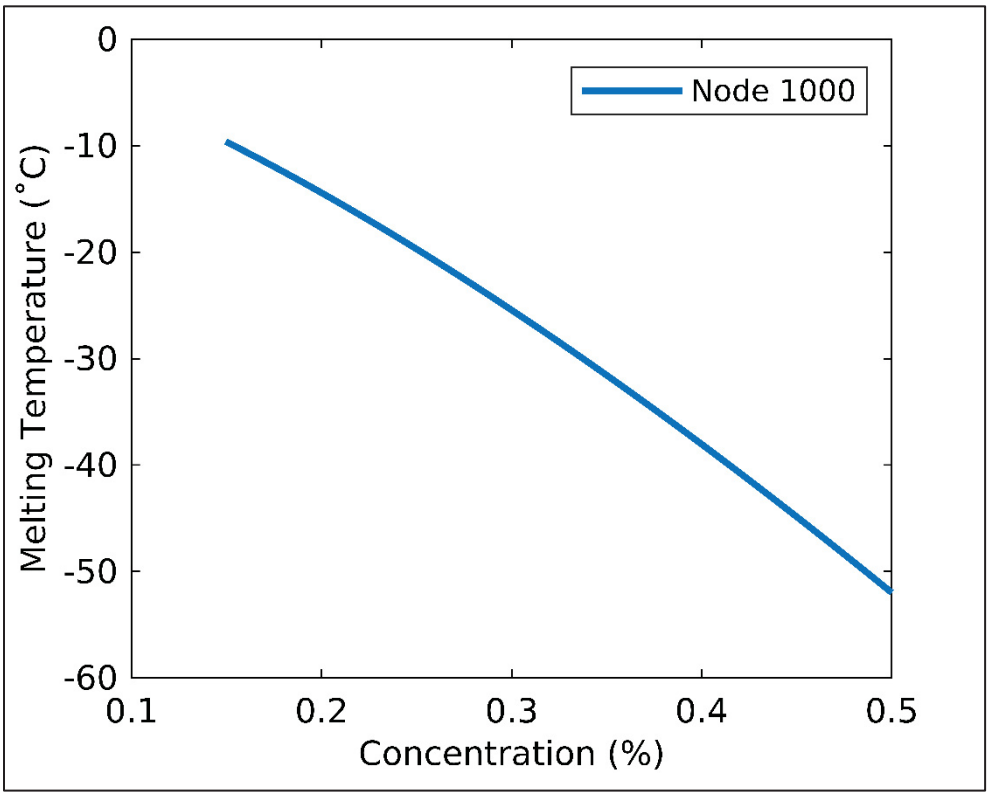


Figure 3.11 Melting temperature vs concentration for node j=1000 as a function of time in 30 minutes

Figure 3.12 shows the results for enthalpy multiplied by density and melting temperature as a function of time for node j=850. The solid blue line represents the enthalpy, while the dashed orange line corresponds to the melting temperature over a 30-minute period. Initially, the control volume at j=850 is in the solid (ice) region. As seen in the figure, the melting temperature remains at 0°C for the first 10 minutes, as it is pure ice. During this time, the internal energy is below 0 $Jm^{-3}$, indicating the solid state.

At t = 10 minutes, the internal energy begins to rise due to the phase change and latent heat absorption. At this point, as the phase shifts to liquid, the volume becomes a solution containing deicer. As a result, the melting temperature drops to -13°C, corresponding to a solution concentration of 18% (shown in figure 3.10). Between 10 and 30 minutes, the melting temperature gradually increases due to dilution, while the enthalpy increases slightly, reflecting heat exchange since the system is not insulated.

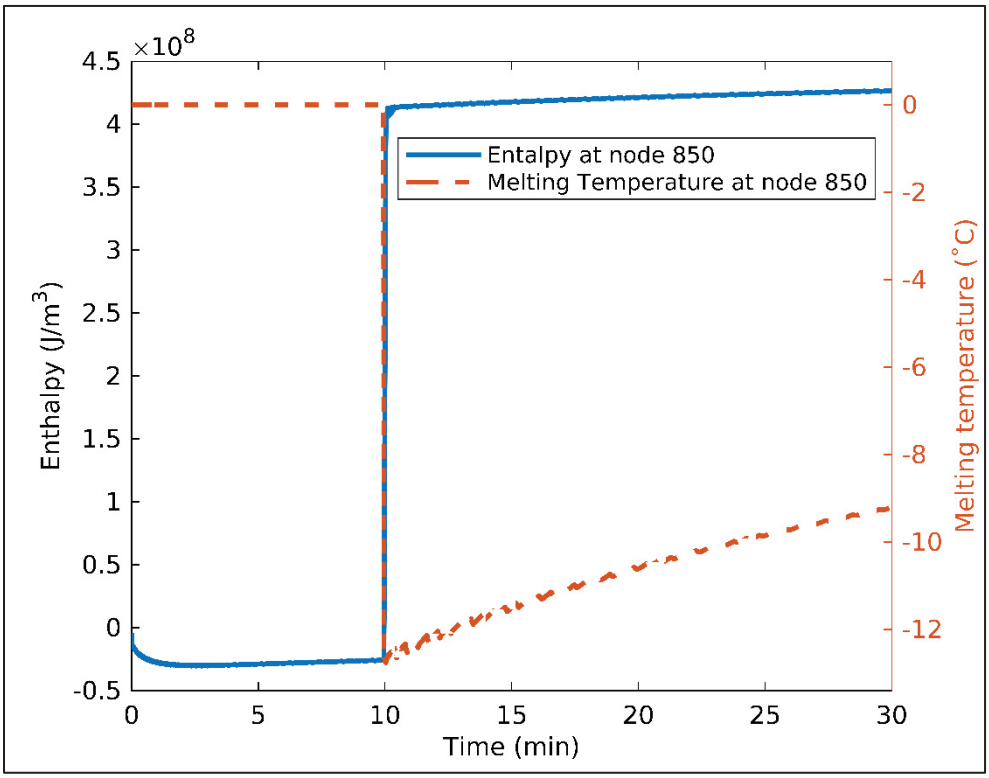


Figure 3.12 Enthalpy and melting temperature for node j=850 as a function of time in 30 minutes

Figure 3.13 illustrates the changes in enthalpy over time for three specific control volumes. The dashed black line represents a control volume that is initially liquid and remains liquid throughout the entire process. The solid blue line shows the enthalpy of a control volume that is initially solid but undergoes a phase change to liquid at t = 10 minutes. The orange dashed line corresponds to a control volume that starts as solid and remains solid until the end of the simulation.

At the beginning of the process, as seen in all control volumes, the internal energy decreases. This is due to the presence of the deicing solution, which initially absorbs heat from the surroundings to melt the ice. The deicer initiates the melting process by lowering the freezing point of the ice, which can cause an initial energy deficit in the system as latent heat is absorbed for phase change. This cooling effect reduces the internal energy of the system until enough heat is transferred to overcome the melting process and increase the system's temperature. For the control volume that does not undergo a phase change, the enthalpy increases slightly due to heat exchange, as the system is not insulated on the deicing solution-air side (BC2). In contrast, for the control volume at node j=850, there is a sharp increase in internal energy, which is attributed to the phase change. This phenomenon was analyzed in detail with the melting temperature in Figure 3.12.

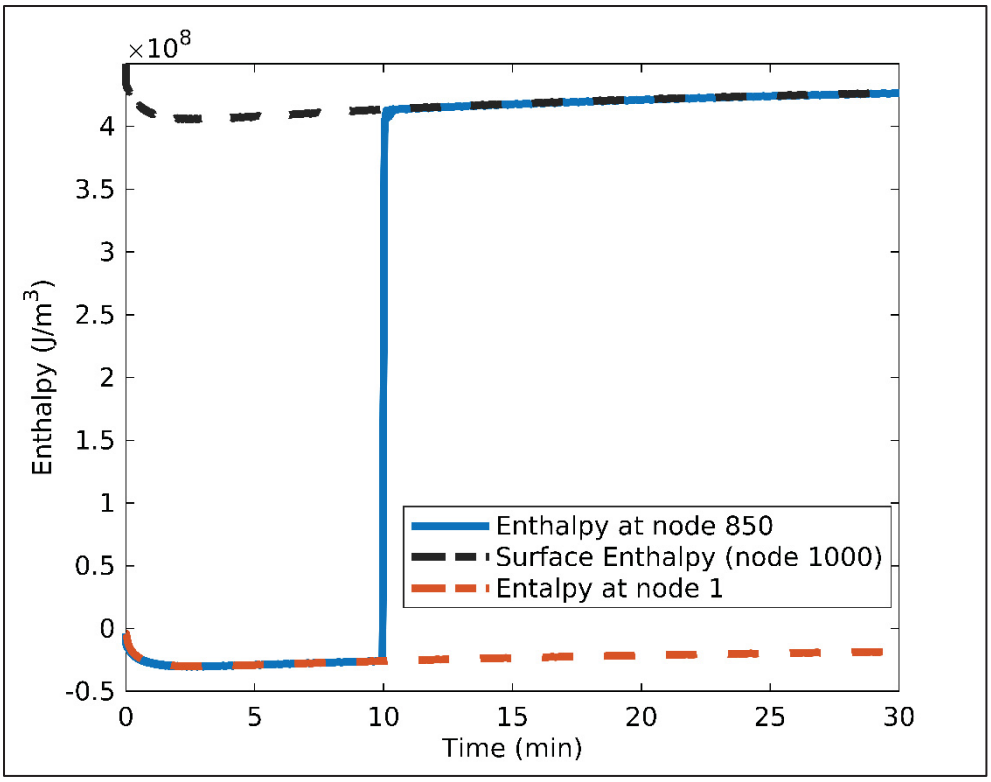


Figure 3.13 Enthalpy in three control volumes as a function of time, in 30 minutes

In conclusion, the model has been successfully verified through multiple approaches. Without the presence of deicing solution, the model was validated against the analytical Neumann similarity solution, confirming its accuracy in predicting temperature and melting front location during the phase change. With deicing chemicals present, the key parameters of the model—such as surface temperature, melting front location, deicer concentration, and mass of ice melted—were thoroughly analyzed. The results consistently aligned with expected physical behavior, including the temperature-concentration relationship following the liquidus curve and the correct incorporation of mass transfer terms using Fick's law. The model accurately captures the dynamic interaction between heat flow, concentration changes, and melting, demonstrating its reliability for simulating the deicing process. These findings indicate that the model behaves as expected and can be considered verified for the intended application.

### 3.1.3 Mesh Study

The purpose of this section is to determine the results' sensitivity to the mesh. As observed here and in the literature, the enthalpy method generates solutions with staircases in the temperature evolution (Alexiades & Solomon, 1993; Gudibande & Iyer, 2013; Tarwidi, 2019). These staircases disappear with a reduction of the control volume size. Thus, the smoothness of the curves for the temperature and the melting front location are investigated. The KFO values from Tables 3.1 and 3.2 are used. The computational values used in mesh study are:

- Initial Diffusion coefficient (D) = $0.8 \times 10^{-9}\ m^2/s$
- Heat convection coefficient ($h_c$)= 9.6 $W/m^2K$
- Initial deicing solution thickness ($H_{initial}$) = $2.06 \times 10^{-4}\ (m)$
- The Length ($L$)= $3.606 \times 10^{-3}(m)$
- Number of nodes ($M$)= $250, 500$ and $1000$.

Figure 3.14 and figure 3.15 present the surface temperature and mass of ice melted over time for three meshes consisting of 250, 500, and 1000 nodes, respectively. The temperature and mass of ice melted predicted by the model are not strongly dependent on mesh size. For instance, the final surface temperature varies by less than 0.1°C between the 250-node and 1000-node meshes, and the total mass of ice melted differs by less than 0.1g. The final temperature and total mass transfer between the 500-node and 1000-node meshes are almost zero. This indicates that the model's results are stable across mesh sizes. As observed, with a finer mesh (i.e., a higher number of nodes), the stair-like behavior in the results becomes less pronounced, leading to smoother and the difference between two meshes results is reduced when you increase the number of nodes.

The staircase phenomenon arises because, if the interface exists within a specific control volume, the temperature of that volume is maintained at $T_m$ . Consequently, the temperature in the remaining portion of the system gradually settles into a stable state aligned with a fixed isotherm passing through that volume. When the interface transitions to the subsequent control volume, temperatures swiftly readjust before settling into a new equilibrium. Consequently,

the duration of each staircase is directly tied to the duration of the interface spends within each control volume, resulting in the staircase phenomenon.

Thus, the duration of each staircase is closely linked to the time the interface remains within each control volume. To quantitatively assess this phenomenon, we analyze the duration of the staircase for various mesh sizes over a period of approximately 5 minutes. For M=250, the staircase duration spans from 4.09 to 5.54 minutes, totaling 1.45 minutes. For M=500, the duration ranges from 4.80 to 5.54 minutes, totaling 0.74 minutes. Lastly, for M=1000, the duration ranges from 4.84 to 5.20 minutes, totaling 0.36 minutes. These results indicate that the time required for each staircase diminishes with increasing meshes, demonstrating a proportional relationship between mesh refinement and the duration of the staircase phenomenon.

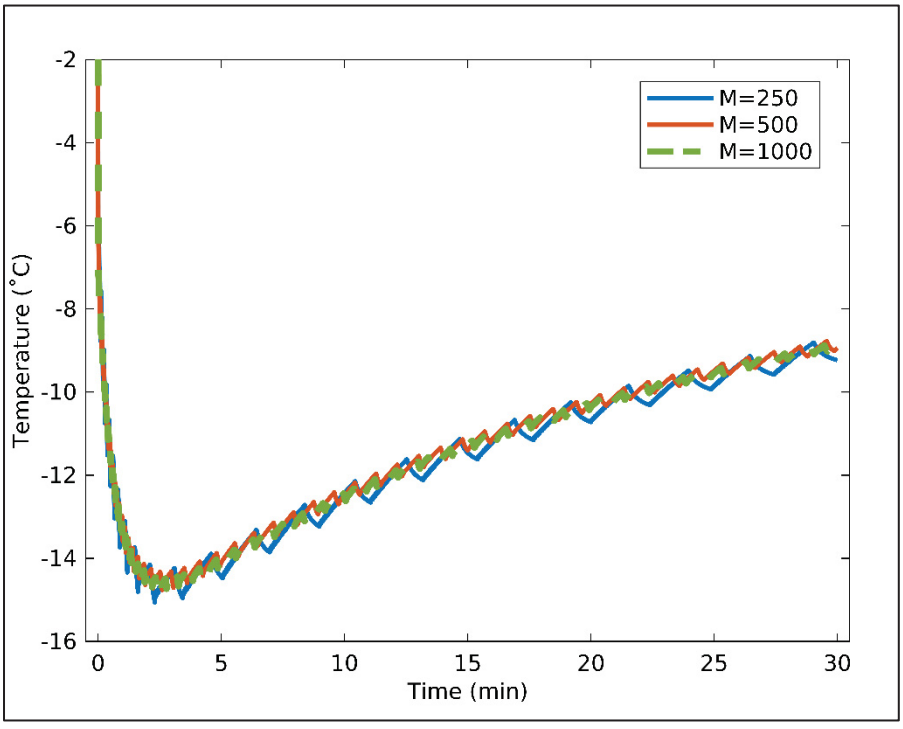


Figure 3.14 Surface temperature as a function of time
with 250, 500, and 1000 nodes after 30 min

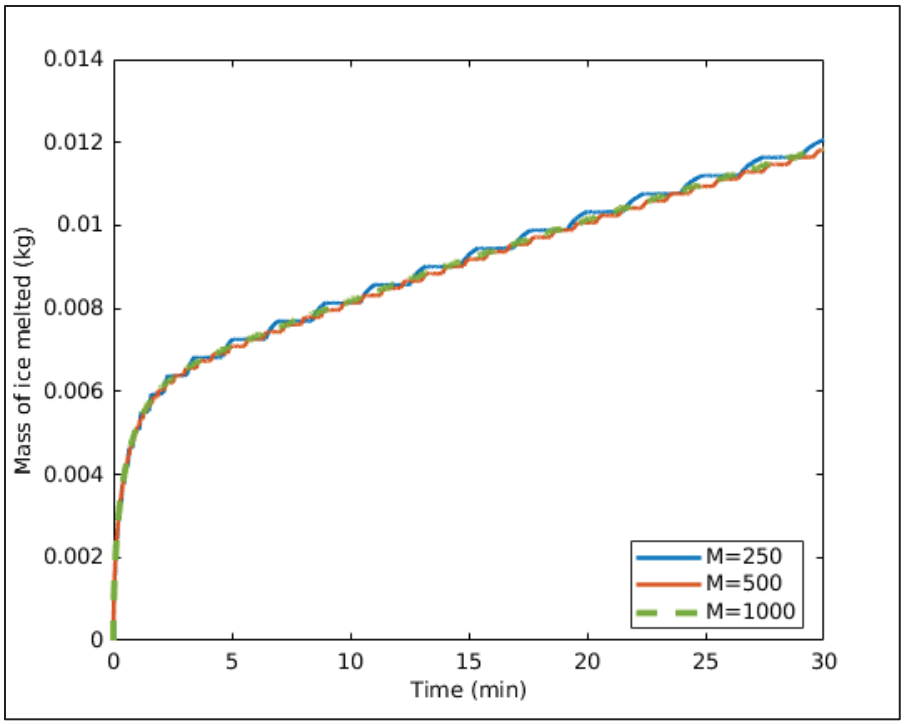


Figure 3.15 Melting front location as a function of time
with 250, 500, and 1000 nodes after 30 min.

Beyond reducing the staircase effect, the overall model predictions for temperature and mass of melted ice remain consistent between M=500 and M=1000, suggesting that M=500 provides reasonable accuracy. However, M=1000 was selected for the validation section to ensure sufficient accuracy and mitigate the staircase effect, considering that calculations take around 24 hours on the computer with the CPU model 12$^{th}$ Gen Intel(R) Core (TM) i9-12900, which does not impose a high time cost for the simulation.

## 3.2 Model Validation

To validate the model, we use a test case based on the experimental tests described in detail in Section 3.1. The validation is performed for two runway deicing products (RDPs), Potassium Formate (KFO) and Potassium Acetate (KAC), with their properties listed in Table 3.1. For each RDP, two temperature conditions are considered: Condition 1 at -2°C and Condition 2 at -10°C.

The validation results for surface temperature, mass of ice melted, and concentration are presented for both products, starting with Condition 1 (-2°C) followed by Condition 2 (-10°C). All initial values used in the validation are provided in Table 3.2, except temperatures that we have 2 conditions.

The detail for the computational domain for KFO and KAC are presented in table 3.3

Table 3.3 Computationnel values

| Parameter | KFO | KAC |
|---|---|---|
| $H_{initial}\ (m)$ | $2.06 \times 10^{-4}$ | $2.31 \times 10^{-4}$ |
| Length $(m)$ | $3.606 \times 10^{-3}$ | $3.631 \times 10^{-3}$ |
| $\Delta x\ (m)$ | $3.60 \times 10^{-6}$ | $3.63 \times 10^{-6}$ |
| $\Delta t\ (min)$ | $2.89 \times 10^{-6}$ | $2.93 \times 10^{-6}$ |
| M (number of nodes) | 1000 | |

### 3.2.1 Condition1

Based on equation 2.24, the diffusion coefficients are $0.5 \times 10^{-9}\ m^2/s$ and $0.8 \times 10^{-9}\ m^2/s$ for KAC and KFO, respectively. Based on equation 2.12, the heat convection coefficient is 9.6 $W\ m^{-2}K^{-1}$ for wind a velocity of 1 $m\ s^{-1}$.

Figure 3.16 and figure 3.17 validate the surface temperature (Node 1000) for KFO and KAC, respectively, showing the temperature evolution as a function of time. The left y-axis represents temperature in °C, while the right y-axis indicates the percentage of error, ranging from 0-1%. The error is calculated using the formula:

$$error^n = \frac{T^n_{experimental}(K) - T^n_{runway\ model}(K)}{T^n_{experimental}(K)} \tag{3.2}$$

In both figures, the solid blue line represents the surface temperature predicted by the runway model, and the orange bars depict the experimental temperature results with the camera standard deviation. The purple circles indicate the percentage of error between the runway model and the experimental results.

For the experimental tests, a thermal camera (Optris Pi400) was used to measure the surface temperature. However, the standard deviation for this camera is not reported in the literature, and it was estimated by the camera manufacturer to be $\pm 2$ ℃ (Optris-GmbH-team).

As seen in the figures, the surface temperature decreases from -2°C to a minimum value before gradually increasing to between -9°C and -8°C after 30 minutes. In both deicers' cases, the system reaches the minimum temperature at the same time in the experimental test. As explained earlier, once the system reaches the equilibrium temperature, if it is not insulated and heat flux occurs from the surroundings, the temperature will rise. In this case, after reaching equilibrium, from 5 to 10 minutes, the temperature increases more slowly in the model than in the experimental results.

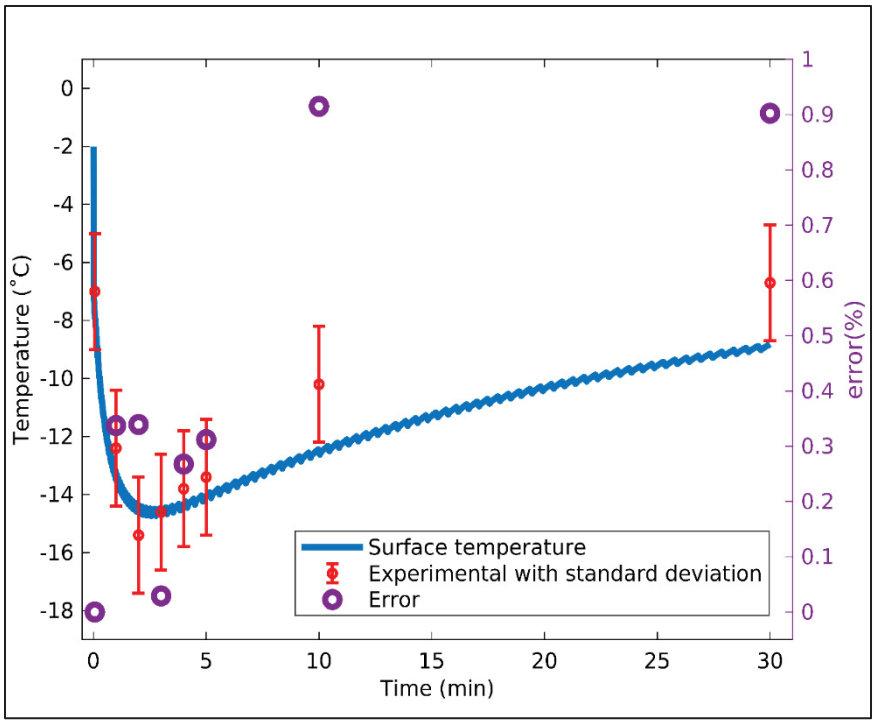


Figure 3.16 Surface temperature results.
Validation of the runway model for KFO after 30 min

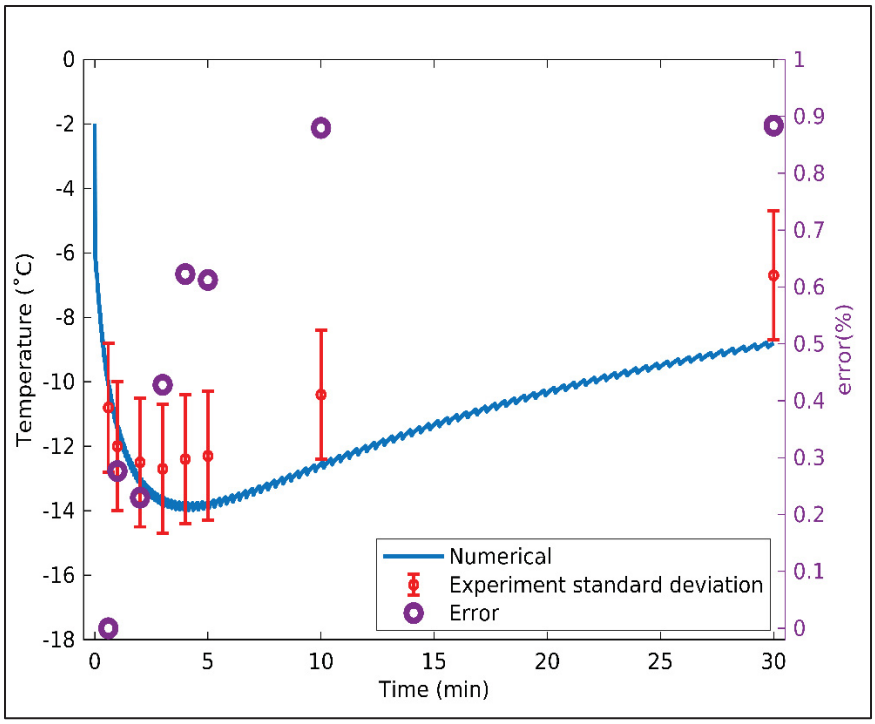


Figure 3.17 Surface temperature results.
Validation of the runway model for KAC after 30 min

One potential source of error lies in the fact that heat loss by convection was not measured during the experimental tests, and the runway model is sensitive to the heat convection coefficient. Additionally, in the experimental test, the solution does not uniformly cover the ice surface and tends to accumulate on one side of the Petri dish during temperature measurements. This uneven distribution can significantly affect the results, as the runway model is sensitive to the solution's thickness. The process of temperature measurement for KAC, along with supporting images, is thoroughly detailed in the article by (Charpentier et al., 2023). The temperature measured by the thermal camera represents the surface's minimum temperature over the Petri dish area. The model's sensitivity to the heat convection coefficient and solution thickness will be investigated in the parametric study section.

The calculated error for both deicing solutions is less than 1%, with a maximum error of 0.9% for KFO and 0.88% for KAC, occurring at 10 and 30 minutes. However, considering the camera's standard deviation, the model's temperatures could align with the experimental results.

Figure 3.18 and figure 3.19 validate the mass of ice melted after 30 minutes for KFO and KAC deicers, respectively. The left y-axis represents the mass in kg, while the right y-axis indicates the percentage of error. The error was calculated using the following formula:

$$error^n = \frac{m^n_{Deicer\ solution-experimental}(kg) - m^n_{Deicer\ solution-runway\ model}(kg)}{m^n_{Deicer\ solution-experimental}(kg)} \quad (3.3)$$

In both figures, the solid blue line represents the mass of ice melted predicted by the runway model, and the orange bars depict the experimental results with their standard deviation. The purple circles indicate the percentage of error between the runway model and the experimental results.

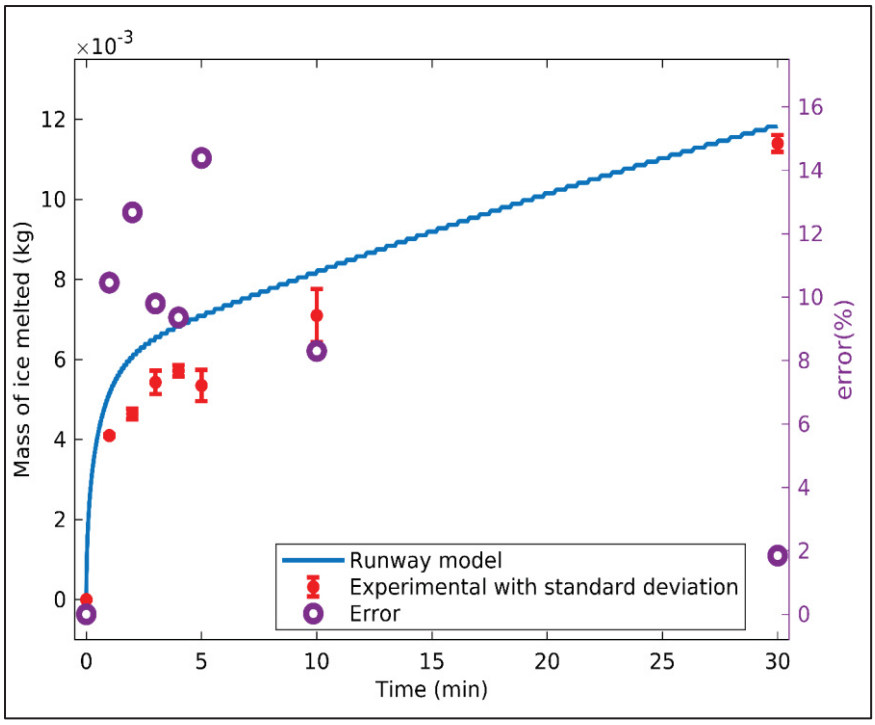


Figure 3.18 Mass of ice melted as a function of time.
Validation of the runway model for KFO after 30 min

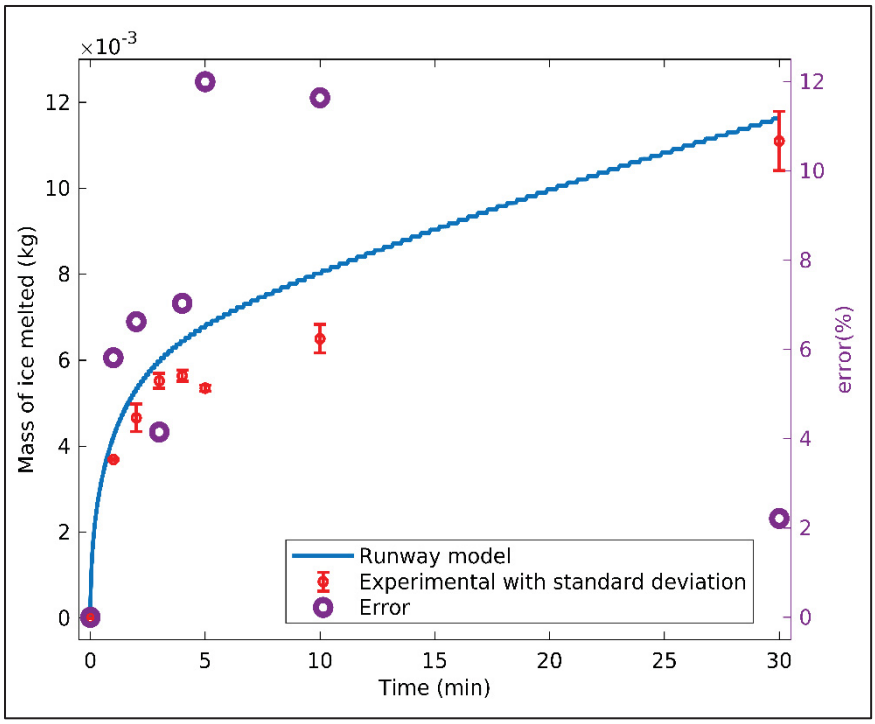


Figure 3.19 Mass of ice melted as a function of time.
Validation of the runway model for KAC after 30 min

After 30 minutes, the runway model shows agreement with the experimental data for both deicers. For KFO, there is a 2% error in the final mass of melted ice, with the experimental result being 11.4 g and the model predicting 11.8 g. For KAC, the error in the mass of melted ice is 2.1%, with the experimental test measuring 11.1 g and the model predicting 11.6 g. The model predicts slightly more ice melting within the first 2 minutes.

According to the numerical results, for KFO, the mass of ice melted starts to increase almost linearly with time after approximately 2 minutes. However, in the experimental data, this linear increase begins around 5 minutes. For KAC, both the experimental and numerical results show a linear increase in mass of ice melted starting after approximately 5 minutes. The maximum error occurs at 5 minutes, with a 15% error for KFO and a 11% error for KAC.

Figures 3.20 and 3.21 validate the solution concentration over 30 minutes for KFO and KAC deicers, respectively. The y-axis indicates the mass concentration (w/w%). The solid blue line represents the concentration predicted by the runway model, while the orange dots show the concentration calculated from the experimental results based on the mass of ice melted.
The concentration for the experimental results is calculated using the formula:

$$C^n = \frac{m_1(kg)}{m_{solution-initial}(kg) + m_{im}^n\,(kg)} \tag{3.4}$$

The predicted results from the runway model are in good agreement with the experimental results for both deicing solutions. At the end of the 30-minute period, the concentration for both deicing products stabilizes at approximately 0.15. Similar to the mass of ice melted, the maximum error occurs at the 5-minute mark.

For both deicing solutions, the runway model shows a linear decrease in concentration after the system reaches equilibrium temperature, at 2.5 minutes for KFO and 4 minutes for KAC. However, in the experimental results, there is a slight increase in concentration around 5 minutes, followed by a linear decrease. The slope of the concentration decrease for KAC before the 5-minute mark is nearly identical in both the experimental data and the runway model.

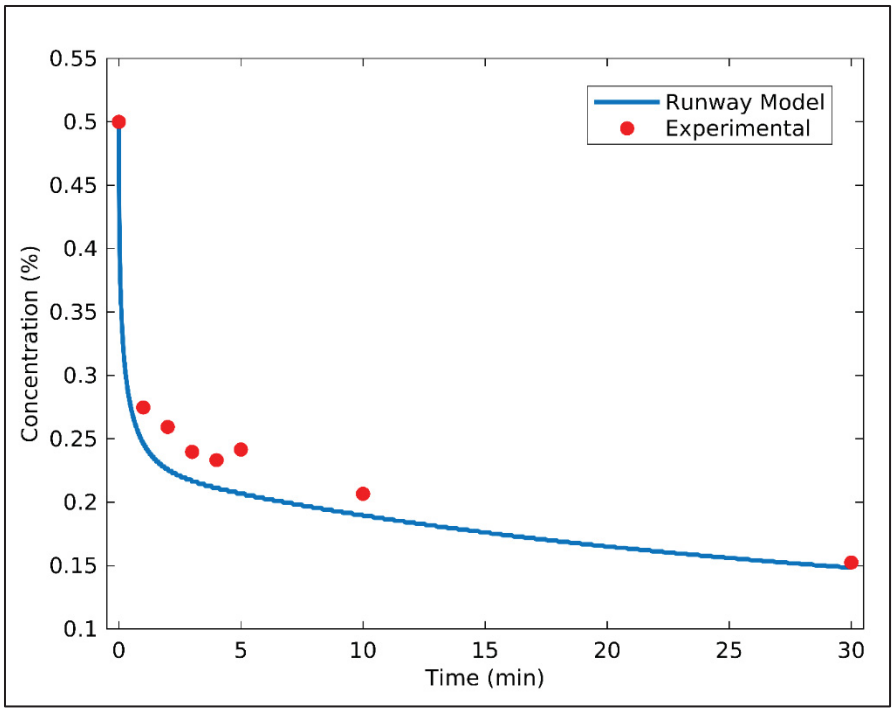


Figure 3.20 Concentration as a function of time.
Validation of the runway model for KFO after 30 min

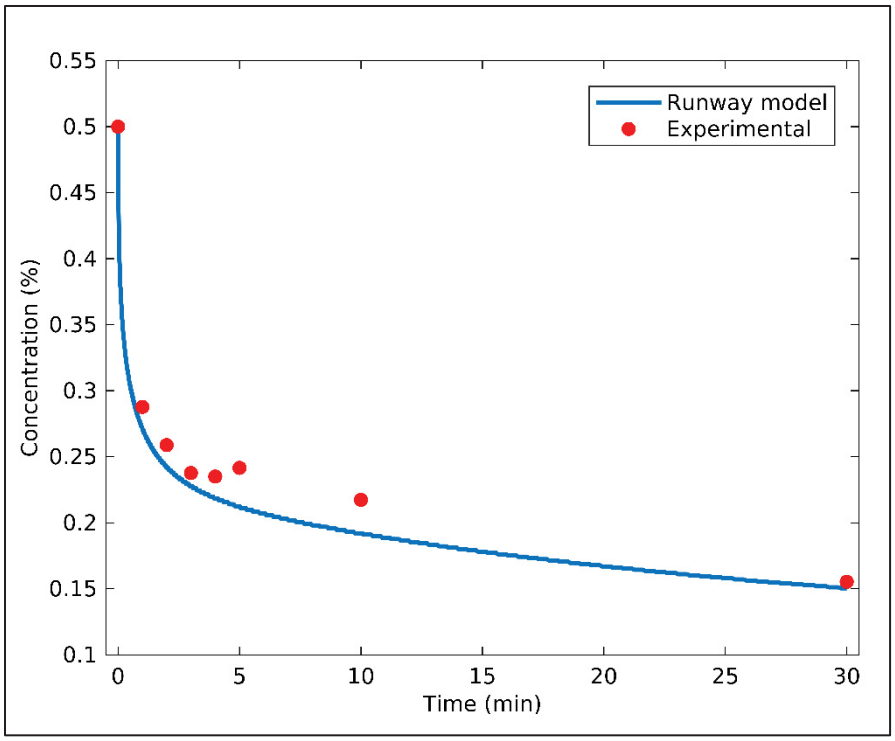


Figure 3.21 Concentration as a function of time.
Validation of the runway model for KAC after 30 min

### 3.2.2 Condition 2

Based on equation 2.24, initially the diffusion coefficients are $0.4 \times 10^{-9}\ m^2/s$ and $0.5 \times 10^{-9}\ m^2/s$ for KAC and KFO, respectively. Based on equation 2.12, the heat convection coefficient is 5.6 $W\ m^{-2}K^{-1}$ for wind velocity 0 $m\ s^{-1}$. As in Condition 1, a thermal camera (Optris Pi400) was used for surface temperature measurements with an estimated standard deviation of ±2 ℃. Additionally, the error was calculated based on Equation 3.2.

Figures 3.22 and 3.23 illustrate the surface temperature evolution over time for Condition 2, following the same color conventions and labels as Figures 3.16 and 3.17: the solid blue line represents the runway model's predicted surface temperature, orange bars show experimental temperature results with camera standard deviation, and purple circles indicate the percentage error.

The surface temperature decreases from -10°C to a minimum value before gradually increasing to a range between -16°C and -14°C after 30 minutes. For both deicing solutions, the minimum temperature predicted by the runway model is higher than the experimental results. For KFO, the minimum experimental temperature is -20.6°C, while the model predicts -19.1°C, resulting in an error of 0.37%. For KAC, the experimental minimum temperature is -21.4°C, whereas the model predicts -19.3°C, with an error of 0.69%.

After reaching equilibrium, the surface temperature for KFO shows a slight linear increase in both the experimental and numerical results. However, for KAC, the model predicts a slight linear increase, while the experimental data shows a decrease from -18.8°C to -19.1°C. This discrepancy leads to a maximum error for KAC of 1.2%, occurring at the end of the 30-minute period.

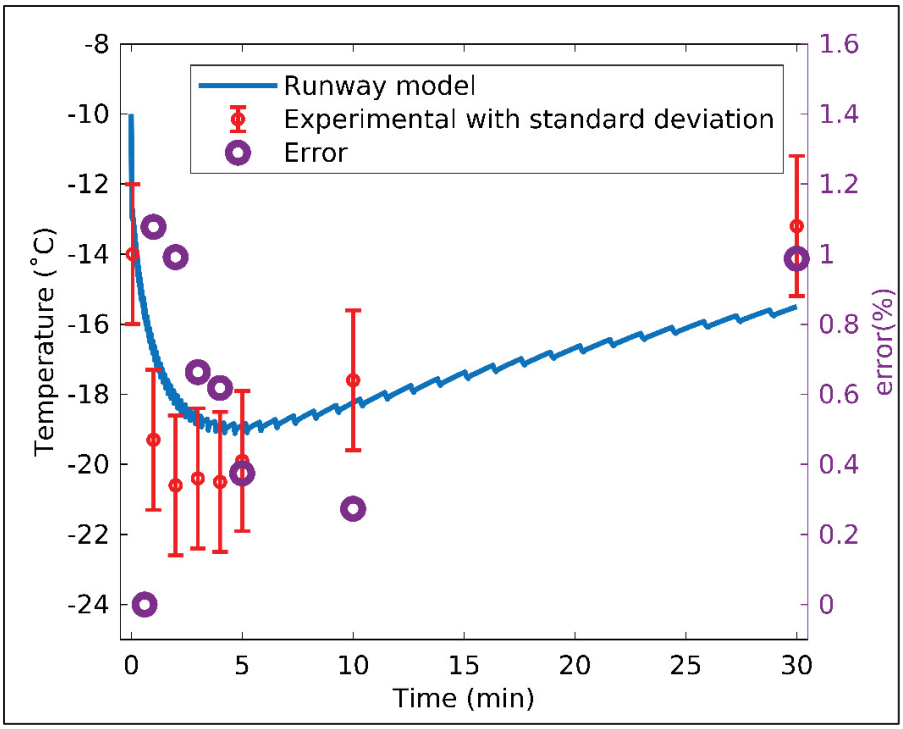


Figure 3.22 Surface temperature results.
Validation of the runway model for KFO after 30 min

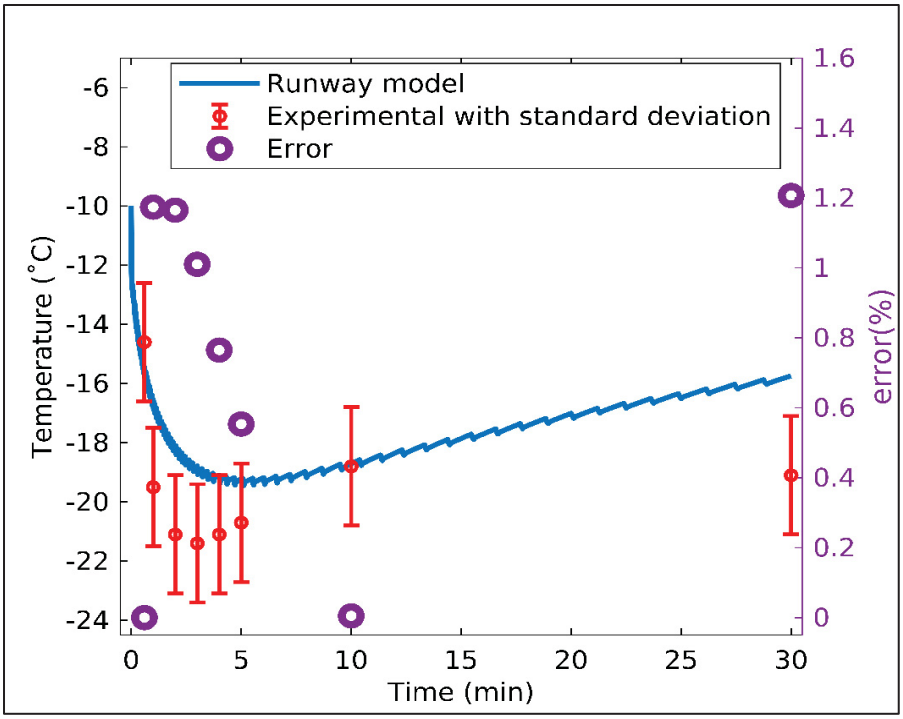


Figure 3.23 Surface temperature results.
Validation of the runway model for KAC after 30 min

The potential sources of error are like those in Condition 1. However, the differences in the results between the two conditions reveal some notable distinctions. For Condition 1, the maximum error is 0.9%, while in Condition 2, the maximum error increases to 1.2%, indicating slightly greater deviation. In Condition 1, the model's predicted minimum temperature closely follows experimental observations, with both trends showing a gradual temperature increase after equilibrium. However, in Condition 2, the runway model slightly overestimates the minimum temperature for both deicers, with KFO and KAC displaying errors of 0.37% and 0.69%, respectively, at the minimum point. After reaching equilibrium, Condition 1 shows a relatively constant temperature rise, whereas in Condition 2, KAC shows a minor decrease from -18.8°C to -19.1°C in the experimental data, while the model predicts a linear increase.

Figures 3.24 and 3.25 validate the mass of ice melted after 30 minutes for Condition 2. They follow the same color conventions and labels as Figures 3.18 and 3.19: the solid blue line represents the runway model's predicted mass of ice melted, the orange bars show the experimental results with standard deviation, and the purple circles indicate the percentage error, as calculated using Equation 3.3.

After 30 minutes, the runway model shows good agreement with the experimental data for KFO with a 4% error in the final mass of ice melted, the experimental result being 6 g and the model predicting 6.5 g. For KAC, the error in the mass of ice melted is 9%, with the experimental test measuring 5.7 g and the model predicting 6.7 g. The model predicts slightly more mass of ice melted over the 30-minute period.

The maximum error for both deicers occurred at t = 5 minutes, where the experimental data shows a slight decrease in mass of ice melted. Some amount of the deicing solution refreezes at this time. The maximum error for KFO is 11.8%, and for KAC, it is 16%. Additionally, we observe that ice melts more slowly compared to condition 1 (-2°C), as expected for lower temperatures.

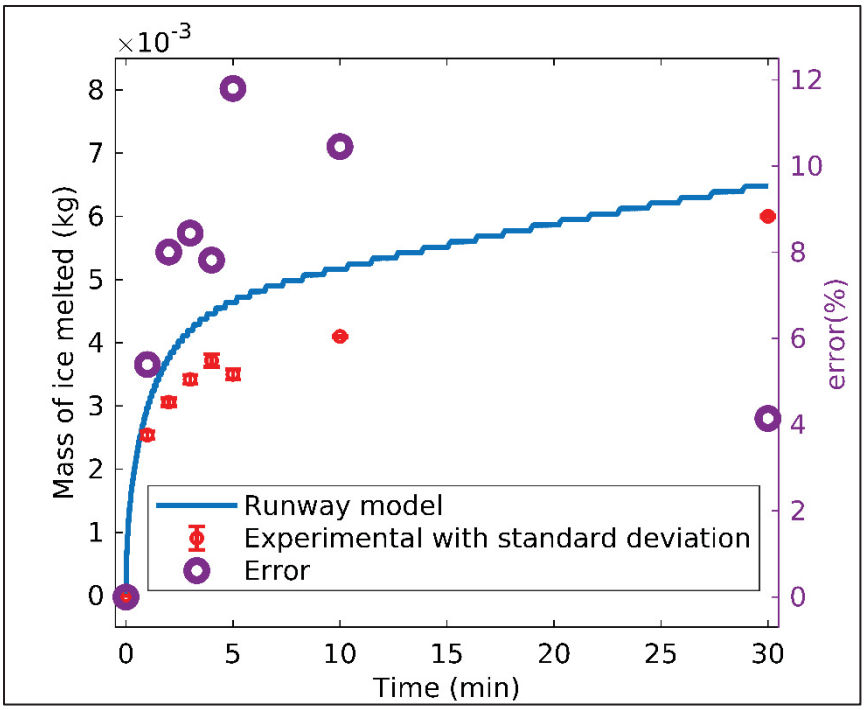


Figure 3.24 Mass of ice melted as a function of time.
Validation of the runway model for KFO after 30 min

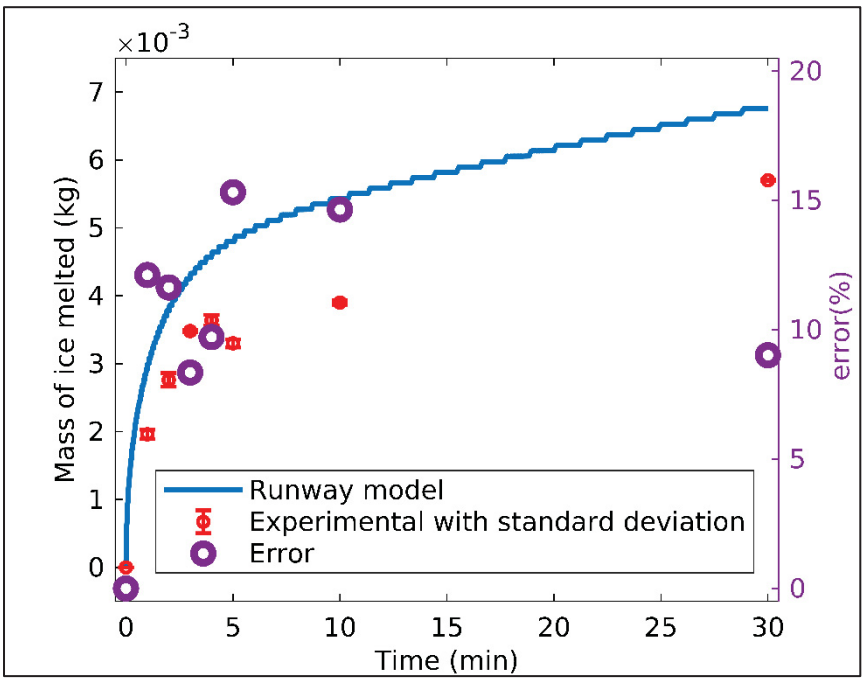


Figure 3.25 Mass of ice melted as a function of time.
Validation of the runway model for KAC after 30 min

Figures 3.26 and 3.27 validate the solution concentration over 30 minutes for Condition 2, following the same conventions as Figures 3.20 and 3.21. The solid blue line shows the concentration predicted by the runway model, while the orange dots represent the concentration derived from experimental measurements of mass of ice melted, as calculated using Equation 3.4.

As seen, the model aligns with the experimental results. By the end of the experiment, the concentration of the solution for KFO is 22.5% in the experimental data and 21.5% in the runway model. For KAC, the experimental result shows a concentration of 23%, while the runway model predicts 21%.

As for the mass of ice melted results, the largest error occurred at the 5-minute mark. At this point, the experimental concentration suddenly increased, whereas in the runway model, the concentration for both deicers decreased linearly. The concentration decreases rapidly from 0 to 4 minutes, then the decline becomes more gradual from 4 minutes until the end.

The validation results confirm the runway model's capability to predicts surface temperature, mass of ice melted, and solution concentration across two conditions (-2°C and -10°C), with discrepancies likely due to uncertainties in the heat convection coefficient and uneven solution distribution. For both deicers, the model demonstrates agreement with experimental data, with minimal errors observed in temperature and mass predictions.

The model's sensitivity to parameters such as the heat convection coefficient and solution thickness underscores areas for potential refinement. To deepen this analysis, the following parametric study evaluates these parameters' influence, providing insights into how variations could impact model results under diverse scenarios.

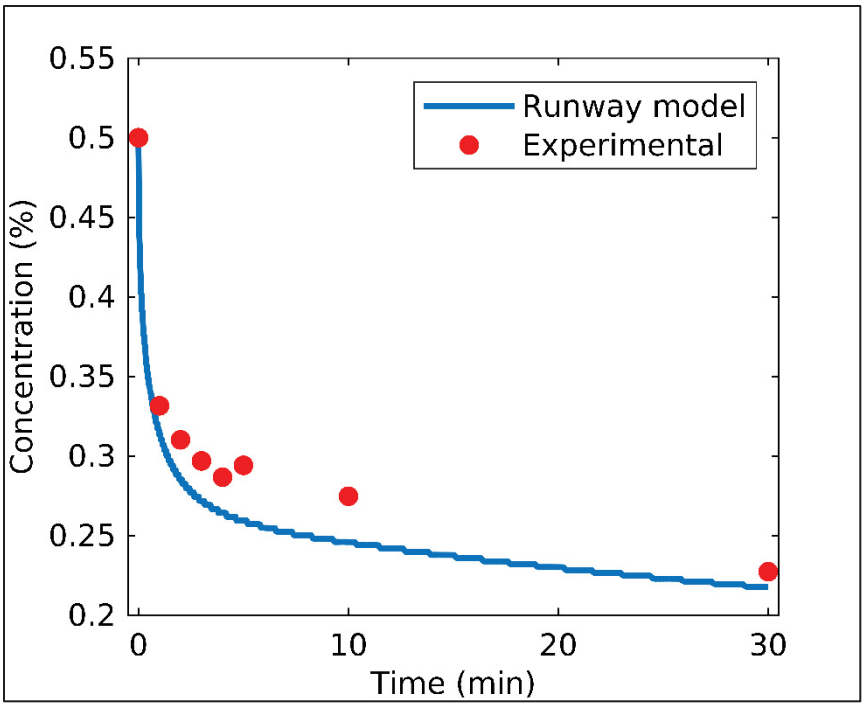


Figure 3.26 Concentration as a function of time.
Validation of the runway model for KFO after 30 min

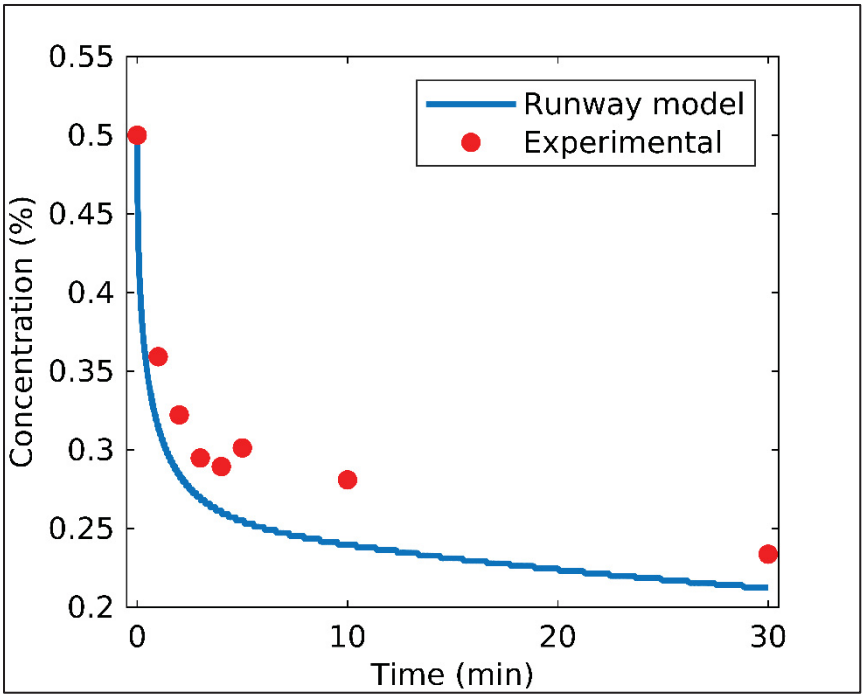


Figure 3.27 Concentration as a function of time.
Validation of the runway model for KAC after 30 min

## 3.3 Parametric study

In this section, we will first investigate the effect of the heat convection coefficient ($h_c$) by analyzing four different wind velocities. Following that, we will explore the consequences of the initial solution thickness on the results. Additionally, the influence of variable melting temperature will be studied, comparing results when the melting temperature is treated as a constant value (eutectic or equilibrium temperature) versus when it varies (as described in Eq 2.24).

For this analysis, the KFO will be used, with the values from Tables 3.1, 3.2, and 3.3, except for the following adjustments:

- In the first part, where we investigate the heat convection coefficient, the values for h correspond to wind velocities of 0, 1, 2, and 3 $m\ s^{-1}$.
- In the second part, we will analyze the results using two additional initial solution thicknesses alongside the value listed in Table 3.3.
- In the final part of this section, four different melting temperatures will be considered.

### 3.3.1 Influence of Heat Convection Coefficient Determined by Wind Velocity on the RDM Model at -2°C

We considered Condition 1, where all initial temperatures are -2°C. The heat convection coefficient values were selected from a range appropriate for natural convection, which varies between 2.5 to 25 $W\ m^{-2}K^{-1}$ . For light wind conditions, ranging from 0 $m\ s^{-1}$to 3 $m\ s^{-1}$ , the corresponding h values were calculated as 5.6, 9.6, 13.6 and 17.6 $W\ m^{-2}K^{-1}$ , respectively. Since in this study the wind velocity is the only factor that affects the heat convection coefficient (according to Equation 2.12), for simplicity, we refer to wind velocity in the results figures instead of the heat convection coefficient.

Figure 3.28 illustrates the effect of the heat convection coefficient over time (30 minutes) on three variables:

a. Surface temperature evolution.

b. The amount of ice melted.

c. The convective heat flux at the surface boundary.

The blue, orange, green, and purple lines correspond to wind velocities of 0, 1,2, and 3 $m\ s^{-1}$, respectively.

During the process, the ambient temperature remains at -2°C, which is warmer than the surface of the system. Consequently, heat flux is negative, meaning heat is transferred to the system. The convective heat flux increases with an increase in $h_c$, since the boundary condition at the surface only considers heat convection, and the ambient temperature remains constant throughout the process. Therefore, the only parameter affecting the heat flux at this boundary is the heat convection coefficient.

For the first two minutes, the system's temperature decreases as the ice absorbs energy from the deicing solution to overcome the latent heat of fusion. This energy is required for the phase transition from solid to liquid. Consequently, the system experiences a temperature drop, as the absorbed energy is drawn from it to facilitate the melting process. After this period, the convective heat flux from the surroundings becomes the dominant factor. As a result, an increase in convective heat flux causes the surface temperature to rise, leading to both an increase in the minimum temperature and the temperature after equilibrium is reached.

The minimum temperatures for $h_c$=5.6, 9.6, 13.6 and 17.6 $W\ m^{-2}K^{-1}$ are -15.31°C, -14.77°C, -14.29°C, and-13.87°C, respectively. Additionally, as the heat convection coefficient increases, the system reaches the minimum temperature faster. For $h_c$=5.6, 9.6, 13.6 and 17.6 $W\ m^{-2}K^{-1}$, the system reaches equilibrium at approximately 3.1, 2.6, 2.32, and 2.14 minutes, respectively. At the end of 30 minutes, the temperatures of the system are -10.72°C, -8.94°C, -7.05°C, and -6.8°C for the corresponding $h_c$ values.

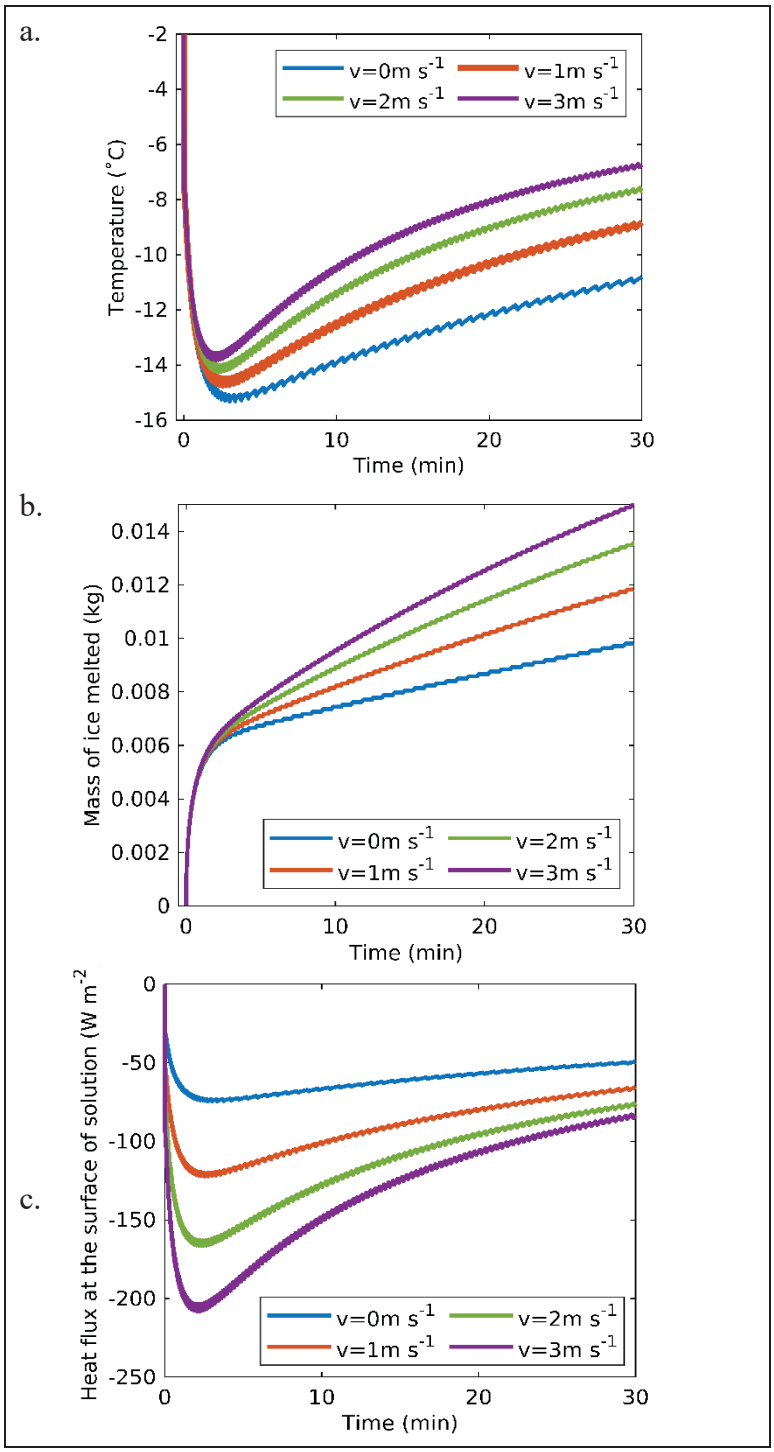


Figure 3.28 (a) Surface temperature (b) Mass of ice melted (c) Convective heat flux as a function of time for v= 0, 1, 2, 3 m $s^{-1}$ for 30 min

When the heat convection coefficient is higher, more heat is coming to the system at the interface, leading to an increase in the rate of ice melting. After the system reaches equilibrium, the heat convection coefficient plays a critical role in the total amount of ice melted. At the end of the 30-minute period, the mass of ice melted is 9.7g, 11.8g, 13.4g, 14.89g, for $h_c$=5.6, 9.6, 13.6 and 17.6 $W\ m^{-2}K^{-1}$, respectively.

### 3.3.2 Effect of Deicing Solution Thickness Determined by Mass on the RDM Model at -10°C

Here, we considered condition 2, where all the temperatures are at -10°C. In this scenario, we aim to investigate the model's sensitivity to the deicing solution thickness. According to Equation 2.20, the thickness in the runway's 1D model depends on the mass of the deicing solution and the area considered. Therefore, two approaches are taken for this investigation: one is to analyze the results for different initial masses of the deicing solution, and the other is to study different area sizes.

We chose the first approach to evaluate the effect of the deicing solution thickness. Figures 3.29, 3.28, and 3.29 illustrate the surface temperature, the mass of ice melted, and the concentration of the solution over time for three different initial masses of the deicing solution: 5g, 7g, and 10g, which correspond to initial deicing solution thicknesses of $2.06 \times 10^{-4}\ m$, $2.88 \times 10^{-4}\ m$, and $4.11 \times 10^{-4}\ m$, respectively, based on Equation 2.20. The blue, orange, and purple lines represent m= 5, 7 and 10 g, respectively.

As observed, increasing the initial thickness of the deicing solution leads to an increase in the mass of ice melted and a decrease in the surface temperature. When the solution thickness is greater, there is a larger liquid region in the system. As mentioned earlier, the freezing point of the solution decreases based on its concentration. When ice melts, it dilutes the solution. Thus, with a greater initial solution thickness, the solution dilutes more slowly. As shown in Figure 3.30 and figure 3.31, when the solution concentration remains higher, more ice melts. Additionally, the melting temperature increases more gradually because it depends on the

concentration. Therefore, the surface temperature decreases further, and the system takes longer to reach equilibrium.

The minimum temperatures m=5, 7, 10g are -19.8°C, -20.91°C, and -22.04°C, occurring around t= 4, 6 and 7 minutes, respectively. Correspondingly, the amount of ice melted at the end of 30 minutes is 6.3g, 8.2g, and 9.9g for the respective initial masses. The concentration of the deicing solution at the end of 30 minutes is 21%, 22%, and 25% for the respective initial masses m=5, 7, 10g.

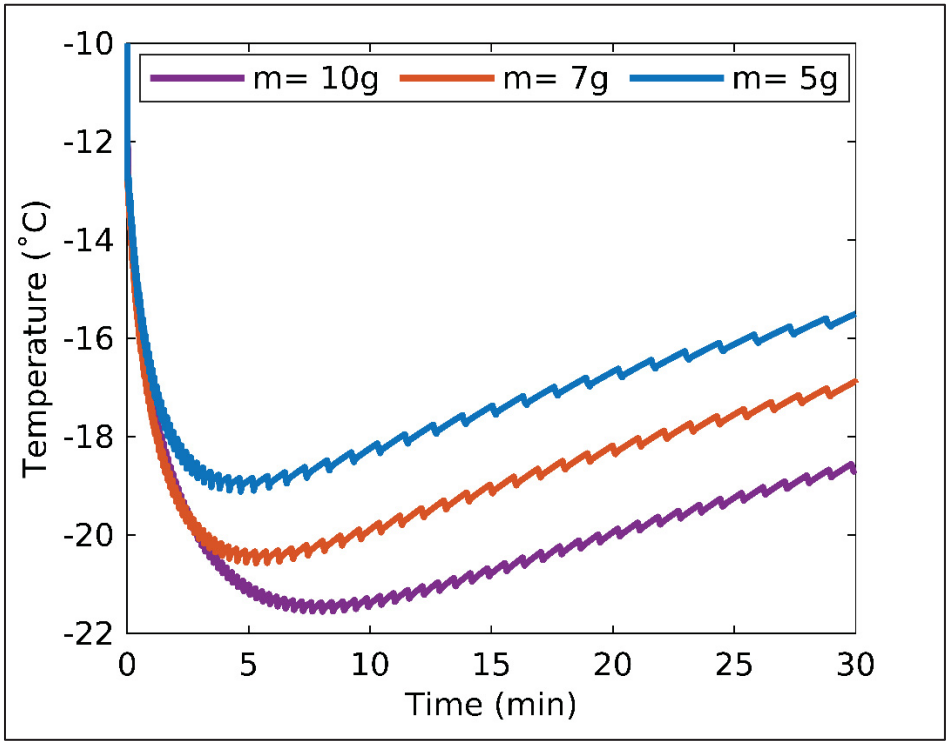


Figure 3.29 Temperature as a function of time
for m=5, 7, 10g for 30 min

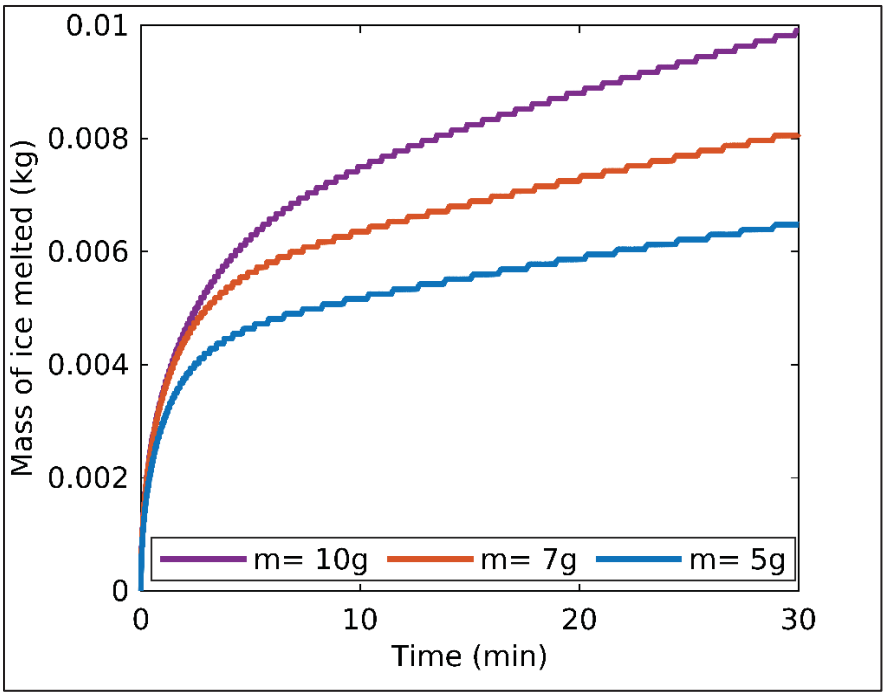


Figure 3.30 Mass of ice melted as a function of time,
for m=5, 7, 10g for 30 min

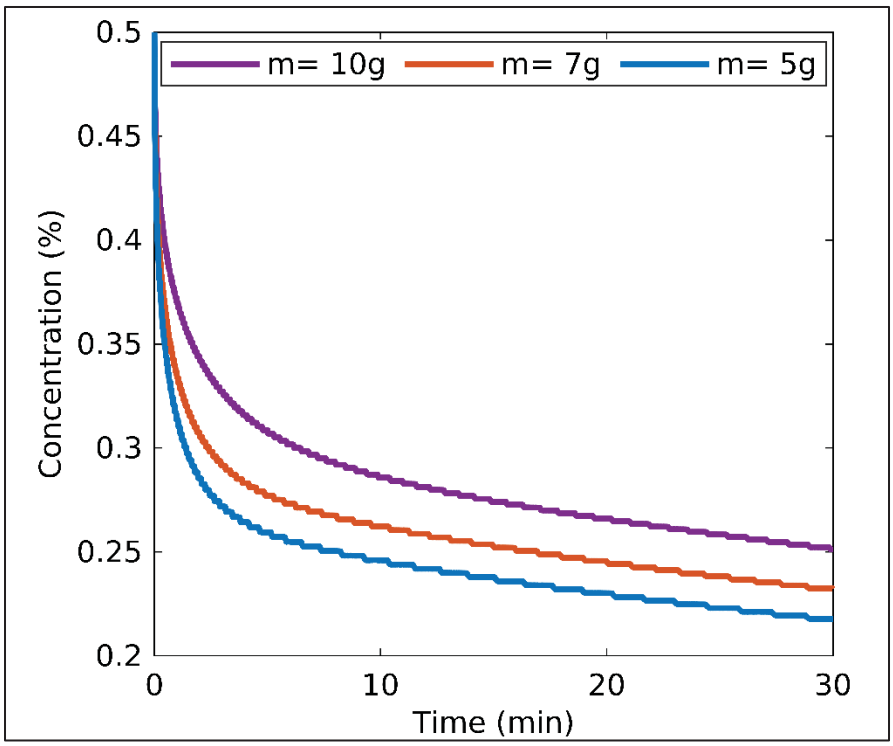


Figure 3.31 Concentration as a function of time
for m=5, 7, 10g for 30 min

The primary thickness effect is on the equilibrium temperature and the time it takes for the system to reach the equilibrium. After the equilibrium is reached, the rate of temperature increase (Figure 3.29), the mass of ice melted (Figure 3.30), and the decrease in concentration (Figure 3.31) are approximately the same for the three initial thicknesses. For example, the melting rates for initial thickness of deicing solution $2.06 \times 10^{-4}\, m$, $2.88 \times 10^{-4}\, m$, and $4.11 \times 10^{-4}\, m$, after the equilibrium (from 5 to 30 minutes), are 0.06 $g\ \mathrm{min}^{-1}$ , 0.09 $g\ \mathrm{min}^{-1}$, 0.1 $g\ \mathrm{min}^{-1}$, respectively.

We calculated the change in melted ice mass per unit increase in deicing solution thickness $\Delta m_{melted\ ice} / \Delta H_{initial}$:

- From 5g to 7g (with thickness change from $2.06 \times 10^{-4}\, m$ to $2.88 \times 10^{-4}\, m$), the rate is approximately $18.29\ g/m$.
- From 7g to 10g (thickness change from $2.88 \times 10^{-4}\, m$ to $4.11 \times 10^{-4}\, m$), the rate is approximately $16.26\ g/m$.

### 3.3.3 Effect of the Melting Temperature as a Function of Concentration on the RDM Model at -2°C

Figures 3.32 and 3.33 illustrate the impact of the melting temperature on the system's temperature and the mass of melted ice, respectively. Unlike previous studies, which empirically estimate the melting rate and use it to calculate concentration and melting temperature indirectly (e.g., from freezing point-concentration diagrams), this model integrates the melting temperature directly into the thermal calculations. Importantly, the model accounts for changes in melting temperature as a function of concentration, providing a more realistic and dynamic representation of the melting process.

To investigate the sensitivity of the system to melting temperature, the study examines four scenarios. In three cases, constant melting temperatures are used: the eutectic melting temperature of the KFO solution (green line), and fixed values of -10°C (orange line) and -20°C (pink line), both below the melting temperature of pure ice. In the fourth scenario, the

melting temperature is dynamically updated at each time step based on concentration using Equation 2.25 (blue line).

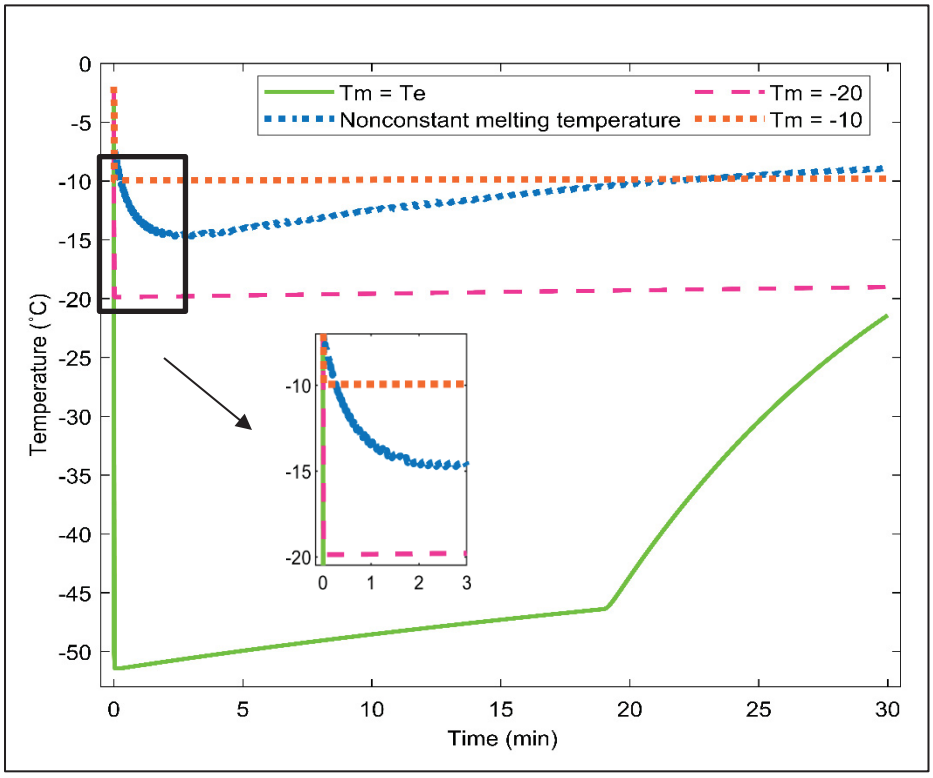


Figure 3.32 Surface temperature
as a function of time using different melting temperatures
-10, -20℃, Te, and non-constant melting temperature

Figure 3.32 shows that the surface temperature is strongly tied to the melting temperature. With a constant melting temperature, the system's thermal trajectory shows a steep decline until it reaches the prescribed melting temperature.

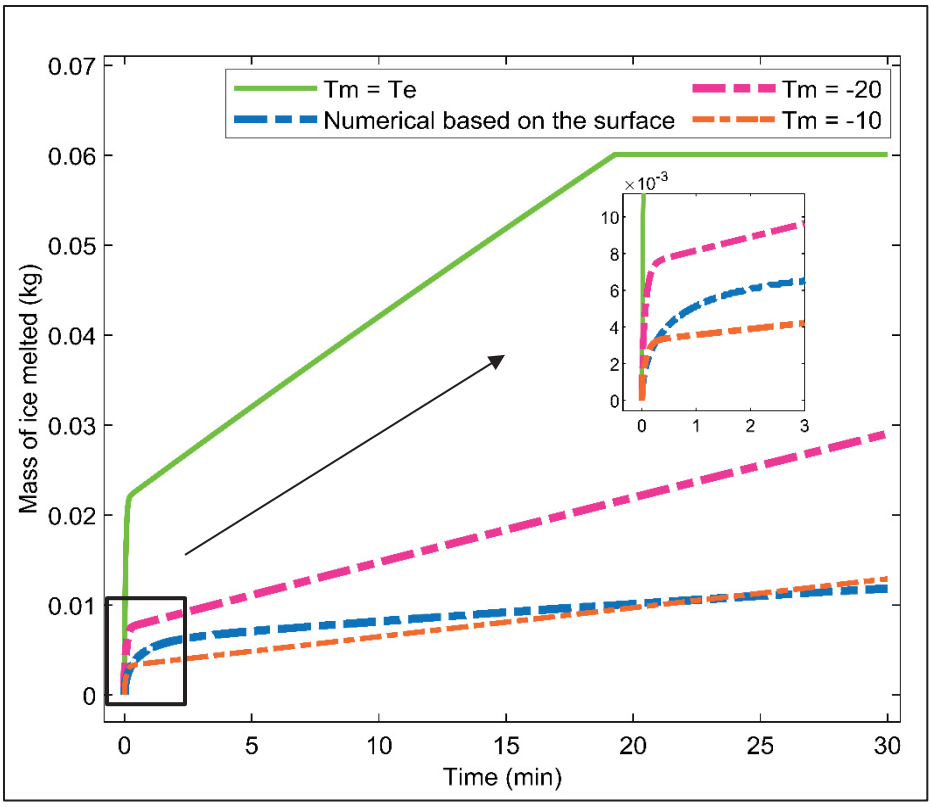


Figure 3.33 Mass of melted ice
as a function of time using different melting temperatures
-10˚C, -20℃, Te, and non-constant melting temperature

After reaching equilibrium, there is a slight uptick in temperature due to convective heat flux from the surroundings maintained at -2 °C. This warmer ambient temperature provides the latent heat necessary to continue melting the ice. The convective heat flux on the surface of the solution, for the non-constant melting temperature scenario, is shown in Figure 3.34.

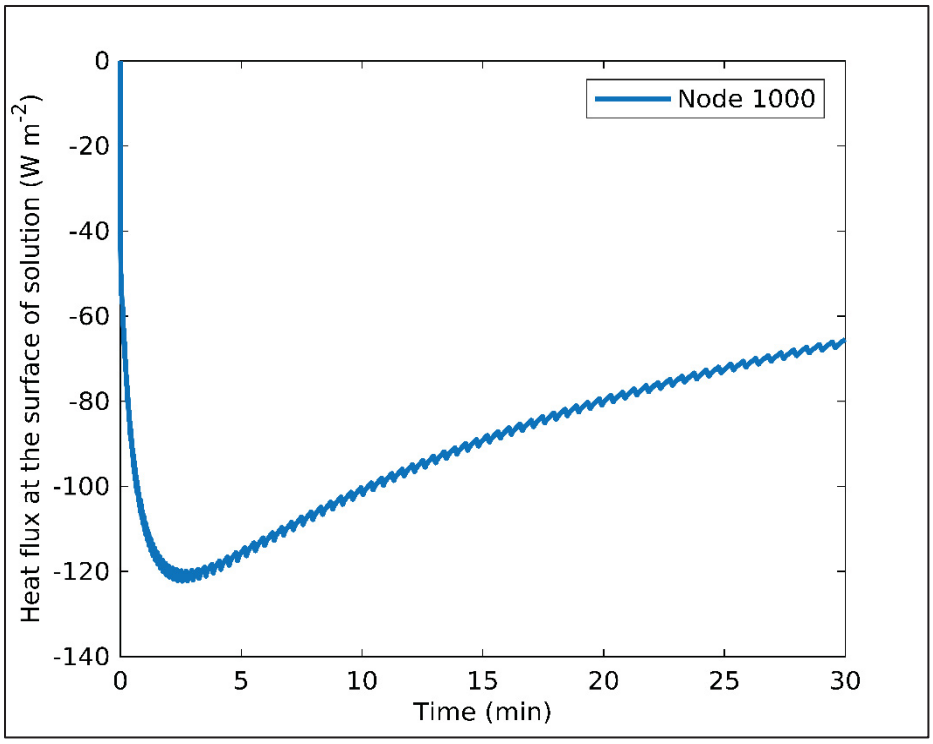


Figure 3.34 Convective heat flux as a function of time for 30 min

When the melting temperature is -52 °C (eutectic temperature), a distinct pattern emerges with the system's temperature stabilizing at -52 °C. Following this equilibrium phase, the temperature increases due to convective heat flux from above and latent heat absorbed during ice melting, persisting until t=19 minutes. This is due to the greater temperature differential between the surrounding air and the system, and the rapid ice melting at lower temperatures, leading to higher latent heat release. Beyond t=19 minutes, when the ice is completely melted, the absorption of latent heat stops, and a sharp rise in system temperature occurs as the system absorbs additional heat from the surroundings, readjusting to a new equilibrium state after the phase change stops.

Figure 3.33 shows that, in all scenarios, there is a sharp increase in the mass of ice melted until the system attains its equilibrium temperature, which corresponds to the melting point temperature. After this, the melting of ice continues. When the melting temperature aligns with the eutectic temperature (-52 °C), the entire ice mass melts before the 20 minutes mark. In the

cases with constant melting temperatures of-10 °C and -20 °C, the melting process unfolds with a consistent slope. For a melting temperature of -10 °C, the rate of increase in melted ice mass is smaller compared to the -20 °C case. This discrepancy is due to the external temperature being a constant -2 °C, resulting in convective heat flux from above the system. Consequently, a lower system temperature yields a higher heat flux from the surrounding air, leading to more pronounced melting. When the melting temperature is dynamic and varies based on concentration, the slope of the curve changes according to the melting temperature of the solution.

In scenarios where the melting temperature is held constant at -10℃, there is a slightly greater amount of ice melted within 30 minutes compared to instances with a non-constant melting temperature, with the same initial mass of the deicing solution. The KFO solution's concentration, calculated using equation 2.46 for a melting temperature of -10℃, is determined to be 9.4%. Conversely, in cases of non-constant melting temperature, the initial concentration of the KFO solution is 50%. Initially, a higher quantity of ice melts in non-constant melting temperature conditions; however, due to the subsequent dilution of the solution, the melting rate decreases over time. Consequently, the study on melting temperature indicates that maintaining a constant melting temperature throughout the process leads to a higher overall ice melting rate. This outcome is achievable when the concentration of the solution remains constant by reapplying deicer chemicals to sustain a consistent concentration during the deicing process. We will investigate the reapplication of deicer under runway conditions in the third section that follows.

## 3.4 Runway Conditions in the RDM Model

The dimensions of one of the runways at Aéroport de Montréal are 3,650 meters in length and 60 meters in width. For study purposes, we consider a smaller area measuring 1 meter by 1 meter. Based on the online documents, the initial thickness of the ice layer on the runway is typically 2.54 centimeters (Peters-chemical-company). We begin by applying 150 grams of a deicing solution with a 50% concentration (Cryotech-Deicing-Technology). The wind velocity is assumed to be 3 ($m\ s^{-1}$). Based on Equation 2.11, the initial heat transfer coefficient at this

wind speed is h= 17.6 ($W\ m^{-2}\ K^{-1}$). Additionally, thermal radiation is considered from above the solution layer. We will analyze the results over a span of 60 minutes. All the properties used are presented in Table 3.1.

First, we compare the melting rates of two runway deicing products, KAC and KFO, under two conditions: at -2°C (Condition 1) and at -10°C (Condition 2), to determine which product can melt more mass of ice under runway conditions.

we aim to investigate how frequently 150 g/m² of KFO needs to be reapplied. We present the temperature variations and amounts of ice melted for various reapplication frequencies in three scenarios: reapplication every 30 minutes, every 20 minutes, and every 15 minutes. We considered a condition where all the temperatures are initially -2°C (Condition 1).

### 3.4.1 Performance Evaluation of KAC and KFO Deicers at -2°C and -10°C

Figures 3.35 and 3.36 show the mass of ice melted and the concentration of KAC and KFO over a 60-minute period under Condition 1 (temperature at -2°C), respectively. The y-axis displays the mass of ice melted in kilograms and the concentration percentage, while the x-axis represents time in minutes. The blue line indicates the performance of KAC, while the orange line corresponds to KFO.

As shown in Figure 3.35, KAC melts more ice than KFO between 10 and 60 minutes. By the end of the 60-minute period, 0.92 kg of ice had melted with KAC, compared to 0.88 kg with KFO. In Figure 3.36, a zoomed-in view of the final moments (58 to 60 minutes) reveals that the concentration of KAC is 0.3% lower than that of KFO, as the greater mass of melted ice in the KAC solution leads to further dilution.

Table 3.4 provides a comprehensive breakdown of the melting rates for KAC and KFO at -2°C. The table details the melting rates, measured in kilograms per minute, at various time intervals over the 60-minute duration. A closer analysis of the data reveals that KAC consistently demonstrates higher melting rates than KFO at every time interval.

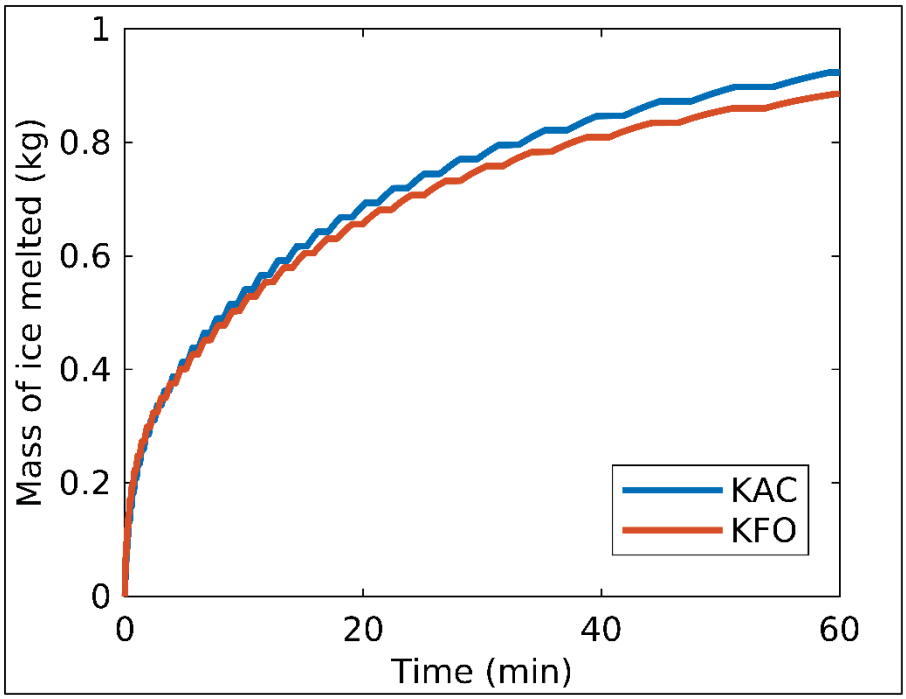


Figure 3.35 Mass of ice melted, KAC (blue line), and KFO (orange line) as a function of time for condition 1 (-2°C)

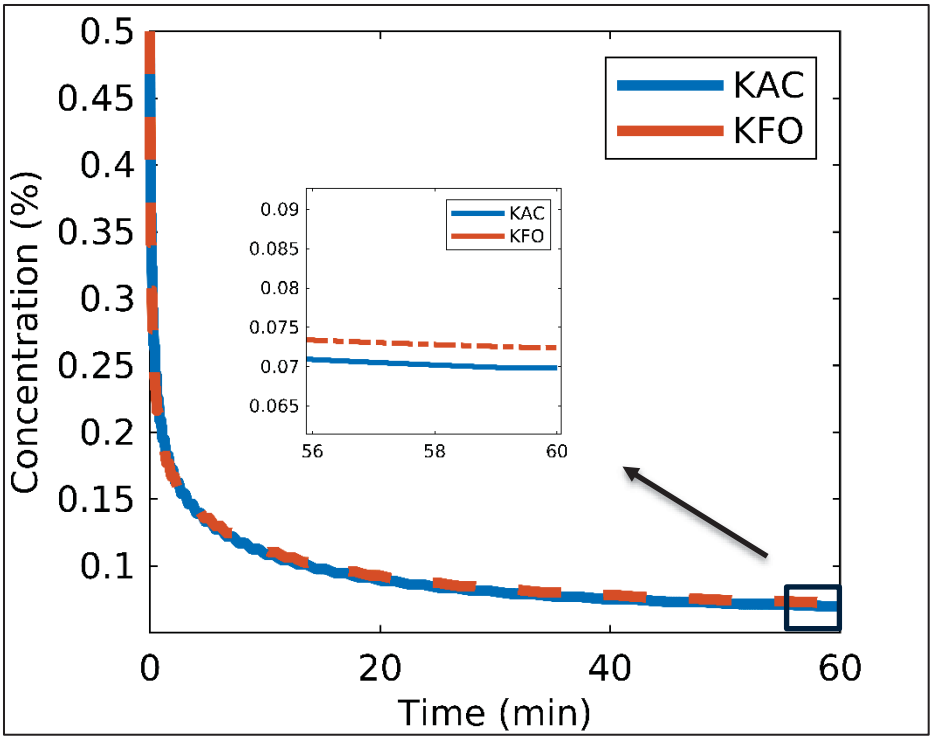


Figure 3.36 Concentration of KAC (blue line), and KFO (orange line) as a function of time for condition 1 (-2°C)

Table 3.4 Melting rates kg/min for two deicer KAC and KFO at condition -2 °C

| Time (min) / Deicer | 1 | 10 | 20 | 30 | 40 | 50 | 60 |
|---|---|---|---|---|---|---|---|
| KAC kg/min | 0.219 | 0.054 | 0.034 | 0.026 | 0.021 | 0.018 | 0.015 |
| KFO kg/min | 0.233 | 0.051 | 0.032 | 0.025 | 0.020 | 0.017 | 0.014 |

Both deicers exhibit a gradual decrease in their melting rates over time. The largest difference occurs at t=10 minutes, where KAC melts approximately 30 grams more ice than KFO.

Figure 3.37 depicts the location of the melting front over a 60-minute period. The results show that within this timeframe, only 0.1 cm of ice melted with KAC and 0.09 cm with KFO. This falls significantly short of the goal to deice a runway covered with 2.54 cm of ice. However, it's important to note that the primary aim of applying deicer is not necessarily to melt all the ice but to weaken the bond between the ice and the runway, thereby facilitating easier mechanical removal. Several factors could explain the reason for the melting of the small mass of ice. First, the model does not account for certain physical effects, such as heat generated by deicer trucks or airplane tires. Additionally, the deicing solution may not have been applied evenly across the ice surface, potentially leading to areas of enhanced melting where the solution penetrated under the ice.

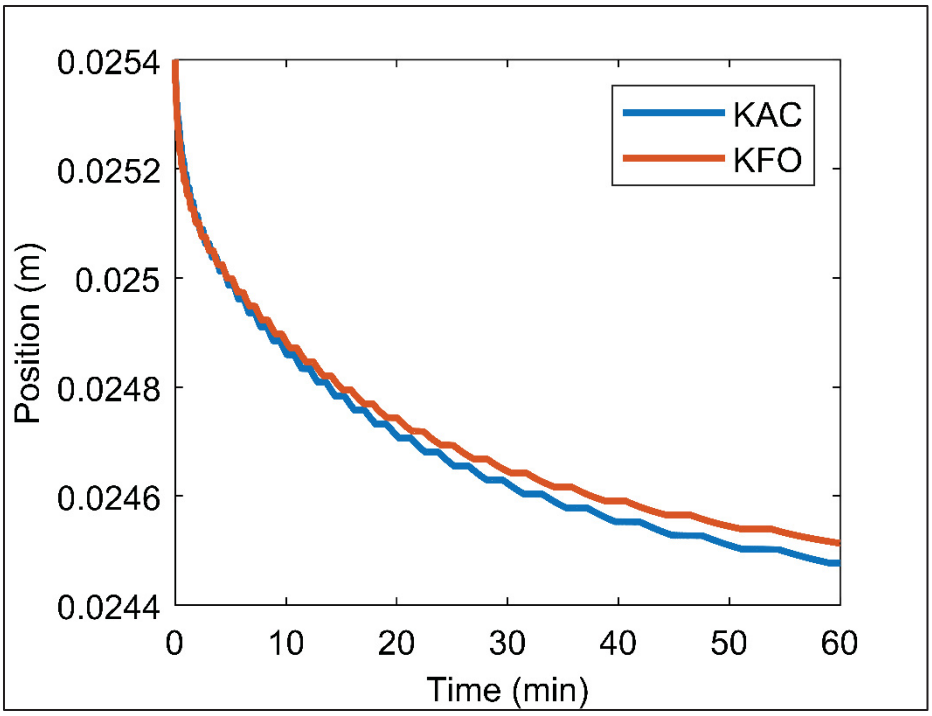


Figure 3.37 Melting front location of KAC (blue line), and KFO (orange line) as a function of time for condition 1 (-2°C)

Moreover, as shown in Figure 3.38, the concentration of the deicing solution is low at 60 minutes, around 7%. The corresponding melting point for a solution with this concentration is approximately -2°C. Since both the ambient air and the runway pavement temperatures are -2°C, the solution cannot melt additional ice at this concentration.

Figure 3.38 shows the amount of ice melted by KAC and KFO over a 60-minute period under condition 2, where the temperature is -10°C. The y-axis represents the mass of ice melted in kilograms, while the x-axis indicates the time in minutes. The blue line corresponds to KAC, and the orange line represents KFO. Figure 3.39 illustrates the surface temperature (solid line) compared to the melting temperature (dashed line) for KAC and KFO over the same 60-minute period at -10°C. The y-axis shows temperature values, and the x-axis represents time in minutes. The blue line denotes KAC and the orange line denotes KFO.

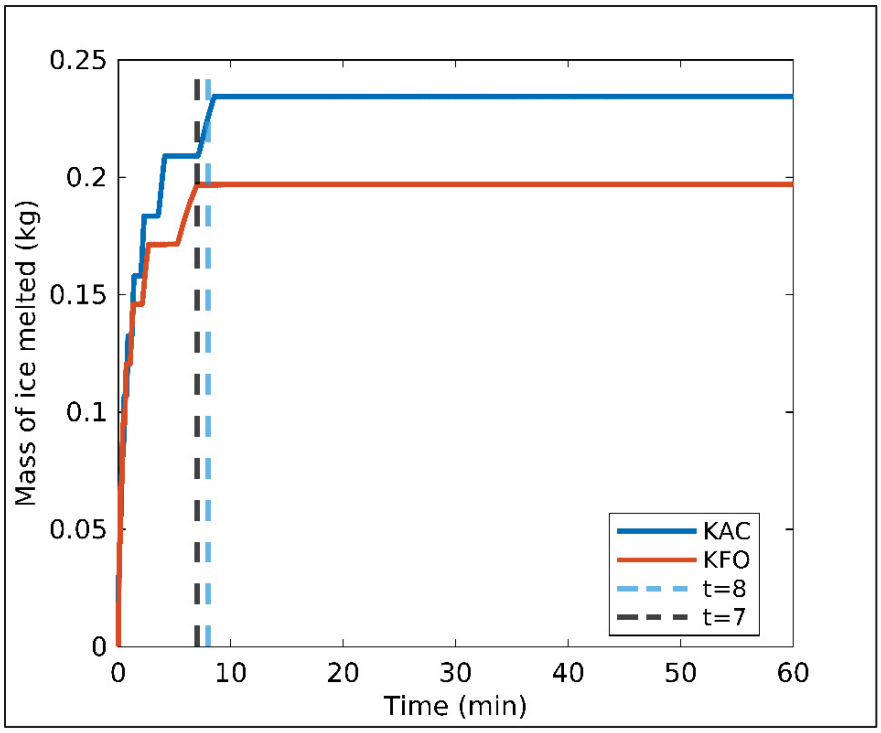


Figure 3.38 Mass of ice melted, KAC (blue line),
and KFO (orange line) as a function of time for condition 2 (-10°C)

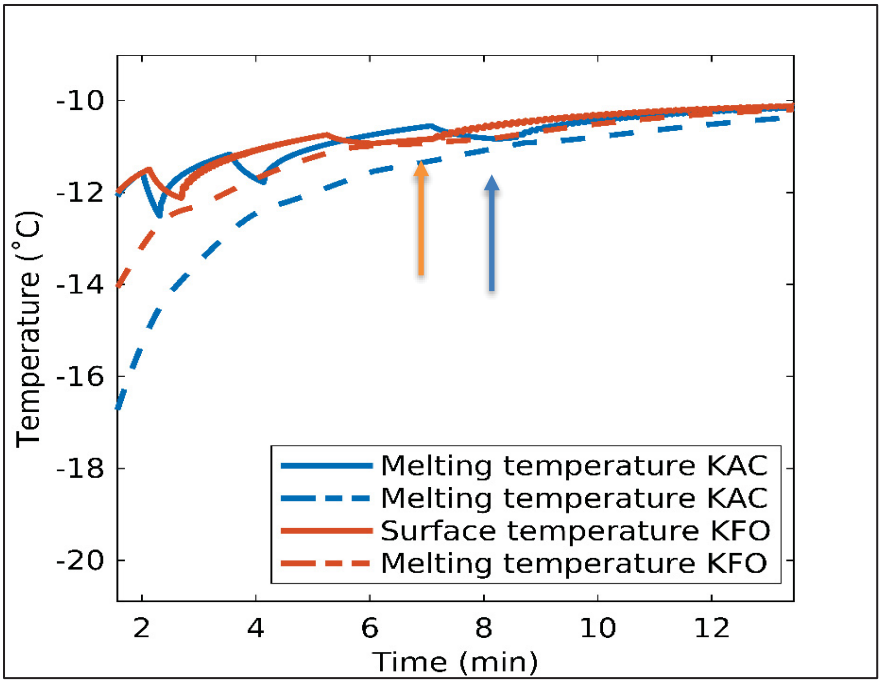


Figure 3.39 Temperature and melting temperature, KAC (blue line),
and KFO (orange line) as a function of time for condition 2 (-10°C)

In Figure 3.38, we observe that the melting process continues until approximately 8 minutes (blue dashed line) for KAC and 7 minutes (orange dashed line) for KFO. By the end of this period, KAC has melted 32 grams more ice than KFO. The total mass of ice melted is 232 grams for KAC and 200 grams for KFO. The reason the melting process halts can be understood from Figure 3.39. At around 8 minutes for KAC and 7 minutes for KFO, the surface temperature reaches the melting point of the respective solutions. Moreover, the temperature, between -10°C and -11°C, is close to the ambient and runway surface temperatures, meaning not enough additional heat is available to continue melting the ice.

Table 3.5 provides a detailed summary of the melting rates for KAC and KFO at -10°C. The table lists melting rates, measured in kilograms per minute, at various intervals over the 60-minute period. The data clearly show that KAC consistently exhibits higher melting rates than KFO throughout all time intervals.

Table 3.5 Melting rates kg/min of two deicer KAC and KFO for -10 °C

| Time (min) / Deicer | 1 | 2 | 3 | 4 | 6 | 7 | 8 |
|---|---|---|---|---|---|---|---|
| KAC kg/min | 0.13 | 0.079 | 0.061 | 0.51 | 0.034 | 0.031 | 0.029 |
| KFO kg/min | 0.12 | 0.073 | 0.057 | 0.043 | 0.030 | 0.028 | 0.024 |

### 3.4.2 Impact of Deicer Reapplication Frequency on Ice Melting and Surface Temperature on Runways

The deicer reapplication frequency refers to how often deicers are reapplied to a runway to maintain effective deicing during winter conditions. According to information from

Association-québécoise-des-transports (2011) on runway operations, it takes approximately 12 minutes to prepare equipment, including deicing trucks and snow removal machinery, and to spread deicing chemicals over the runway. Given this, we decided that a minimum of 15 minutes is required between deicer applications.

We will evaluate the impact of deicer reapplication frequency on the thickness of ice melted and the surface temperature of the solution under three scenarios:

1. Reapplying 150 $gm^{-2}$of solution at t=30min.
2. Reapplying 75 $gm^{-2}$of solution every 20 minutes (at t=20 and t=40 minutes).
3. Reapplying 50 $gm^{-2}$of solution every 15 minutes (at t=15, t=30, and t=45 minutes).

Figures 3.40a and 3.40b illustrate the melting front location and the mass of ice melted over a 60-minute period, respectively. The blue line represents the scenario without reapplication, while the purple, green, and orange lines correspond to scenarios 1, 2, and 3, respectively.

The scenario without reapplication serves as a baseline for comparison. In this baseline scenario, the mass of ice melted is significantly lower compared to the reapplication scenarios. With no reapplication, the melting front advances to a location of 0.0245 m, resulting in a total of 0.9 kg of ice melted.

The results indicate that reapplying the full 150 g of deicer in a single reapplication (Scenario 1) and 75g every 20 minutes (Scenario 2) result in the amount of melted ice at the end (1.33 kg of ice melted) which is greater than when splitting the total amount into smaller applications at shorter intervals (Scenarios 3, with 1.25 kg of ice melted). This is because adding a larger mass of deicer significantly increases concentration, leading to a greater reduction in surface temperature and melting temperature. Consequently, more heat is transferred from the air into the ice, accelerating melting rates in Scenarios 1 and 2. For instance, in Scenario 1, reapplying 150 g of deicer at once sharply increases the concentration within the system, from nearly 0%

to 25%, which significantly accelerates the melting rate, as demonstrated in Figure 3.41. This rapid increase in concentration causes the melting front to progress more quickly.

In Scenario 3, where smaller amounts of deicer are applied more frequently, the first reapplication at 15 minutes raises the concentration from 5% to 22%. However, by the second reapplication at t = 30 minutes, adding 50 g of deicer no longer causes a significant change from 5% to 14% in concentration (less than 10%), resulting in a stable melting rate without further increases.

a.

b.

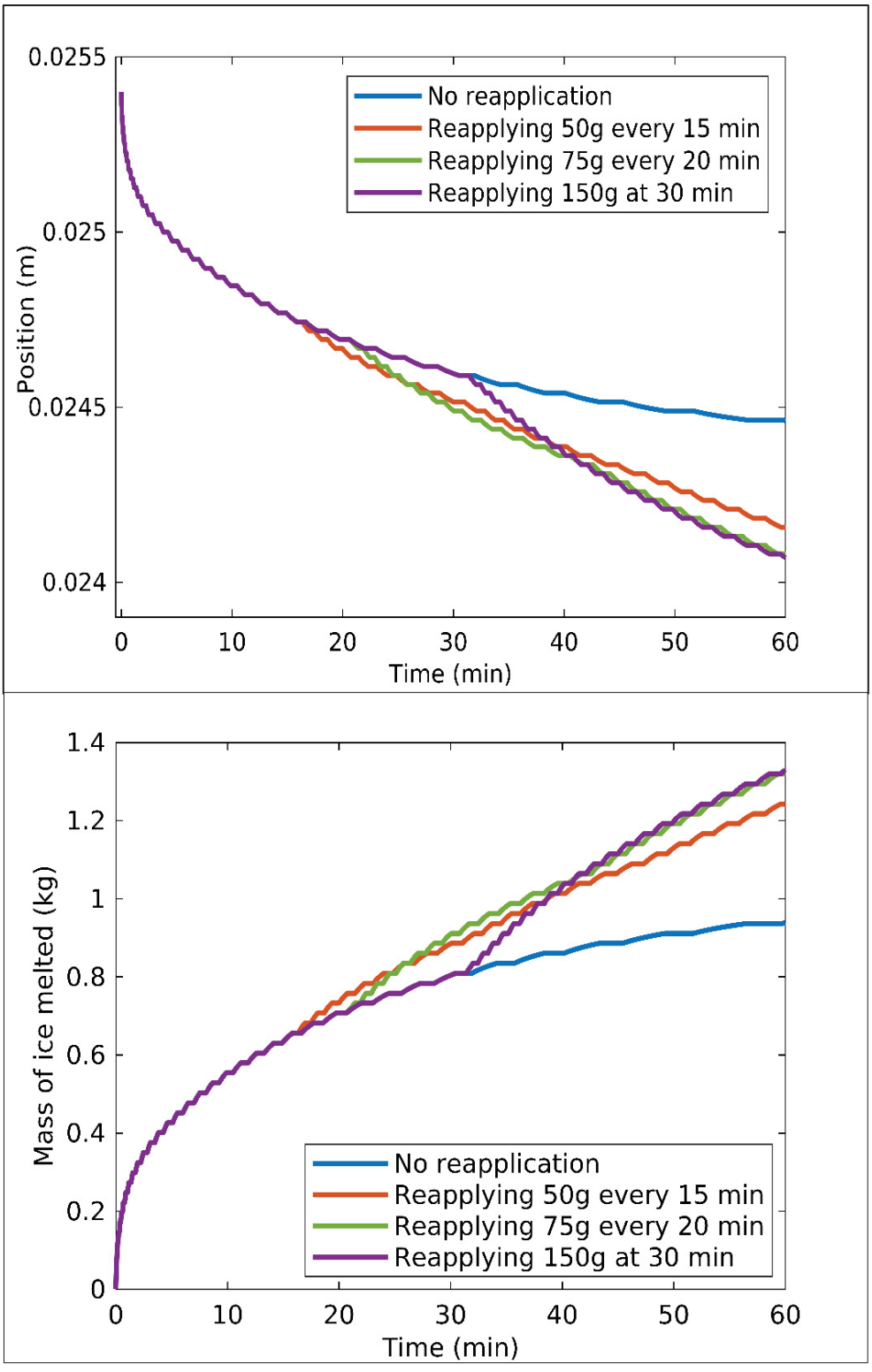


Figure 3.40 (a) Melting front location and (b) mass of ice melted over 60 minutes under different reapplication scenarios

The results for the mass of ice melted and the melting front location indicate that reapplying the full amount of 150g deicer at once or reapplying 75g twice cause more mass of ice melted than dividing it into smaller portions. By the 60-minute mark, both scenarios 1 and 2 result in the same amount of ice melted—1.33 kg. By the end of 60 minutes, scenarios 1 and 2 show a small difference compared to Scenario 3, with approximately 0.1 mm (equivalent to 80 grams) more ice melted.

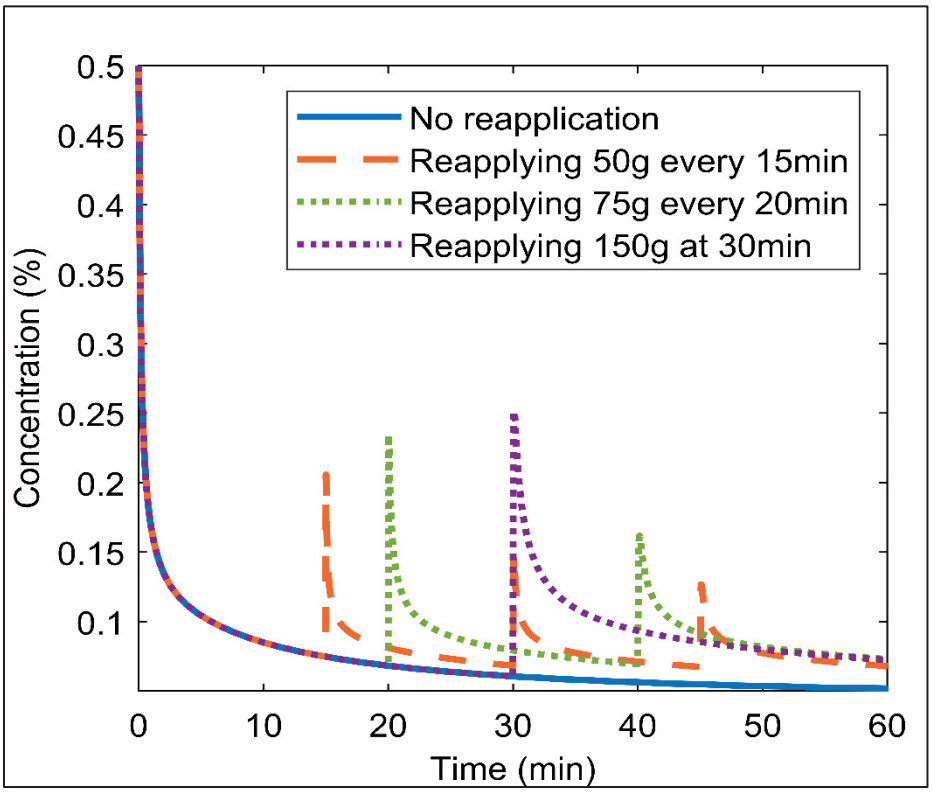


Figure 3.41 Concentration of the surface over 60 minutes
under different reapplication scenarios

Figures 3.42a and 3.42b depict the surface temperature and melting temperature over 60 minutes for the three deicer reapplication scenarios, along with the scenario without reapplication. The blue line represents the scenario without reapplication, while the purple, green, and orange lines correspond to scenarios 1, 2, and 3, respectively. As shown, the melting temperature of the system decreases when deicer is reapplied, depending on its concentration (as seen in Figure 3.41). This leads to a corresponding drop in surface temperature. In scenario

1, where the deicing solution is added all at once, the melting temperature immediately drops to -20°C, reflecting a 25% concentration. This causes the surface temperature to decrease by about 2°C.

In this figure, the initial temperature corresponds to the control volume at the surface of the deicing solution before reapplication. After reapplying 150 grams of deicing solution (at a temperature of -2°C), additional control volumes are introduced into the system due to the added solution. As a result, the surface control volume changes. However, to maintain consistency in our analysis, we continue to monitor the temperature of the original surface control volume from before the reapplication, rather than the updated surface control volume after reapplication. In the end, there is no significant difference in surface temperature across all scenarios, with the temperature stabilizing around -3°C. This is because, by the end, the concentration within the control volume is approximately the same in all cases.

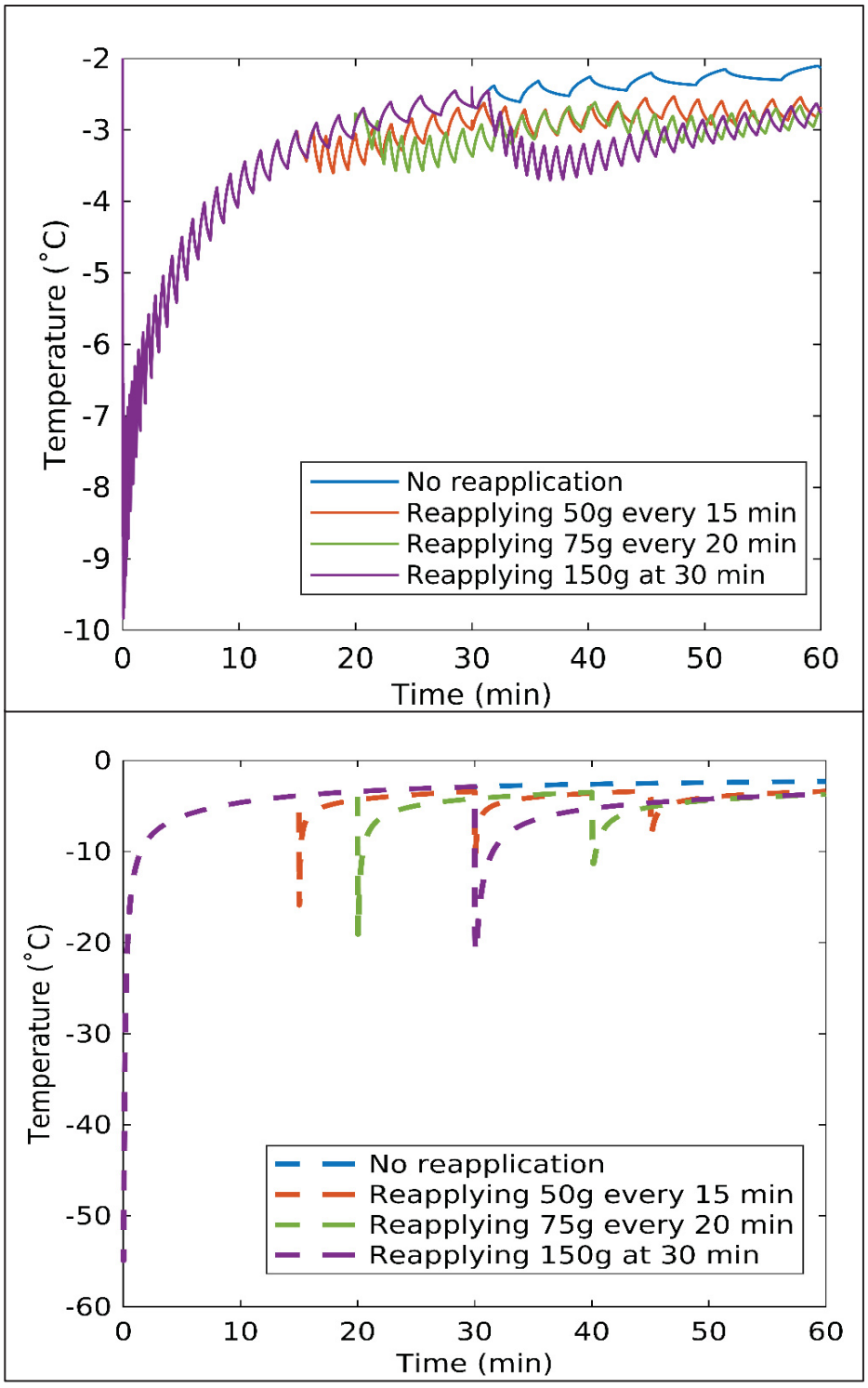


Figure 3.42 (a) Surface temperature (b) Melting temperature over 60 minutes under different reapplication scenarios

## 3.5 Conclusion & Discussion

This chapter presented the results of the runway deicing model. The model was first verified against the Neumann similarity solution using a test case without the presence of deicing chemicals. The results showed good agreement with the Neumann solution. In the second phase of verification, an experimental test case with KFO as the deicing agent was used, and key parameters were analyzed. The relationship between surface temperature and melting temperature was examined, confirming an initial rapid surface temperature drop due to ice melting, followed by a subsequent rise in melting temperature. Additionally, the location of the melting front was tracked, showing that ice melting occurred at a faster rate before the system reached thermal equilibrium.

We also monitored the concentration of the deicing solution, confirming a gradual decrease over time due to dilution from the melted ice. Analysis of the mass of ice melted showed that the highest melting rate occurred before reaching equilibrium, with a slower rate afterward.
To ensure the accurate incorporation of mass transfer terms into the enthalpy method, we calculated the mass of water and solute in each control volume using concentrations derived from Fick's law. We also calculated solute concentrations based on the interface location within each control volume. The results for both the mass of ice melted and the solute concentration, obtained using both methods—one based on the interface location and the other from Fick's law—are in close agreement. It verifies that the mass transfer process has been correctly implemented in the enthalpy method. The calculation of the ice mass and solute concentration in both approaches confirms that the coupling of heat and mass transfer processes has been successfully implemented.

To further investigate concentration dynamics, data for specific control volumes were presented. The relationship between concentration and melting temperature was examined, verifying that the system followed the liquidus curve as described in the methodology. This analysis emphasized the role of concentration gradients in diffusion processes within the domain, which significantly impact the spatial and temporal evolution of melting.

We also analyzed the enthalpy (internal energy) in a control volume, which confirmed that during the melting process, internal energy increased rapidly due to latent heat absorption at the melting temperature. Finally, a comparison of enthalpy between three control volumes—one initially liquid and the others initially solid—demonstrated that enthalpy remains relatively constant in regions without phase change. However, in regions undergoing melting, enthalpy increases significantly due to latent heat absorption. These findings reinforce the localized nature of phase change and its dependence on both thermal and concentration gradients in the model.

The mesh sensitivity study evaluated the impact of mesh size on numerical method, specifically assessing grid-induced errors for temperature and mass of ice melted results. Minimal variation was observed between the 250-node and 1000-node meshes, with differences of less than 0.1°C and 0.1g. The staircase phenomenon was reduced with finer meshes, resulting in smoother results and decreased duration of the staircase effect. Thus, while M=500 provided reasonable accuracy, M=1000 was selected for validation to further mitigate the staircase effect, as it required approximately 24 hours of simulation time, which is manageable.

In the validation section, two different temperature conditions were tested for both KFO and KAC. The first condition was at -2°C, and the second at -10°C. In Condition 1, the maximum temperature error was found to be 0.9% for KFO and 0.88% for KAC, occurring at the 10- and 30-minute marks, respectively. Despite this, when the standard deviation of the thermal camera was considered, the modeled temperatures were closely aligned with the experimental data. For mass, the highest error occurred at the 5-minute mark, with 15% for KFO and 11% for KAC. The concentration results for both deicers agreed well with experimental values, with concentrations stabilizing around 0.15 after 30 minutes. Like the mass results, the largest concentration errors were observed at 5 minutes.

Under Condition 2 (-10°C), the temperature error peaked at 1.2% for both deicers, while the mass error reached 11.8% for KFO and 16% for KAC. The concentration error followed the same trend as mass, with the highest error occurring at the 5-minute point.

The validation of our numerical model was conducted using small-scale laboratory tests in a Petri dish due to the unavailability of experimental data for real runways. We believe this validation is sufficient to demonstrate the model's applicability to full-scale runway scenarios for the following reasons:

- Dominance of vertical direction in de-Icing physics:
  The deicing process is primarily driven by the diffusion of the deicer in the vertical direction through the deicer and ice layers, with negligible influence from lateral dimensions. This one-dimensional nature ensures that the critical phenomena observed in small-scale Petri dish tests are representative of full-scale systems. Since vertical diffusion is decoupled from lateral dimensions, the model is inherently scalable, and its predictions remain valid regardless of the system's size, supporting its applicability to real runway scenarios.
- Consistency of material properties:
  The thermal and physical properties of the deicer and ice (e.g., thermal conductivity, specific heat, diffusion coefficients, temperature of ice, deicer and ambient) remain consistent across scales, ensuring that the model’s predictions are transferable from the small-scale system to a full-scale runway.

Indeed, the Petri dish experiments serve as a proof of concept, demonstrating the model's ability to predict phase transitions and melting processes under controlled conditions. The experimental data validates that the enthalpy-based approach and the concentration-dependent freezing point are representations of the underlying melting dynamic.

When analyzing the heat convection coefficient, it was observed that increasing the heat convection coefficient leads to a rise in surface temperature. This increase impacts both the minimum temperature and the post-equilibrium temperature. A higher heat convection

coefficient results in more heat reaching the system at the interface, which accelerates the ice melting process. After the system reaches equilibrium, the heat convection coefficient continues to play a key role in determining the total mass of ice melted. This parametric study was conducted because the heat convection coefficient was identified as a potential source of error during validation. Since the heat loss by convection was not directly measured in the experiments, this analysis helps quantify the model's sensitivity to this parameter and its potential impact on the predictive accuracy of the model.

Regarding the initial solution thickness, the results showed that increasing the thickness of the deicing solution enhances ice melting while lowering the surface temperature. We calculated the change in melted ice mass per unit increase in deicing solution thickness $\Delta m_{melted\ ice} / \Delta H_{initial}$. From 5g to 7g (with thickness change from $2.06 \times 10^{-4}\ m$ to $2.88 \times 10^{-4}\ m$), the rate is approximately $18.29\ g/m$. From 7g to 10g (thickness change from $2.88 \times 10^{-4}\ m$ to $4.11 \times 10^{-4}\ m$), the rate is approximately $16.26\ g/m$. This parameter was selected for study because the non-uniform distribution of the deicing solution during experiments was identified as another source of error in the validation process. By examining how variations in initial thickness affect melting dynamics, this analysis helps quantify the model's sensitivity to this parameter.

In the study on melting temperature, both constant (eutectic or equilibrium) and variable melting temperatures were considered. This parametric study was conducted to highlight the sensitivity of the model to melting temperature and its critical role in predicting both the melting rate and surface temperature. Unlike previous studies that indirectly account for melting temperature through empirical melting rates and concentration estimates, this model incorporates melting temperature directly into the thermal calculations. By analyzing scenarios with both constant and variable melting temperatures, the study demonstrates how concentration-dependent melting temperatures provide a more realistic representation of the deicing process. The results revealed that using a constant melting temperature throughout the process yields a higher melting rate overall. The surface temperature is closely tied to the

melting temperature, with a constant melting point resulting in a rapid decrease in temperature until it reaches the specified melting value.

The parametric studies on the heat convection coefficient, deicing solution thickness, and melting temperature reveal the significant influence of these parameters on the deicing process. Increasing the heat convection coefficient enhances heat transfer to the system, leading to faster equilibrium times, higher surface temperatures, and an increase in the total mass of ice melted. Similarly, increasing the deicing solution thickness facilitates ice melting by maintaining higher solution concentrations for longer periods, slowing dilution, and extending the duration of melting. The melting temperature also plays a critical role, as it directly impacts both the melting rate and surface temperature. Using a concentration-dependent melting temperature provides a more realistic representation of the deicing process, while a constant melting temperature results in higher overall melting rates due to the sustained concentration of the solution.

While each parameter contributes uniquely to the deicing dynamics, the heat convection coefficient directly affects the rate of heat input at the boundary, the deicing solution thickness governs concentration-dependent melting, and the melting temperature determines the thermal behavior. Together, these studies highlight the model's sensitivity to these parameters and their collective importance in accurately simulating the deicing process.

The final section compared the melting rates of KAC and KFO under runway conditions. KAC exhibited a higher melting rate than KFO in both temperature scenarios. However, based on the amount of deicer recommended by literature, complete ice melting did not occur, indicating that larger quantities of deicer would be necessary for full ice melting. Additionally, the model does not account for certain physical processes, such as the penetration of deicing solution into fractured ice. This could affect the distribution of concentration and, subsequently, the melting dynamics.

Lastly, the study explored the impact of deicer reapplication frequency on both ice thickness and surface temperature. Three scenarios were tested: (1) reapplying 150 g/m² of solution at t=30 minutes, (2) reapplying 75 g/m² every 20 minutes (at t=20 and t=40 minutes), and (3) reapplying 50 g/m² every 15 minutes (at t=15, t=30, and t=45 minutes). The scenario without reapplication serves as a baseline for comparison, where the mass of ice melted is notably lower than in the reapplication scenarios. Results for the mass of ice melted and melting front location indicate that reapplying the full 150 g of deicer at once, or reapplying 75 g twice, yields more ice melted than dividing it into smaller portions. By the 60-minute mark, both scenarios 1 and 2 result in 1.33 kg of ice melted. By the end of the 60 minutes, scenarios 1 and 2 show only a minor difference compared to scenario 3, with approximately 0.1 mm (about 80 grams) more ice melted. There is minimal variation in surface temperature across all reapplication scenarios, as the temperature stabilizes around -3°C. This consistency is due to the similar concentration levels within the control volume by the end of each scenario.

This thesis contributes to advancing runway deicing strategies, offering insights that align with sustainability goals by reducing the use of deicing chemicals. By predicting melting rates and the behavior of deicing agents under varying atmospheric and runway conditions, the developed model helps to minimize the environmental impact of runway deicing operations. Specifically, understanding the melting behavior of different deicing materials, such as Potassium acetate (KAC) and Potassium formate (KFO), and the influence of temperature, concentration, and reapplication frequency provides valuable data for reducing the quantity of chemicals required for deicing. This directly supports sustainability efforts by minimizing chemical usage, which is crucial for reducing environmental pollution and the negative impact of runoff on surrounding.

The study’s results also provide insights for airport operators, particularly in optimizing deicing operations. By incorporating the eutectic temperature of deicing materials into the model, airport management can better predict the effectiveness of various deicers and make informed decisions about which chemicals to use based on specific runway conditions. The model's ability to simulate different deicing scenarios allows for tailored strategies that balance

performance and environmental responsibility, and contributing to safer, more sustainable runway management practices.

The key contributions of this work are:

- Dynamic and coupled modeling:
  Unlike previous studies that rely on experimental measurements of bulk properties, such as volume and mass, this model dynamically couples heat transfer, mass transfer, and phase change processes. This coupling enables a detailed understanding of how melting is influenced by both thermal and concentration gradients.
- Spatial solution:
  The use of a one-dimensional finite-volume approach provides spatially resolved insights into the evolution of melting front locations and phase distributions, offering a more realistic compared to uniform assumptions made in experimental methods.

- Diffusion and concentration gradients:
  The inclusion of diffusion effects, driven by deicer concentration gradients, represents a critical improvement. This aspect was largely ignored in earlier approaches but is shown to play a significant role in the melting rate and temperature evolution.

- Phase tracking:
  Through the enthalpy-based method, this model tracks the phase of control volumes (solid, liquid, or mushy) at every time step.

- Predictive capability:
  The model is not only validated against experimental results but also offers predictive capabilities for various scenarios. It can simulate the effects of different deicer types, concentrations, and environmental conditions.

- Improved representation of melting rate and temperature:

The melting rate in this model is computed as a direct outcome of the coupled heat and mass transfer processes, rather than being inferred from bulk measurements. Similarly, the melting temperature is dynamically updated based on local conditions, ensuring consistency with physical principles and experimental freezing point-concentration data.

Several important improvements have been identified in the proposed model, particularly in terms of its ability to simulate a more realistic deicing process. One of the key enhancements is the incorporation of mass diffusion, which plays a critical role in the melting process. Diffusion is especially significant during the early stages of deicing, before the system reaches its equilibrium temperature. After equilibrium is reached, the temperatures in both the solid and liquid phases become nearly identical, making the results from the 1D model nearly equivalent to those of the previous models. However, it is the consideration of diffusion in the initial stage of the process that results in a more accurate simulation of melting dynamics, unlike the previous models, which assume uniform concentration and temperature across the system.

Another key improvement is the method used for calculating the melting rate. Unlike the previous models, which require experimental data for the melting rate of each deicer, our model calculates the melting rate directly from the calculation. It only requires the eutectic temperature, the density and the specific heat of the deicing solution, which are obtained from experimental data. This approach eliminates the need for experimental tests for each new deicer, offering a more generalizable and cost-effective solution. This is an important advancement because it allows for the simulation of deicing processes for different chemicals without the need for additional empirical data.

Furthermore, our model introduces the capability to simulate deicer reapplication, a feature not present in the previous models. The previous models assume uniform concentration and temperature across the system, making them unsuitable for evaluating the impact of reapplying deicers in real-world conditions. In contrast, our model can dynamically account for changes

in concentration and temperature throughout the deicing process, providing actionable insights for optimizing deicing operations and reducing environmental impact.

These improvements contribute to a more accurate and flexible model that provides better insights into the deicing process. By incorporating diffusion, calculating melting rates directly from deicer properties, and allowing for the reapplication of deicers, our model represents a significant advancement over the previous models. These enhancements make the model more realistic and applicable to a broader range of deicing operations, offering a numerical tool complementary to laboratory experiments for improving runway deicing strategies in practice.

# CONCLUSION

This thesis aimed to develop a numerical model for the runway deicing process that predicts ice melting rates and surface temperatures under varying deicer and atmospheric conditions. Existing deicing models for the pavements often rely on empirical melting rates and zero-dimensional analysis, which inadequately capture the complexities of runway-specific conditions. To address these limitations, this work developed a spatially resolved deicing model based on the modified Stefan problem, incorporating mass diffusion and concentration-dependent melting temperatures. The model uses the enthalpy method, enabling flexible treatment of phase changes in impure solutions, and provides detailed predictions of deicing performance under realistic conditions.

Achievements of the three sub-objectives:

1. The first objective was to identify the most suitable mathematical and numerical methods for addressing the phase change problem. This was achieved by employing the enthalpy method to solve the Stefan problem alongside a finite volume approach for spatial solution and finite difference approximations for temporal derivatives. The model incorporated Fick's law of diffusion to address the non-uniform distribution of deicer concentration during melting, capturing critical concentration gradients at the melting front location and their influence on melting dynamics.

   A mesh sensitivity study was conducted. Results demonstrated the model's predictions for surface temperature and total ice mass melted for number of meshes 250, 500, and 1000. The differences between the 250-node and 1000-node meshes were less than 0.1°C in temperature and below 0.1 g in mass of ice melted. Finer meshes reduced the staircase phenomenon, leading to smoother outputs and a shorter duration of the effect. Although the 500-node mesh provided adequate accuracy, the 1000-node mesh was selected for validation to further reduce the staircase effect, with a simulation time of approximately 24 hours.

The analysis of key parameters, including surface temperature, melting front location, and concentration gradients, verified the model's ability to capture the interactions between heat flow, mass diffusion, and phase change processes. The parametric trends followed physical expectations, such as the adherence to the liquidus curve and proper mass transfer behavior as governed by Fick's law. These elements collectively verified the model's suitability for pavement deicing applications.

2. The second objective was to develop a melting model that incorporates the influence of deicer agents and validate it against experimental data. The model was applied to KAC and KFO under controlled experimental conditions at -2°C and -10°C. Validation results demonstrated that the model predicted surface temperatures, ice melting rates, and deicer concentrations. Three parametric study was done:

   Heat convection coefficient: Increasing the heat convection coefficient enhanced the rate of heat transfer at the melting front location, leading to faster melting rates and increased total ice melting. This study also helped quantify the potential uncertainties arising from variations in heat convection in the experimental setup.

   Deicing solution thickness: The study showed that increasing the initial deicing solution thickness improved ice melting rates. Quantifying the melting rate as a function of deicing solution thickness provided insights into potential experimental errors caused by non-uniform deicing solution distribution.

   These parametric studies were critical for understanding how variations in key parameters could affect experimental results, explaining some of the discrepancies observed during model validation.

   Effect of the melting temperature as a function of concentration: Simulations revealed that using a constant melting temperature accelerated melting compared to variable melting temperatures, highlighting the importance of accounting for concentration-

dependent melting temperatures in real scenarios. This parametric study was conducted to highlight the sensitivity of the model to melting temperature and its critical role in predicting both the melting rate and surface temperature. Unlike previous studies that indirectly account for melting temperature through empirical melting rates and concentration estimates, this model incorporates melting temperature directly into the thermal calculations.

3. The third objective focused on applying runway-specific conditions and studying operational scenarios. Two critical aspects were examined:

   Performance evaluation of KAC and KFO deicers: Under runway conditions, KAC exhibited higher melting rates than KFO at both -2°C and -10°C. However, neither deicer achieved complete ice melting within the recommended application rates, suggesting that larger quantities or multiple applications are necessary for full deicing. These findings emphasize the model's utility in optimizing deicer choice and application strategies for different environmental conditions. However, the amount of deicer suggested in the literature was insufficient to achieve complete ice melting, indicating that greater quantities would be required for full ice melting. Moreover, the model does not consider specific physical processes, such as the penetration of deicing solution into fractured ice, which could influence the concentration distribution and, consequently, the melting behavior.

   Impact of deicer reapplication frequency on ice melting and surface temperature on Runways: Three reapplication scenarios were tested, (1) a single 150 g/m² reapplication at 30 minutes, (2) 75 g/m² reapplications at 20- and 40-minute intervals, and (3) 50 g/m² reapplications every 15 minutes. Results showed that larger, less frequent applications melted more ice overall, with scenarios (1) and (2) achieving approximately 1.33 kg of melted ice by 60 minutes, while scenario (3) resulted in slightly less melting.

The key contributions are:

- Innovative Modeling Approach:
  The thesis extends the Stefan problem and enthalpy by incorporating variable melting temperatures and mass diffusion, significantly advancing the theoretical understanding of deicing processes. The melting rate in this model is computed as an outcome of the coupled heat and mass transfer processes. This allows for modeling of non-uniform deicer concentrations and their impact on melting dynamics.

- Practical Validation:
  The model was validated against experimental data under controlled conditions, demonstrating its accuracy in predicting temperature, concentration, and melting rates for commonly used deicers (KAC and KFO).

- Runway-Specific Insights:
  The model provides actionable insights for deicer application strategies, highlighting the importance of reapplication frequency in maximizing melting rate and improving operational safety.

## RECOMMENDATIONS & LIMITATIONS

1. Limitations

- Simplified geometry:
  The current model assumes a one-dimensional geometry for computational simplicity. While this provides insights into deicing processes, it does not fully capture the complexities of real-world runway surfaces, such as cracks, slopes, or uneven ice layers.

- Absence of deicer penetration into ice:
  The model does not consider the penetration of deicing solution into the ice, which may occur in porous or fractured ice. This could affect the distribution of concentration and, subsequently, the melting dynamics.

- Exclusion of environmental interactions:
  External factors such as solar radiation, sublimation and evaporation, and rain are neglected. These factors could influence the melting rate and heat flux distribution, particularly in outdoor applications.

2. Suggestions for future work

- Extension to multi-dimensional models:
  Developing two- or three-dimensional models would enhance the understanding of deicing processes on complex geometries, and able to model non-uniform thickness and crack.

- Integration of deicer penetration:
  Taking into account for deicer penetration into ice or porous substrates could provide more accurate predictions for field applications.

- Incorporation of environmental effects:
  Future work should include external influences like solar radiation, sublimation and evaporation, and rain to improve the model's applicability to real-world conditions.

- Validation with field data:
  While the model has been validated with controlled experimental data, further validation using field measurements on actual runways is suggested to ensure its robustness and scalability.

- Applying the model to other transportation infrastructures, such as roads or bridges.

## APPENDIX

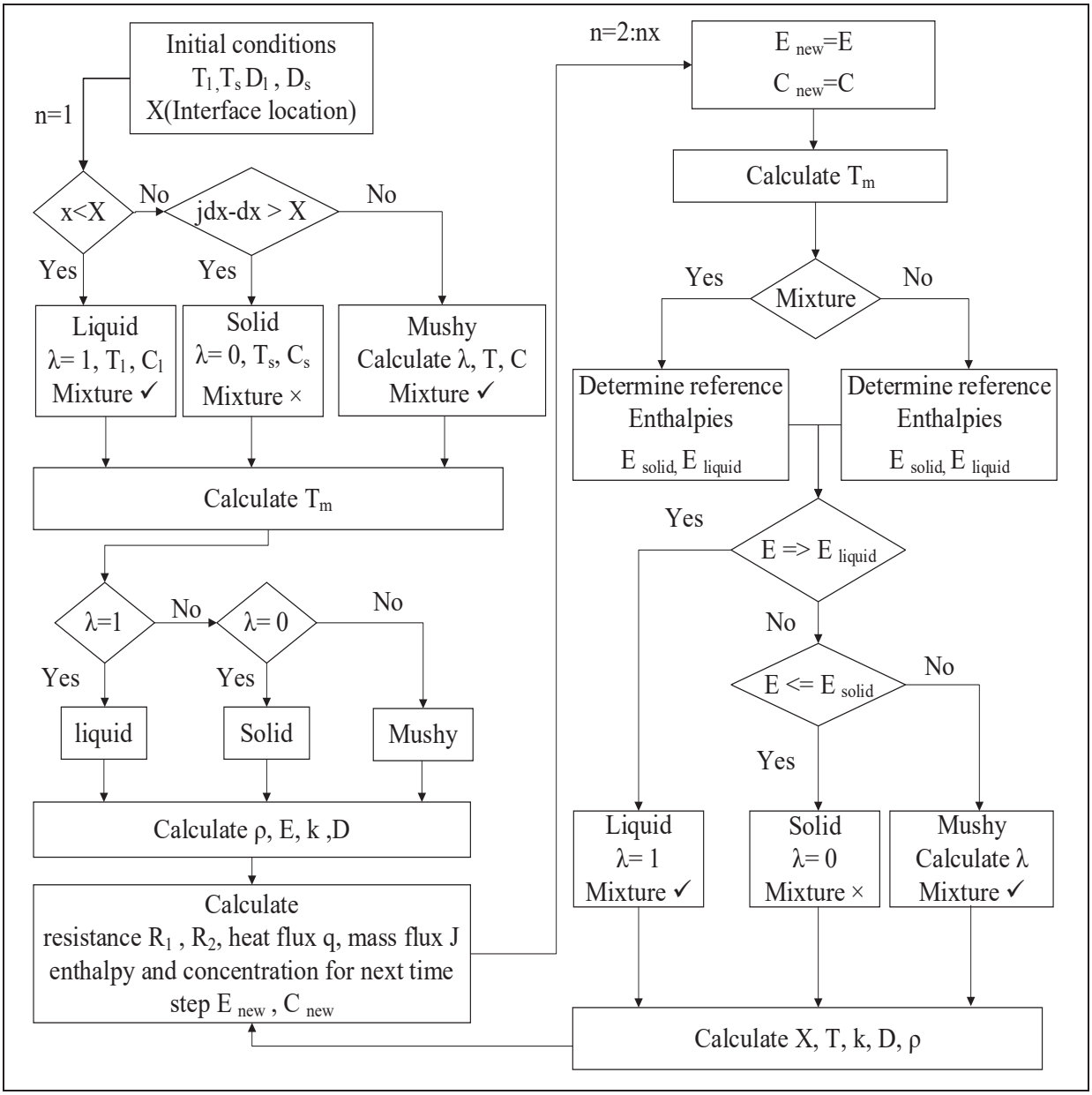


The calculation algorithm of runway deicing model

## BIBLIOGRAPHY


Akin, M., & Shi, X. (2012). Development of standard laboratory testing procedures to evaluate the performance of deicers. *Journal of Testing and Evaluation, 40*(6), 1015-1026.

Alexiades, V., & Solomon, A. D. (1993). *Mathematical modeling of melting and freezing processes*: Routledge.

Associated-Press. (2015). United Airlines plane slides off runway at O'Hare Airport. Retrieved from https://abc7chicago.com/plane-off-runway-ohare-slides-chicago-airport/1140653/

Association-québécoise-des-transports, A. (2011). Pleins feux sur l'expertise de classe internationale d'Aéroports de Montréal en matière de déneigement. Retrieved from https://aqtr.com/association/actualites/pleins-feux-lexpertise-classe-internationale-daeroports-montreal-matiere-deneigement

Ayasoufi, A. (2004). *Numerical Simulation of Heat Conduction with Melting and/or Freezing by Space-Time Conservation Element and Solution Element Method.* University of Toledo, Retrieved from http://rave.ohiolink.edu/etdc/view?acc_num=toledo1103147485

Barash, S., Covington, J., & Tamulonis, C. (2000). Preliminary data summary airport deicing operations (Revised). *United States Environmental Protection Agency, Washington*.

Beckett, G., Mackenzie, J. A., & Robertson, M. L. (2001). A Moving Mesh Finite Element Method for the Solution of Two-Dimensional Stefan Problems. *Journal of Computational Physics, 168*(2), 500-518. doi:https://doi.org/10.1006/jcph.2001.6721

Bennon, W. D., & Incropera, F. P. (1987). A continuum model for momentum, heat and species transport in binary solid-liquid phase change systems—I. Model formulation. *International Journal of Heat and Mass Transfer, 30*(10), 2161-2170. doi:https://doi.org/10.1016/0017-9310(87)90094-9

Bhattacharya, M., Basak, T., & Ayappa, K. G. (2002). A fixed-grid finite element based enthalpy formulation for generalized phase change problems: role of superficial mushy region. *International Journal of Heat and Mass Transfer, 45*(24), 4881-4898. doi:https://doi.org/10.1016/S0017-9310(02)00178-3

Blackburn, R. R., Amsler, D., & Bauer, K. M. (2004). Guidelines for snow and ice control materials and methods. *Transportation Research Circular*, 31-49.

Brassard, J.-D., Laforte, C., Tremblay, M. M., & Volat, C. (2019). *Runway Deicing Product Anti/Deicing Performance Assessment: Review and Future Directions*. https://doi.org/10.4271/2019-01-1974

CBS-news. (2016). United Flight From SFO Skids Off Runway In Chicago. Retrieved from https://www.cbsnews.com/sanfrancisco/news/united-flight-from-sfo-skids-off-runway-in-chicago/#:~:text=CHICAGO%20(CBS%20SF)%20%2D%2D%20A,if%20weather%20played%20a%20role.

Chappelow, C. C., McElroy, A. D., Blackburn, R. R., Darwin, D., de Noyelles, F. G., & Locke Jr, C. E. (1992). *Handbook of test methods for evaluating chemical deicers*. Retrieved from

Charpentier, C., Brassard, J.-D., Momen, G., & Perron, J. (2023). Development of a dynamic ice penetration model for runway de-icing products through performance experimental characterization. *Cold Regions Science and Technology, 213*, 103932. doi:https://doi.org/10.1016/j.coldregions.2023.103932

Charpentier, C., Brassard, J.-D., Tremblay, M.-M., & Momen, G. (2022). *A Refined Procedure for Evaluating the Airport Runway De-icing Products Performance*. Paper presented at the Workshop on Atmospheric Icing of Structures.

Comfort, G. (2001). *Wet Runway Friction : Literature and Information Review*: Transportation Development Centre.

Committee, G.-R. D. P. (2021). Ice Melting Test Method for AMS1431 and AMS1435 Runway Deicing/Anti-Icing Products. In: SAE International.

Cryotech-Deicing-Technology. Liquid Runway Deicer. Retrieved from https://www.cryotech.com/products/e36-liquid-runway-deicer

Dan, H.-C., Tan, J.-W., Du, Y.-F., & Cai, J.-M. (2020). Simulation and optimization of road deicing salt usage based on Water-Ice-Salt Model. *Cold Regions Science and Technology, 169*, 102917. doi:https://doi.org/10.1016/j.coldregions.2019.102917

Denby, B. R., Sundvor, I., Johansson, C., Pirjola, L., Ketzel, M., Norman, M., . . . Omstedt, G. (2013). A coupled road dust and surface moisture model to predict non-exhaust road traffic induced particle emissions (NORTRIP). Part 2: Surface moisture and salt impact modelling. *Atmospheric Environment, 81*, 485-503. doi:https://doi.org/10.1016/j.atmosenv.2013.09.003

Dusinberre, G. (1945). Numerical methods for transient heat flow. *Transactions of the American Society of Mechanical Engineers, 67*(8), 703-710.

Esen, A., & Kutluay, S. (2004). A numerical solution of the Stefan problem with a Neumann-type boundary condition by enthalpy method. *Applied Mathematics and Computation, 148*(2), 321-329. doi:https://doi.org/10.1016/S0096-3003(02)00846-9

Evans, J. D., & King, J. R. (2000). Asymptotic results for the Stefan problem with kinetic undercooling. *The Quarterly Journal of Mechanics and Applied Mathematics, 53*(3), 449-473. doi:10.1093/qjmam/53.3.449

Eyres, N. R., Hartree, D. R., Ingham, J., Sarjant, R. J., & Wagstaff, J. B. (1946). The calculation of variable heat flow in solids. *Philosophical Transactions of the Royal Society of London. Series A, Mathematical and Physical Sciences, 240*(813), 1-57. doi:doi:10.1098/rsta.1946.0002

Font, F., & Myers, T. G. (2013). Spherically symmetric nanoparticle melting with a variable phase change temperature. *Journal of Nanoparticle Research, 15*(12), 2086. doi:10.1007/s11051-013-2086-3

Fujimoto, A., Tokunaga, R. A., Kiriishi, M., Kawabata, Y., Takahashi, N., Ishida, T., & Fukuhara, T. (2014). A road surface freezing model using heat, water and salt balance and its validation by field experiments. *Cold Regions Science and Technology, 106-107*, 1-10. doi:https://doi.org/10.1016/j.coldregions.2014.06.001

Gerbino-Bevins, B., Tuan, C., & Mattison, M. (2012). Evaluation of Ice-Melting Capacities of Deicing Chemicals. *Journal of Testing and Evaluation, 40*(6), 952-960. doi:10.1520/JTE104460

Groot, R. D. (2018). Second order front tracking algorithm for Stefan problem on a regular grid. *Journal of Computational Physics, 372*, 956-971. doi:https://doi.org/10.1016/j.jcp.2018.04.051

Gudibande, N., & Iyer, K. (2013). Modified enthalpy method for the simulation of melting and solidification. *Sadhana, 38*(6), 1259-1285. doi:10.1007/s12046-013-0210-9

Gudibande, N., & Iyer, K. (2017). Numerical simulation of contact melting using the cell-splitting modified enthalpy method. *Numerical Heat Transfer, Part B: Fundamentals, 71*(1), 84-107. doi:10.1080/10407790.2016.1244396

Gupta, S. C. (2017). *The classical Stefan problem: basic concepts, modelling and analysis with quasi-analytical solutions and methods* (Vol. 45): Elsevier.

Hassan, Y., Halim, A. O. A. E., Razaqpur, A. G., Bekheet, W., & Farha, M. H. (2002). Effects of Runway Deicers on Pavement Materials and Mixes: Comparison with Road Salt. *Journal of Transportation Engineering, 128*(4), 385-391. doi:doi:10.1061/(ASCE)0733-947X(2002)128:4(385)

Henry, H., & Stavros, A. A. (1996). Mathematical modelling of solidification and melting: a review. *Modelling and Simulation in Materials Science and Engineering, 4*(4), 371. doi:10.1088/0965-0393/4/4/004

Jamil, A., Kousksou, T., Zeraouli, Y., Gibout, S., & Dumas, J. P. (2006). Simulation of the thermal transfer during an eutectic melting of a binary solution. *Thermochimica Acta, 441*(1), 30-34. doi:https://doi.org/10.1016/j.tca.2005.11.010

Klein-Paste, A. (2007). Runway Operability under Cold Weather Conditions. Tire-pavement friction creation by sand particles on iced pavements, and non-contacting detection of sand particles on pavements.

Klein-Paste, A. (2018). Airplane braking friction on dry snow, wet snow or slush contaminated runways. *Cold Regions Science and Technology, 150*, 70-74.

Klein-Paste, A., & Potapova, J. (2014). Thermal Aspects of Melting Ice with Deicer Chemicals. *Transportation Research Record, 2440*(1), 69-75. doi:10.3141/2440-09

Koga, S., & Krstic, M. (2020). Single-boundary control of the two-phase Stefan system. *Systems & Control Letters, 135*, 104573. doi:https://doi.org/10.1016/j.sysconle.2019.104573

König-Haagen, A., & Diarce, G. (2023). Comparison of Corrected and Uncorrected Enthalpy Methods for Solving Conduction-Driven Solid/Liquid Phase Change Problems. *Energies, 16*(1), 449. Retrieved from https://www.mdpi.com/1996-1073/16/1/449

Kulyakthin, S., & Klein-Paste, A. (2021). Can calorimetry be used to measure the melting rate of deicers? *Cold Regions Science and Technology, 181*, 103170. doi:https://doi.org/10.1016/j.coldregions.2020.103170

Lamas, C. P., Vega, C., & Noya, E. G. (2022). Freezing point depression of salt aqueous solutions using the Madrid-2019 model. *The Journal of Chemical Physics, 156*(13). doi:10.1063/5.0085051

Lamé, G., & Clapeyron, B. (1831). *Mémoire sur la solidification par refroidissement d'un globe liquide.* Paper presented at the Annales Chimie Physique.

Melinder, Å. (2007). Thermophysical Properties of Aqueous Solutions Used as Secondary Working Fluids Doctoral Thesis By.

Monteiro, E., Almeida, R., & Rouboa, A. (2011). Finite Volume Method Analysis of Heat Transfer in Multiblock Grid during Solidification. In.

Myers, T. G. (2016). Mathematical modelling of phase change at the nanoscale. *International Communications in Heat and Mass Transfer, 76*, 59-62. doi:https://doi.org/10.1016/j.icheatmasstransfer.2016.05.005

Myers, T. G., & Font, F. (2015). On the one-phase reduction of the Stefan problem with a variable phase change temperature. *International Communications in Heat and Mass Transfer, 61*, 37-41. doi:https://doi.org/10.1016/j.icheatmasstransfer.2014.11.008

Myers, T. G., Hennessy, M. G., & Calvo-Schwarzwälder, M. (2020). The Stefan problem with variable thermophysical properties and phase change temperature. *International Journal of Heat and Mass Transfer, 149*, 118975. doi:https://doi.org/10.1016/j.ijheatmasstransfer.2019.118975

National-Transportation-Safety-Board. (2016). *Runway Excursion During Landing, Delta Air Lines Flight 1086, Boeing MD-88,N909DL, New York, New York March 5,2015*. Retrieved from https://www.ntsb.gov/investigations/AccidentReports/Reports/AAR1602.pdf

Nuijten, A. D. W. (2016). Runway temperature prediction, a case study for Oslo Airport, Norway. *Cold Regions Science and Technology, 125*, 72-84. doi:https://doi.org/10.1016/j.coldregions.2016.02.004

Optris-GmbH-team. *TECHNICAL NOTE - FEVER SCREENING SYSTEMS*. Retrieved from https://www.instrumart.com/assets/technical-note-fever-screening.pdf

Peters-chemical-company. E36 LIQUID RUNWAY DEICER – SAFE RUNWAYS AND A CLEAN ENVIRONMENT. Retrieved from https://www.peterschemical.com/e36-liquid-runway-deicer/

Potapova, J. (2012). *Melting ice with salt-a thermodynamic model.* Institutt for bygg, anlegg og transport,

Prakash, C., & Voller, V. (1989). On the numerical solution of continuum mixture model equations describing binary solid-liquid phase change. *Numerical Heat Transfer, Part B: Fundamentals, 15*(2), 171-189. doi:10.1080/10407798908944899

Problem, S., & Vuik, C. (1994). Some historical notes about the Stefan problem.

Radio-Canada. (2019). Un avion fait une sortie de piste à l'aéroport de Bagotville. Retrieved from https://ici.radio-canada.ca/nouvelle/1151839/incident-voyageurs-bagotville-aeroport-urgence

Roscani, S. D., & Voller, V. R. (2024). On an enthalpy formulation for a sharp-interface memory-flux Stefan problem. *Chaos, Solitons & Fractals, 181*, 114679. doi:https://doi.org/10.1016/j.chaos.2024.114679

Rubinšteĭn, L. (2000). *The stefan problem* (Vol. 8): American Mathematical Soc.

Seifeddine, K., Amziane, S., & Toussaint, E. (2022). Thermal behavior of pervious concrete in dry conditions. *Construction and Building Materials, 345*, 128300. doi:https://doi.org/10.1016/j.conbuildmat.2022.128300

Shi, X. (2008). *Impact of airport pavement deicing products on aircraft and airfield infrastructure* (Vol. 6): Transportation Research Board.

Shi, X., Quilty, S. M., Long, T., Jayakaran, A., Fay, L., & Xu, G. (2017). Managing airport stormwater containing deicers: challenges and opportunities. *Frontiers of Structural and Civil Engineering, 11*(1), 35-46. doi:10.1007/s11709-016-0366-6

Stefan, J. (1891). Ueber die Theorie der Eisbildung, insbesondere über die Eisbildung im Polarmeere. *Annalen der Physik, 278*(2), 269-286. doi:https://doi.org/10.1002/andp.18912780206

Sultana, K. R., Dehghani, S. R., Pope, K., & Muzychka, Y. S. (2018). Numerical techniques for solving solidification and melting phase change problems. *Numerical Heat Transfer, Part B: Fundamentals, 73*(3), 129-145. doi:10.1080/10407790.2017.1422629

Swaminathan, C. R., & Voller, V. R. (1992). A general enthalpy method for modeling solidification processes. *Metallurgical Transactions B, 23*(5), 651-664. doi:10.1007/BF02649725

Swaminathan, C. R., & Voller, V. R. (1993). On the enthalpy method. *International Journal of Numerical Methods for Heat & Fluid Flow, 3*(3), 233-244. doi:10.1108/eb017528

Tarwidi, D. (2019). An enthalpy-based finite element method for solving two-phase Stefan problem. *Indonesian Journal on Computing (Indo-JC), 4*, 43. doi:10.21108/INDOJC.2019.4.1.252

Turkyilmazoglu, M. (2018). Stefan problems for moving phase change materials and multiple solutions. *International Journal of Thermal Sciences, 126*, 67-73. doi:https://doi.org/10.1016/j.ijthermalsci.2017.12.019

US-Environmental-Protection-Agency. (2012). *Environmental Impact and Benefit Assessment for the Final Effluent Limitation Guidelines and Standards for the Airport Deicing Category*. Retrieved from https://riverheadny.municipalone.com/files/documents/UpdatedCHPPExhibitF1505044315110520PM.pdf

Vasil'ev, V., Vasilyeva, M., Stepanov, S., Sidnyaev, N. I., Matveeva, O. I., & Tseeva, A. N. (2021). Numerical Solution of the Two-Phase Stefan Problem in the Enthalpy Formulation with Smoothing the Coefficients. *Herald of the Bauman Moscow State Technical University. Series Natural Sciences*, 4-23. doi:10.18698/1812-3368-2021-4-4-23

Voller, V. R. (2008). An enthalpy method for modeling dendritic growth in a binary alloy. *International Journal of Heat and Mass Transfer, 51*(3), 823-834. doi:https://doi.org/10.1016/j.ijheatmasstransfer.2007.04.025

Voller, V. R., & Prakash, C. (1987). A fixed grid numerical modelling methodology for convection-diffusion mushy region phase-change problems. *International Journal of*

*Heat and Mass Transfer, 30*(8), 1709-1719. doi:https://doi.org/10.1016/0017-9310(87)90317-6

Wåhlin, J., Fjærestad, J. S., Thomsen, K., & Klein-Paste, A. (2017). *Thermodynamics of deicing chemicals*.

Wåhlin, J., & Klein-Paste, A. (2017). The effect of mass diffusion on the rate of chemical ice melting using aqueous solutions. *Cold Regions Science and Technology, 139*, 11-21.

Widyatmoko, D., & Dehdezi, P. (2015). *De-icing/Anti-icing agents and their effects on airfield asphalt pavements*. Retrieved from

Wilke, C. R., & Chang, P. (1955). Correlation of diffusion coefficients in dilute solutions. *AIChE Journal, 1*(2), 264-270. doi:10.1002/aic.690010222

Zeneli, M., Nikolopoulos, A., Karellas, S., & Nikolopoulos, N. (2021). Chapter 7 - Numerical methods for solid-liquid phase-change problems. In A. Datas (Ed.), *Ultra-High Temperature Thermal Energy Storage, Transfer and Conversion* (pp. 165-199): Woodhead Publishing.

Zhao, H., Qi, J., Chen, H., Tian, Z., Sun, J., & Sun, Z. (2020). A control volume method based interface movement equation for one-dimensional Stefan problem achieving mass conservation. *Journal of Materials Research and Technology, 9*(6), 16107-16115. doi:https://doi.org/10.1016/j.jmrt.2020.11.086